UCLA
UCLA Electronic Theses and Dissertations

Title
Configuration and Generation of Substorm Current Wedge

Permalink
https://escholarship.org/uc/item/4sw949rf

Author
Chu, Xiangning

Publication Date
2015

Peer reviewed|Thesis/dissertation

eScholarship.org Powered by the California Digital Library
University of California

UNIVERSITY OF CALIFORNIA

Los Angeles

Configuration and Generation of Substorm Current Wedge

A dissertation submitted in partial satisfaction of the

requirements for the degree Doctor of Philosophy

in Geophysics and Space Physics

by

Xiangning Chu

2015

ABSTRACT OF THE DISSERTATION

Configuration and Generation of Substorm Current Wedge

by

Xiangning Chu

Doctor of Philosophy in Geophysics and Space Physics

University of California, Los Angeles, 2015

Professor Robert L. McPherron, Chair

The substorm current wedge (SCW), a core element of substorm dynamics coupling the magnetotail to the ionosphere, is crucial in understanding substorms. It has been suggested that the field-aligned currents (FACs) in the SCW are caused by either pressure gradients or flow vortices, or both. Our understanding of FAC generations is based predominately on numerical simulations, because it has not been possible to organize spacecraft observations in a coordinate system determined by the SCW. This dissertation develops an empirical inversion model of the current wedge and inverts midlatitude magnetometer data to obtain the parameters of the current wedge for three solar cycles. This database enables statistical data analysis of spacecraft plasma and magnetic field observations relative to the SCW coordinate.

In chapter 2, a new midlatitude positive bay (MPB) index is developed and calculated for three solar cycles of data. The MPB index is processed to determine the substorm onset time, which is shown to correspond to the auroral breakup onset with at most 1-2 minutes difference.

Substorm occurrence rate is found to depend on solar wind speed while substorm duration is rather constant, suggesting that substorm process has an intrinsic pattern independent of external driving. In chapter 3, an SCW inversion technique is developed to determine the strength and locations of the FACs in an SCW. The inversion parameters for FAC strength and location, and ring current strength are validated by comparison with other measurements. In chapter 4, the connection between earthward flows and auroral poleward expansion is examined using improved mapping, obtained from a newly-developed dynamic magnetospheric model by superimposing a standard magnetospheric field model with substorm current wedge obtained from the inversion technique. It is shown that the ionospheric projection of flows observed at a fixed point in the equatorial plane map to the bright aurora as it expands poleward, suggesting that auroral poleward expansion is mainly a consequence of magnetic dipolarization caused by the SCW. Chapter 5 shows that increased plasma pressure caused by flow braking has a temporal pattern similar to that of the currents in the SCW. In contrast, flow vortices vanish quickly, suggesting that pressure gradient is an important factor in generating the SCW. The measured pressure gradients are found to be organized relative to SCW central meridian. Nonalignment between pressure gradient and flux tube volume gradient lead to the generation of an SCW with quadrupole FACs (inner and outer loop of FACs). Because the inner current loop is weaker than the outer loop, the combined magnetic effect of the two current loops is similar to a classic SCW. The final chapter studies the magnetic flux transport by earthward flows, and accumulated inside the SCW and enclosed within auroral poleward boundary. Their good agreement suggests that flux accumulation causes magnetic dipolarization and auroral poleward expansion. The strength of the SCW is positively correlated with the amount of magnetic flux accumulated.

The dissertation of Xiangning Chu is approved.

Vassilis Angelopoulos

Robert Strangeway

Walter Gekelman

Robert L. McPherron, Committee Chair

University of California, Los Angeles

2015

This dissertation is dedicated to my parents and sister,

for their unconditional love and care,

to my lovely wife, Jie Deng,

who has offered unyielding support and encouragement,

and to my late grandmother.

TABLE OF CONTENTS

LIST OF FIGURES

ACKOWLEGEMENTS

Foremost, I would like to express the deepest appreciation to my advisor Professor Robert McPherron for the continuous support of my Ph.D. study and research. Bob has been a remarkable advisor to me. He gave me the freedom to research on my own topic of interests, while being so comprehensive to provide the guidance I needed. He provided scientific insight and expertise to answer my questions and improve my understandings. I have certainly been molded by his enthusiasm in science, and I appreciate all the fun and interests he has given me.

I would like to thank my committee members, Vassilis Angelopoulos, Robert Strangeway and Walter Gekelman, for their insightful comments and inspiring questions. I would especially like to thank Vassilis, who has been supportive since the days I began working on THEMIS data. He has provided invaluable advices on research and scientific thinking.

I would also like to express my gratitude to Professor Zuyin Pu, who is the advisor of my undergraduate and master's thesis. He has influenced me in many ways, especially being rigorous and strict in scientific research.

I have greatly benefited from the knowledge and expertise of the professors and colleagues at UCLA and other institutes. I would especially like to thank Tung-Shin Hsu, for his contributions to my thesis with many useful discussions and ideas. I am also very thankful to Margaret Kivelson, Raymond Walker, Chris Russell, Krishan Khurana, James Weygand, Martin Connors and Andrei Runov for their insightful suggestions on my work. I also thank Judy Hohl who helped refine my manuscripts with her expertise in scientific writing.

My thanks to my fellow colleagues and graduate students who made my life here more enjoyable: Hui Zhang, Jiang Liu, Jennifer Kissinger, Mike Hartinger, Feifei Jiang, Ye Gao, Christine Gabrielse, Xuzhi Zhou, Chao Yue, Xiaojia Zhang, Shanshan Li, Jodie Ream, Hanying Wei, Yingdong Jia, Yingjuan Ma, Cong Zhao, Kate Ramer, Adam Kellerman, Kaiqing Yuan, Hao Cao, and more.

Finally, I would like to thank my parents and my wife, Jie Deng, for their unconditional love, support and patience. I could not have finished the thesis without your encouragement.

I acknowledge NASA grant NNX14AO02H and NSF grant AGS-1003854. I would like to thank THEMIS, IMAGE, INTERMAGNET, SuperMAG, IMAGE magnetometer network, GOES, OMNI database, NASA NSSDC and NASA VMO and Geotail for providing the data that are essential for this dissertation work.

VITA

Education

2015 Ph.D. candidate in Space Physics, University of California, Los Angeles

2009 M.S. in Space Physics, Peking University, Beijing, China

2006 B.S. in Space Physics, Peking University, Beijing, China

Publications

Chu, X. N., R. L. McPherron, T.-S. Hsu and V. Angelopoulos (2015), Solar cycle dependence of substorm occurrence and duration: implications for onset, J. Geophys. Res., doi:10.1002/2015JA021104.

Chu, X. N., R. L. McPherron, T.-S. Hsu, V. Angelopoulos, Z. Pu, Z. Yao, H. Zhang and M. Connors (2015), Magnetic mapping effects of substorm currents leading to auroral poleward expansion and equatorward retreat, J. Geophys. Res., 119, doi:Doi 10.1002/2014JA020596.

Chu, X. N., T. S. Hsu, R. L. McPherron, V. Angelopoulos, Z. Y. Pu, J. J. Weygand, K. Khurana, M. Connors, J. Kissinger, H. Zhang and O. Amm (2014), Development and validation of inversion technique for substorm current wedge using ground magnetic field data, J. Geophys. Res., 119(3), 1909-1924, 10.1002/2013ja019185.

Chu, X. N., Z. Pu, X. Cao, J. Wang, V. Mishin, V. Angelopoulos, J. Liu, Y. Wei, K. H. Glassmeier, J. McFadden, D. Larson, S. Mende, H. Frey, C. T. Russell, I. Mann, D. Sibeck, Q. Zong, S. Fu, L. Xie, T. I. Saifudinova, M. V. Tolochko, L. A. Sapronova, H. Reme and E. Lucek (2010), THEMIS observations of two substorms on February 26, 2008, SCIENCE CHINA Technological Sciences, 53(5), 1328-1337, 1315:1303:1300.

Chu, X. N., R. L. McPherron, T.-S. Hsu, V. Angelopoulos, R. Strangeway, J. Weygand, J. Liu (2015), Magnetotail flux accumulation leading to auroral expansion and substorm current wedge: case study, (manuscript ready).

Chu, X. N., R. L. McPherron, V. Angelopoulos, T.-S. Hsu, J. Liu (2015), Is the pressure gradient a driver of the substorm current wedge? A statistical study, (manuscript ready).

Chu, X. N., R. L. McPherron, T.-S. Hsu and V. Angelopoulos (2015), Statistical Relation between the Substorm Current Wedge and Other Substorm Signatures, (manuscript ready).

Connors, M., C. T. Russell, **X. N. Chu** and R. L. McPherron (2015), The February 24 2010 Substorm: A Refined View Involving a Pseudobreakup/Expansive Phase/Poleward Boundary Intensification Substorm Sequence. Earth, Planets and Space (accepted).

Yao, Z., J. Liu, C. Owen, C. Forsyth, I. Rae, Z. Pu, H. Fu, X.-Z. Zhou, Q. Shi, A. Du and **X. Chu** (2015). "A physical explanation for the magnetic decrease ahead of dipolarization fronts ", Ann. Geophys.33(10):1301-1309

Liu, J., V. Angelopoulos, **X. Chu**, X.-Z. Zhou and C. Yue (2015). "Substorm Current Wedge Composition by Wedgelets." Geophysical Research Letters: 2015GL063289.

Yao, Z. H., Z. Y. Pu, C. J. Owen, S. Y. Fu, **X. N. Chu**, J. Liu, V. Angelopoulos, I. J. Rae, C. Yue, X. Z. Zhou, Q. G. Zong, X. Cao, Q. Q. Shi, C. Forsyth and A. M. Du (2014). "Current reduction

in a pseudo-breakup event: THEMIS observations." Journal of Geophysical Research: Space Physics 119(10): 2014JA020186.

Connors, M., R. L. McPherron, B. J. Anderson, H. Korth, C. T. Russell, and **X. N. Chu** (2014), Electric currents of a substorm current wedge on 24 February 2010, Geophys. Res. Lett., 41(13), 4449-4455, doi:10.1002/2014gl060604.

McPherron, R. L., T. S. Hsu, and **X. Chu** (2014), An Optimum Solar Wind Coupling Function for the AL Index, doi:10.1002/2014JA020619.

Z. H. Yao, Z. Y. Pu, A. M. Du, V. Angelopoulos, C. J. Owen, J. Liu, **X. N. Chu**, X. Cao, S. Y. Fu, Q. G. Zong, and Y. Wang (2014), Pressure gradient evolution in the near-Earth magnetotail at the arrival of BBFs, Chin. Sci. Bull., 59(34), 4804-4808, doi:10.1007/s11434-014-0618-6.

McPherron, R. L., D. N. Baker, T. I. Pulkkinen, T. S. Hsu, J. Kissinger, and **X. Chu** (2013), Changes in solar wind–magnetosphere coupling with solar cycle, season, and time relative to stream interfaces, Journal of Atmospheric and Solar-Terrestrial Physics, 99(0), 1-13, doi:10.1016/j.jastp.2012.09.003.

Yao, Z., W. J. Sun, S. Y. Fu, Z. Y. Pu, J. Liu, V. Angelopoulos, X. J. Zhang, **X. N. Chu**, Q. Q. Shi, R. L. Guo and Q. G. Zong (2013). "Current structures associated with dipolarization fronts." Journal of Geophysical Research: Space Physics 118(11): 2013JA019290.

Yao, Z. H., V. Angelopoulos, Z. Y. Pu, S. Y. Fu, M. Kubyshkina, J. Liu, **X. N. Chu**, T. Nishimura, X. Cao, A. M. Du, C. Yue, Q. Q. Shi and Y. Wei (2013). "Conjugate observations of flow diversion in the magnetotail and auroral arc extension in the ionosphere." Journal of Geophysical Research-Space Physics 118(8): 4811-4816.

McPherron, R. L., D. N. Baker, T. I. Pulkkinen, T. S. Hsu, J. Kissinger and **X. Chu** (2013). "Changes in solar wind–magnetosphere coupling with solar cycle, season, and time relative to stream interfaces." Journal of Atmospheric and Solar-Terrestrial Physics 99(0): 1-13.

Kissinger, J., R. L. McPherron, T. S. Hsu, V. Angelopoulos, and **X. Chu** (2012), Necessity of substorm expansions in the initiation of steady magnetospheric convection, Geophys. Res. Lett., 39, doi:Artn L15105

Hsu, T. S., R. L. McPherron, V. Angelopoulos, Y. S. Ge, H. Zhang, C. Russell, **X. N. Chu**, and J. Kissinger (2012), A statistical analysis of the association between fast plasma flows and Pi2 pulsations, J. Geophys. Res., 117, doi:Artn A11221

McPherron, R. L., T. S. Hsu, J. Kissinger, **X. Chu**, and V. Angelopoulos (2011), Characteristics of plasma flows at the inner edge of the plasma sheet, J. Geophys. Res., 116, doi:Artn A00i33 Pu, Z. Y., X. Chu, X. Cao and et al. (2010), THEMIS observations of substorms on 26 February 2008 initiated by magnetotail reconnection, J. Geophys. Res., 115(A2), A02212.

Wei, Y., Z. Pu, M. Hong, Q. Zong, Z. Ren, S. Fu, L. Xie, S. Alex, X. Cao, J. Wang and **X. Chu** (2009). "Westward ionospheric electric field perturbations on the dayside associated with substorm processes." Journal of Geophysical Research (Space Physics) 114: 12209.

Selected Honors and Awards

2014 NASA Earth and Space Sciences Fellowship	NASA
2014 Outstanding Student Presentation Award	Geospace Environment Modeling
2014 Outstanding Original Research Award	Department of Earth, Planetary, and Space Sciences (UCLA)

Chapter 1

Introduction

The cause of magnetospheric substorms is one of the most highly debated topics in the field of space physics. Although magnetospheric substorms have been studied for half a century, a comprehensive picture of substorm physics is still deficient regarding the generation mechanism of the substorm current wedge (SCW) due to lack of observations in the equatorial plane of the tail. The substorm current wedge, which is a core element of substorm dynamics connecting the magnetotail and the ionosphere, is crucial in the understanding of substorms. In this introduction, historical studies and unresolved issues regarding magnetospheric substorms and the substorm current wedge will be discussed.

1.1 Magnetospheric substorms

Magnetospheric dynamics are driven by the solar wind-magnetosphere interaction through two processes: magnetic reconnection [*Dungey*, 1961] and viscous interaction [*Axford and Hines*, 1961]. Magnetic reconnections, both at the dayside and nightside, are the dominant drivers of geomagnetic activity. Dayside reconnection occurs when the solar wind interplanetary magnetic field (IMF) is southward and anti-parallel to Earth's northward dipole magnetic field. Open field lines created by dayside reconnection are transported by the solar wind over both polar caps and stored in the magnetotail lobes. Nightside reconnection converts open magnetic field lines in the lobe to closed magnetic field lines, which are transported earthward in the plasma sheet by bursty bulk flows and

magnetospheric convections, then around the Earth and back to dayside, restoring the dayside flux. This is the Dungey Cycle [*Dungey*, 1961] describing magnetospheric convection driven by reconnection [*Dungey*, 1961]. The difference between dayside and nightside reconnection rates determines the mode of magnetospheric response: magnetospheric substorm, steady magnetospheric convection, sawtooth, or geomagnetic storm.

A magnetospheric substorm is a process of energy and magnetic flux loading and unloading caused by the imbalance between dayside and nightside reconnection. The concept of a substorm was first introduced to describe magnetic perturbations in the polar region during magnetic storms [*Akasofu and Chapman*, 1961]. The term was extended to auroral substorms and polar magnetic substorms, which were used to describe the spatial-temporal development of the bright aurora and the westward electrojet in the ionosphere [*Akasofu*, 1964; *Akasofu et al.*, 1965]. Authors of later works realized that substorm phenomena occur not only in the ionosphere, but also throughout the magnetosphere [*Jelly and Brice*, 1967; *McPherron et al.*, 1967; *Coroniti et al.*, 1968]. The concept of a substorm was then generalized to the magnetospheric substorm [*Akasofu*, 1968; *Coroniti et al.*, 1968], including auroral breakup and expansion, substorm current wedge, near-Earth dipolarization, and Pi2 pulsations. Our understanding of magnetospheric substorms has greatly improved during the ensuing decades of the Space Age, when simultaneous observations on the ground and in space and numerical simulations became available. Many phenomenological substorm models, such as the near-Earth neutral line model (NENL), the near-Earth current disruption model (NECD) and the global synthesis model

[*Pu et al.*, 2001], have been developed. The NENL model suggests that substorms are triggered by mid-tail reconnection at 20-30 R_E (rather than distant tail reconnection at about 100 R_E), which generates bursty bulk flows that travel earthward and cause cross-tail current reduction [*Hones et al.*, 1970; *McPherron*, 1970; *McPherron et al.*, 1973; *Baker et al.*, 1996; *Baumjohann and Nakamura*, 2001; *Angelopoulos et al.*, 2008a]. The NENL model is also referred as the 'outside-in model' because the substorm phenomena start from reconnection in the mid-tail region and then propagate to the near-Earth region. The NECD model, on the other hand, proposes that current disruption first occurs in the near-Earth region and sends out rarefaction waves that travel tailward and trigger mid-tail magnetic reconnection [*Lui*, 1978; 1996]. Therefore, the NECD model is also referred to as an 'inside-out model'. Timing between different phenomena have been studied extensively in an attempt to resolve the differences between the two models [*McPherron*, 1970; *Lui and Murphree*, 1998]. Simultaneous observations from the multiple spacecraft THEMIS mission showing that substorms are likely initiated by mid-tail reconnection support the NENL model [*Angelopoulos et al.*, 2008a].

The NENL model has been progressively to updated explain how near-Earth reconnection generates a magnetospheric substorm [*Hones et al.*, 1970; *McPherron*, 1970; *McPherron et al.*, 1973; *Baker et al.*, 1996; *Baumjohann and Nakamura*, 2001; *Angelopoulos et al.*, 2008a]. Prior to substorm onset, dayside magnetopause reconnection creates open magnetic fields, which are transported by solar wind and stored in the tail lobes, stretching the magnetic field. This is the substorm growth phase [*McPherron*, 1970]. As more open flux is stored in the lobe, the tail becomes even more stretched and

the current sheet becomes thinner, creating favorable conditions for near-Earth reconnection. Near-Earth reconnection converts magnetic energy to thermal and kinetic energy of fast flows accompanied by reconnection fronts travelling both earthward and tailward [*Angelopoulos et al.*, 1992; *Angelopoulos et al.*, 2013]. Tailward plasmoids (or travelling compression regions or anti-dipolarization fronts) are observed tailward of reconnection [*Li et al.*, 2014]. Earthward flows are observed with a dipolarization front near the reconnection site [*Runov et al.*, 2011; *Liu et al.*, 2014]. The dipolarization front reflects and accelerates ions and electrons in the ambient plasma sheet. The ion reflection is not symmetric, with stronger ion acceleration duskward of the dipolarization front rather than on the dawnward side [*Zhou et al.*, 2014a; *Zhou et al.*, 2014c]. These earthward flows transport magnetic flux and energy, and are usually slowed down, stopped, or diverted azimuthally between 8 and 12 R_E [*McPherron et al.*, 2011; *Hsu et al.*, 2012; *Sergeev et al.*, 2014a], the transition region where the magnetic field configuration changes from tail-like to dipole-like. During the flow braking process, the magnetic field becomes dipolarized, which is evidence of cross-tail current reduction. In addition, plasma acceleration and heating during the flow braking process create a high-pressure region that diverts the flows and distorts the magnetic field lines both vertically and azimuthally. The polarity of the magnetic field line distortion is consistent with the existence of field-aligned currents (FACs) in a SCW [*Birn and Hesse*, 2014; *Kepko et al.*, 2014]. The FACs in an SCW flow into the ionosphere in the post-midnight region and flow out of the ionosphere in the pre-midnight region. In the ionosphere, the FACs are connected through the westward electrojet in the auroral oval. Particle precipitation

associated with FACs creates auroral brightening [*Akasofu*, 1964; *McPherron et al.*, 1973]. Magnetic dipolarizations observed at geosynchronous orbit are also consistent with the existence of an SCW [*Nagai*, 1982a; *Nagai*, 1982b]. In addition, dispersionless injections at geosynchronous orbit are also observed as evidence of plasma heating [*Birn et al.*, 1997a; 1997b; 1998]. During the substorm expansion phase, the SCW expands azimuthally, which is consistent with the westward travelling surge of the aurora and the azimuthal expansion of geosynchronous dipolarization [*Nagai*, 1982a; *Nagai*, 1982b; *Liou et al.*, 2002]. The dipolarization region also retreats tailward sometimes [*Baumjohann et al.*, 1999]. The aurora expands poleward as the SCW strengthens [*Chu et al.*, 2015c]. This is the expansion phase starting from substorm onset. The definition of substorm onset includes many phenomena such as magnetic reconnection, earthward flows, auroral brightening and poleward expansion, dispersionless injection, geosynchronous dipolarization, magnetic negative bay of the westward electrojet, midlatitude positive bay, etc. In previous studies, variety of onset indicators has been used to identify substorm onset.

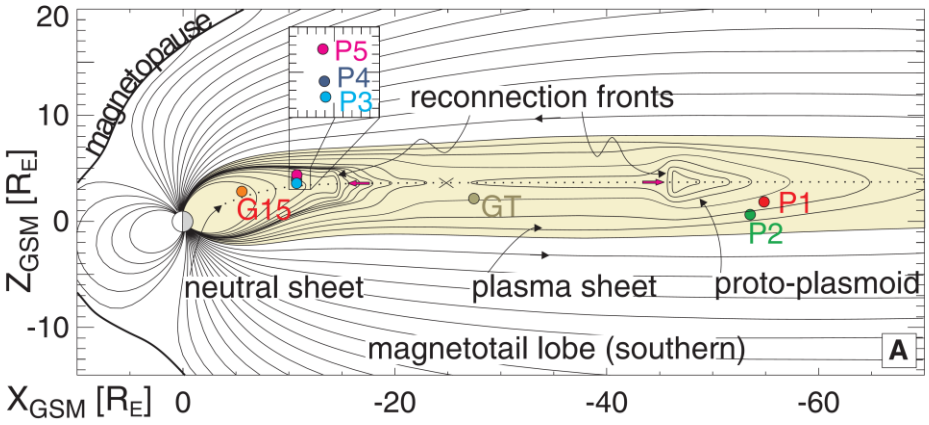

Figure 1. 1 From *Angelopoulos et al.* [2013]. View of a substorm triggered by near-Earth magnetic reconnection. The X-Z projection of the magnetic field lines is modified from the T96 model.

1.2 Substorm current wedge

1.2.1 Brief history

The study of substorm currents goes back for more than 100 years as does the interpretation of magnetic perturbations associated with the dynamic aurora [*Birkeland*, 1908]. It was first believed that FACs were also present in space [*Birkeland*, 1908], but Chapman and others argued that they were confined to the ionosphere. Statistical and modeling studies using magnetic perturbations from ground-based magnetometers have investigated the pattern of currents in the ionosphere, and referred to as the equivalent ionospheric current [*Chapman*, 1918; 1927; *Kamide et al.*, 1976]. Two distinct current patterns were found during different phases of geomagnetic activity. One current pattern with a single current cell found during the substorm expansion phase is referred to as the DP-1 (disturbance polar of the first type) current system [*Nishida*, 1968a; b; *Obayashi and Nishida*, 1968]. Another current pattern, with two cells with their vortices situated on the morning and evening sides, is called the DP-2 current system (disturbance polar of the second type) [*Iijima and Nagata*, 1972; *Kokubun*, 1972; *Clauer and Kamide*, 1985]. Both DP-1 and DP-2 current systems are two-dimensional and confined within the

ionosphere. Although the existence of FACs from space was proposed in 1913 by Birkeland, it was impossible to validate using only ground magnetometers because, according to Fukushima's theorem, magnetic effects of the FACs and their Pedersen currents exactly cancel each other at any point underneath the ionosphere. Using magnetometers onboard spacecraft ATS-1 at geosynchronous orbit and a ground magnetometer at Honolulu, *McPherron et al.* [1973] demonstrated the existence of three-dimensional FACs flowing from the magnetosphere into the ionosphere along magnetic field lines.

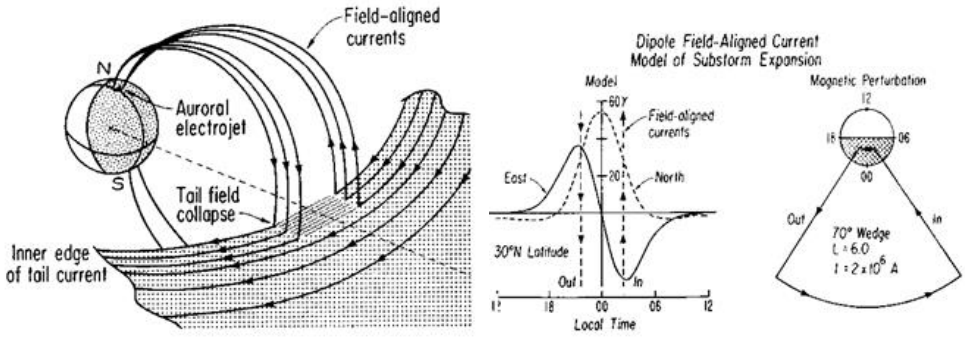

Figure 1.2 From *McPherron et al.* [1973]. A perspective view of the SCW. (a) The cross-tail current is diverted through the ionospheric westward electrojet along magnetic field lines. (b) The northward (H) and eastward (D) components of the SCW-induced magnetic perturbation at 30° latitude versus local time. (c) The X-Y projection of the SCW is shwn.

1.2.2 Three-dimensional SCW

The classic SCW picture represents well the observed magnetic perturbations from ground magnetometers in the auroral oval and at mid latitude, as well as those at

geosynchronous orbit. The classic SCW was envisioned as one current loop comprised of four parts. The cross-tail current is disrupted and connected to the ionosphere through FACs. One FAC (downward FAC) flows out of the equatorial plane and into the ionosphere from the dawn side. The other FAC (upward FAC) flows out of the ionosphere and into the equatorial again from the dusk side. The two are connected in the ionosphere by a westward electrojet across the auroral bulge. The magnetic perturbations of these currents can be measured by ground magnetometers and geosynchronous magnetometers. At higher latitudes in the auroral oval, ground magnetic perturbations are dominated by the westward electrojet, which creates a negative change in the H (northward) component called a negative bay signature. Based on the negative bay signature, auroral electrojet indices are generated to measure the strength of the westward electrojet. At midlatitude, magnetic perturbations are dominated by the two FACs in the SCW. The FACs create positive perturbations in the H component inside the SCW. The H component, a Gaussian-like function relative to local time, is maximized at the central meridian of the SCW. The D (eastward) component has an anti-asymmetric pattern. It has a positive maximum near the upward FAC in the pre-midnight region and a negative minimum in the post-midnight region. This is the midlatitude positive bay (MPB) signature [*McPherron*, 1972; *McPherron et al.*, 1973]. Note that the magnetic perturbations at midlatitude are more complex than illustrated here because: 1) the FACs have different widths (the downward FAC is wide and the upward FAC is narrow), 2) other currents such as the ring current and partial ring current exist, and 3) a lot of fine current structures exist in the FACs. At geosynchronous orbit, the magnetic perturbations

are dominated by two FACs and the reduction in the cross-tail current. And the pattern of the magnetic perturbations is similar to a positive bay signature. The northward component increases (dipolarization) and the eastward component has an anti-asymmetric pattern dependent on local times. The dipolarization and positive bay signature observed by midlatitude ground magnetometers and by geosynchronous magnetometers are consistent in local time [*McPherron and Barfield*, 1980; *Nagai*, 1982a; *Nagai*, 1982b]. In summary, the classic SCW well represents magnetic perturbations at different latitudes on the ground and at geosynchronous orbit.

1.2.3 Two-loop SCW

In contrast to the classic one-loop SCW model, there is growing evidence from numerical simulations suggesting that there is a second, weaker current wedge at the same local time beneath the main current wedge with currents flowing in the opposite direction [*Birn and Hesse*, 1991; 1996; *Raeder and McPherron* 1998; *Birn and Hesse*, 2000; *Yang et al.*, 2011; *Birn and Hesse*, 2013; 2014; *Kepko et al.*, 2014]. Simulations suggest that flow braking and diversion can dipolarize magnetic field lines and bend them away from the central meridian. The rotation of magnetic field lines creates FACs of different polarities, not only in the azimuthal direction on two sides of the central meridian, but also in the radial direction on two sides where magnetic field lines are most bent, creating a quadrupole pattern of FACs. Since the magnetic perturbations of the quadrupole FAC at midlatitudes and at geosynchronous orbit are similar to the outer current loop, the inner current loop should be weaker than the outer current loop (classic

SCW). It has also been suggested by observations of dipolarizations that a weaker inner current loop is required to explain the magnetic dip ahead of the magnetic dipolarization [*Sergeev et al.*, 2011; *Sergeev et al.*, 2014b]. Comparison between modeled and observed magnetic dipolarizations suggests that the inner current loop is usually located at 5.5 R_E and its strength is about only one third that of the outer current loop [*Sergeev et al.*, 2011; *Sergeev et al.*, 2014b]. However, more direct observational evidence is needed to prove the existence of an inner current loop in an SCW. The existence of the partial ring current, the incomplete portion of the ring current, further complicates the SCW model. The partial ring current is similar to the inner current loop, but is located nearer to Earth at 4 R_E and more duskward. It also should be noted that there are other current systems that also have such a quadrupole pattern, such as the Birkeland current in the polar cap and multiple simultaneous current wedgelets surrounding the dipolarization fronts of multiple simultaneous flows [*Birn and Hesse*, 2013; 2014; *Liu et al.*, 2015]. Their relationship to the SCW is still undetermined and under study. Despite the complexity of the SCW, its global magnetic signatures are represented by the classic one-loop SCW model very well [*Chu et al.*, 2015c]. This is because magnetic effects of the inner current loop only partially cancel effects of the stronger outer loop in regions well away from the FAC source region.

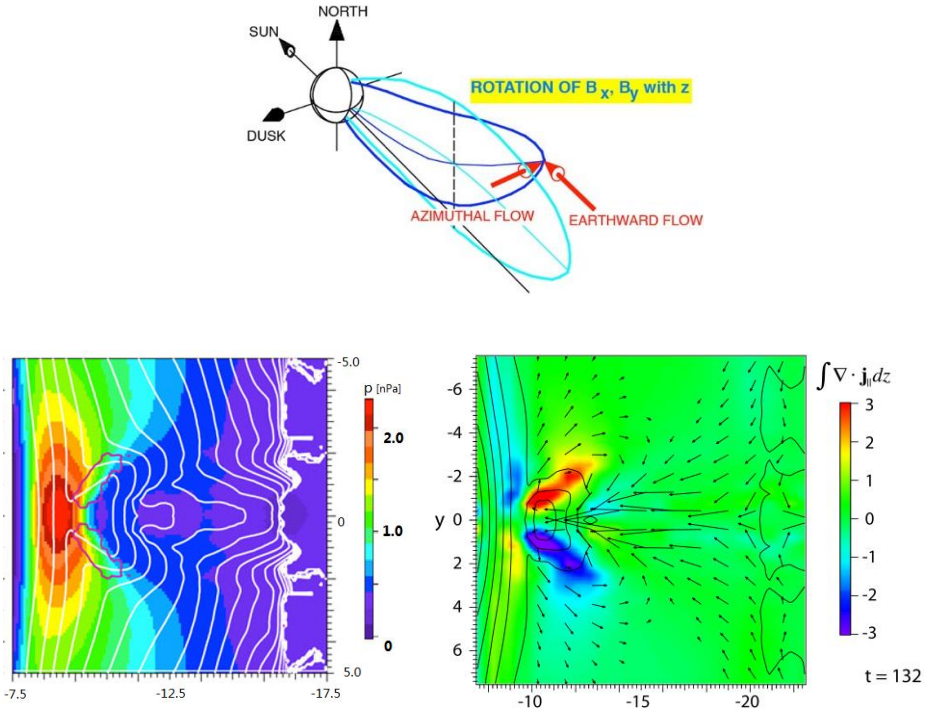

Figure 1. 3 From [*Birn and Hesse*, 2013; 2014; *Kepko et al.*, 2014]. A perspective view of generation mechanisms of the SCW. (a) The pressure gradient and the azimuthal flow will dipolarize the magnetic field lines vertically and bend them azimuthally. Such rotation of the magnetic field lines is consistent with the FACs of the SCW. (b) Plasma pressure on the equatorial plane is based on an MHD simulation of an earthward flow. The white contour shows the flux tube volume. (c) Divergence to field-aligned currents integrated over z axis is shown as color-contour on the equatorial plane. The contour of B_z is shown as black contour. The vectors represent the flow velocity.

1.3 Generation mechanisms

Understanding SCW formation is of key importance in understanding substorm phenomena as a whole since the SCW couples the magnetosphere to the ionosphere. The magnetospheric driver for FACs (not limited to the FACs in a SCW) has been suggested by the Vasyliunas' equation [*Vasyliunas*, 1970]. Starting from the momentum equation, the perpendicular currents are obtained,

$$\mathbf{j}_{\perp} = \frac{\mathbf{B}}{B^2} \times \rho \frac{d\mathbf{u}}{dt} + \frac{\mathbf{B}}{B^2} \times \nabla P \tag{1}$$

Due to current continuity, the parallel current can be expressed as,

$$\nabla \cdot \mathbf{j}_{\parallel} = -\nabla \cdot \mathbf{j}_{\perp} = -\nabla \cdot \left(\frac{\mathbf{B}}{B^2} \times \rho \frac{d\mathbf{u}}{dt} + \frac{\mathbf{B}}{B^2} \times \nabla P \right) \tag{2}$$

By integrating along a magnetic field line from the equator where $j_{\parallel}=0$ to the ionosphere, we obtain the parallel current density,

$$\frac{j_{\parallel}}{B} = -\int_0^s \nabla \cdot \left(\frac{\mathbf{B}}{B^2} \times \rho \frac{d\mathbf{u}}{dt} + \frac{\mathbf{B}}{B^2} \times \nabla P \right) \frac{ds}{B} \tag{3}$$

The inertial term can be neglected under the assumption of approximate force balance in the absence of flows. Therefore, the parallel currents are expressed by Vasyliunas' equation [*Vasyliunas*, 1970],

$$j_{\parallel} = -(\mathbf{B}/B) \cdot \nabla P \times \nabla V \tag{4}$$

where

$$V = \int ds/B \tag{5}$$

is the flux tube volume as integrated from the equatorial plane to the ionosphere, whose gradient is usually radially outward. Therefore, Vasyliunas' equation suggests that azimuthal pressure gradients generate FACs if flows are not present.

If flows are present, FAC generation can be reformulated in an equation containing three source terms [*Sato and Iijima*, 1979; *Hasegawa and Sato*, 1980],

$$j_{\parallel,i} = B_i \int_{eq}^{ion} \left\{ \frac{2\vec{j}_{\perp} \cdot \nabla B}{B^2} + \frac{\rho}{B} \frac{d}{dt}\left(\frac{\Omega}{B}\right) - \frac{\vec{j}_{in} \cdot \nabla \rho}{\rho B} \right\} dl_{\parallel} \tag{6}$$

where $\Omega = \vec{B} \cdot \nabla \times \vec{v}/B$ is the flow vorticity and $\vec{J}_{in} = -\frac{\rho}{B^2}\frac{d\vec{v}}{dt} \times \vec{B}$ is the inertial current.

Vasyliunas' equation explicitly shows that FAC generation is associated with the gradients of equatorial pressure and flux tube volume and their alignments in the absence of flows. If flows are present, FAC generation can be inferred from equation (3), which consists of three source terms in the magnetosphere. The first term on the right side of equation (6) has contribution from the pressure-driven current due to the pressure gradient. The second term on the right side is the current due to flow vorticity and the third term is the inertial current due to acceleration or deceleration of the flows. Their contributions in FAC generation have been investigated in previous studies. *Haerendel* [1992a] discussed flow braking theoretically and concluded that the current wedge is caused by eastward inertial current due to flow braking. This hypothesis was investigated statistically using observations from AMPTE, and it was found that the inertial current was too weak to account for the SCW [*Shiokawa et al.*, 1997]. Instead, the azimuthal

pressure gradient was proposed to be the source of the SCW after flow braking [*Shiokawa et al.*, 1998a; *Shiokawa et al.*, 1998b]. Later it was argued that the pressure gradient in the z direction was the major contributor to the SCW instead of the azimuthal gradient [*Birn et al.*, 1999] combined with changes in B_x and B_y. Later works continued to focus on pressure changes surrounding earthward flows. The plasma density inside earthward flows is lower than that of the surrounding background plasma. Therefore, it is also referred as a depleted plasma bubble. The plasma ahead of the bubble is compressed and the thermal pressure is higher. Azimuthal pressure gradients associated with such a pressure pattern have been suggested to generate a quadrupole SCW during the substorm expansion phase [*Yang et al.*, 2011; *Birn and Hesse*, 2013]. The azimuthal pressure gradient during the growth phase has been also associated with the currents related to growth phase auroral arc intensification [*Xing et al.*, 2009; *Xing et al.*, 2011]. On the other hand, the direct contribution of flow vorticity to FAC generation was estimated using magnetospheric and ionospheric flow vortices during a substorm [*Keiling et al.*, 2009]. This study suggested that flow vortices could generate the FACs of the SCW at the beginning of the substorm expansion phase when flow speed was high enough. In another case study, the current density of FACs from both the flow vortex and the azimuthal pressure gradient was estimated and found to be comparable to the classic SCW [*Yao et al.*, 2012].

1.4 Motivations

The strength of the SCW is usually represented by the auroral electrojet index (AL), which measures the westward electrojet of the SCW by the most extreme the negative bay perturbation seen in the auroral zone. The AL index, however, is biased by 1) its sensitivity to the localized fine structure of the electrojet, 2) pseudobreakup, and 3) the network of stations which occasionally has no stations in local time and latitude beneath the westward electrojet. If AL stations are not located near the onset region, the AL response can be delayed from auroral onset by as much as half an hour. In chapter 2, a new MPB index is developed to measure the strength of the SCW based on the signature of midlatitude positive bays from 1982 to 2012 (31 years). The MPB index, which measures the FACs of the SCW, is insensitive to localized currents related to pseudobreakup; thus, it indicates a major substorm onset. A database of substorm onsets is determined using the MPB index and refined using original observations of magnetic perturbations recorded by ground magnetometers. The MPB onset list is in good agreement (± 2 min) with the auroral onset determined by the IMAGE satellite. Using MPB onset, the solar cycle variation of substorm occurrence was found to depend on solar wind conditions. In contrast, the durations of the substorm expansion and recovery phases do not change with the solar cycle. This suggests that substorm frequency of energy unloading is controlled by solar wind conditions through dayside reconnection, but the unloading process related to flux transport and pileup in the near-Earth region is controlled by the magnetosphere and independent of external driving.

Although theory and simulations suggest that pressure gradients and flow vortices are two potential mechanisms for generating the FACs that feed the SCW, the generation

mechanisms of the SCW still have not been determined from in-situ observations of related phenomena. One reason is that in-situ observations differ at different locations relative to FACs. Although the SCW usually centers at 2300 MLT [*Clauer and McPherron*, 1974a; b], its central meridian can be anywhere on the nightside. In addition, past in-situ measurements were usually single point or separated by about 1 R_E. The separation is significantly smaller than the source region of the FACs in the SCW, which can easily extend 10 R_E in the azimuthal direction and 4 R_E in the radial direction in simulations [*Birn et al.*, 2011; *Yang et al.*, 2011]. In addition, in-situ measurements are sometimes transient and local. Therefore, knowing satellite location relative to FACs is essential in interpreting in-situ measurements. However, FAC locations are difficult to obtain from sparse satellite coverage. They can be obtained, however, from an inversion technique using ground magnetometer data based on the MPB signature [*McPherron et al.*, 1973; *Horning et al.*, 1974a; *Sergeev et al.*, 1996]. An improved inversion technique is developed in this thesis to determine the locations and strengths of the FACs in the SCW using ground magnetometer data at midlatitude (Chapter 3).

In addition, the FACs in an SCW, which connect flows in the magnetotail to aurora in the ionosphere, usually flow along magnetic field lines calculated using a standard magnetospheric model (Tsygenenko model, [*Tsyganenko and Stern*, 1996]). The aurora expands poleward during the substorm expansion phase, however, and sometimes reaches a latitude that maps to the distant tail rather than the flow braking region, which is generally believed to be the source region of the SCW. One reason is that the Tsyganenko model, a statistical model, is highly inaccurate for specific events. Another

reason is that an SCW, the essential current system during substorms, is missing from the Tsyganenko model. To take the SCW-induced magnetic dipolarization into consideration, the magnetospheric model has been improved by superposing a dynamic SCW inverted using ground magnetometer data for specific events (Chapter 4). In addition, the magnetospheric source of the FACs is established using the improved magnetospheric model.

The SCW formation is believed to be related to the process of flow braking and diversion. However, flows can occur at any level of magnetic activity so there is no one-to-one correspondence between flows and substorms. The FACs in the SCW have been suggested to be generated by flow vortices, pressure gradient, or both. Obtaining the pattern of pressure gradient and flow vortices requires the central meridian of the SCW, which is unknown from in situ observations because these FACs are weak and spread over large area relative to the satellite coverage. In this chapter, the central meridian is obtained from the inversion technique for SCW. With the knowledge of FAC locations, the temporal and spatial correlations between the earthward flows and the SCW are investigated in the SCW frame, especially the pressure gradient and the flow vortices relative to substorm onset (temporal) and the central meridian of the SCW (spatial). The pattern of pressure gradient has been obtained in the SCW frame. These results shed light on how the FACs in the SCW is generated.

The mechanisms that generate FACs in an SCW have been investigated in the SCW frame using information about FACs' locations inverted from ground magnetometer data. Yet the area of the FACs is unknown from space observations; thus,

the amplitude of the FACs is unknown from space observations. A global parameter, less dependent on the FACs' location, is needed to measure the amplitude of substorm-related phenomena. Since the SCW formation is related to the process of pileup and diversion of plasma flows, the transport and accumulation of magnetic flux at the inner edge of the plasma sheet by plasma flows and their relationship with SCW formation are investigated (Chapter 6). The relationship between the SCW formation and magnetic flux transport and accumulation provides insight into how substorm phenomena are connected to magnetic reconnection via magnetic flux transport and accumulation.

1.5 Thesis outline

This thesis attempts to determine the generation mechanisms of field-aligned currents in an SCW. A new MPB index is developed to measure the strength of the SCW. A database of substorm onset is determined using the MPB index in Chapter 2. An inversion technique for SCW is developed to determine the location and strength of the current wedge in chapter 3. In chapter 4, using the improved dynamic magnetospheric model, it is established that the source region should be co-located with the flow braking region rather than in the distant tail. In Chapter 5, the generation mechanisms of the SCW have been investigated in the SCW frame. In Chapter 6, the relationship between SCW formation and magnetic flux transport and accumulation is studied. Chapter 7 outlines conclusions and areas for future studies.

Chapter 2

Solar cycle dependence of substorm occurrence and duration

Magnetospheric substorms represent a major energy release process in Earth's magnetosphere. Their duration and intensity are coupled to solar wind input, but the precise way the solar wind energy is stored and then released is a matter of considerable debate. Part of the observational difficulty has been the gaps in the Auroral Electrojet index traditionally used to study substorm properties. In this chapter, I have created a midlatitude positive bay (MPB) index to measure the strength of the substorm current wedge. Because this index is based on midlatitude magnetometer data that are available continuously over several decades we can assemble a database of substorm onsets lasting 31 years (1982-2012). It is confirmed that the MPB onsets have a good agreement (± 2 min) with auroral onsets as determined by optical means onboard the IMAGE mission, and that the MPB signature of substorms is robust and independent of the stations' position relative to ionospheric currents. Using the MPB onset, expansion and recovery as a proxy of the respective substorm quantities it was found that the solar cycle variation of substorm occurrence depends on solar wind conditions and has a most probable value of 80 minutes. In contrast, the durations of substorm expansion and recovery phases do not change with the solar cycle. This suggests that the frequency of energy unloading in the magnetosphere is controlled by solar wind conditions through dayside reconnection,

but the unloading process related to flux pileup in the near-Earth region are controlled by the magnetosphere and independent of external driving.

2.1 Introduction

Magnetospheric dynamics are driven by the solar wind through two processes, viscous interaction [*Axford and Hines*, 1961] and magnetic reconnection [*Dungey*, 1961], which are related to 'directly-driven' and 'loading-unloading' processes in the magnetosphere and ionosphere. During a magnetospheric substorm an important energy unloading process, magnetic reconnection, converts lobe magnetic energy into thermal and kinetic energy of fast flows. Magnetic flux brought by these flows pileup in the near-Earth region, change the magnetic configuration from a stretched tail to more dipolar field and reduce the cross-tail currents. Braking and diversion of these flows in the near-Earth region bend the magnetic fields, and generate field-aligned currents (FACs) [*Xing et al.*, 2009; *Yao et al.*, 2012; *Birn and Hesse*, 2014]. The cross-tail current is connected through the ionospheric westward electrojet via the FACs, forming the substorm current wedge (SCW) [*McPherron et al.*, 1973]. Development of the SCW is associated with auroral brightening and expansion [*Akasofu*, 1964]. The substorm onset can be identified using the signature of auroral brightening [*Frey et al.*, 2004] and the change in the auroral electrojet measured by standard auroral indices (AE, AU, and AL) [*Hsu and McPherron*, 2012] or by SuperMAG electrojet indices [*Gjerloev*, 2009; *Newell and Gjerloev*, 2011a] or localized electrojet indices using IMAGE chain [*Amm and Viljanen*, 1999; *Pulkkinen et al.*, 2003; *Guo et al.*, 2014a].

The AL index, however, is aliased by its sensitivity to localized fine structure of the electrojet and the network of stations occasionally missing stations in local time and latitude relative to the westward electrojet. If AL stations are not located near the onset region the AL response can be delayed from auroral onset by as much as half an hour [*Chu et al.*, 2014a]. Besides, the strength of the westward electrojet is underestimated when the auroral oval contracts or expands away from AL stations and overestimated when some AL station observes localized currents. In addition, auroral indices has a data gap between 1988 and 1990. Conversely, the midlatitude positive bay (MPB), signature of the SCW, varies smoothly over local time and is insensitive to electrojet latitude [*Chu et al.*, 2014a]. Midlatitude magnetometer data are available continuously over several decades. Although MPB magnetic perturbations have been used to infer SCW location and strength [*Horning et al.*, 1974a; *Sergeev et al.*, 1996; *Chu et al.*, 2014a], no index exists to measure the strength of the SCW.

Geomagnetic activity, as represented by the AL index, is delayed from the maximum of the solar cycle by several years and peaks during the declining phase [*Hsu et al.*, 2015]. The AL index, which has a higher correlation coefficient with solar wind speed than with sunspot number [*Newell et al.*, 2007], can be predicted using solar wind conditions [*McPherron et al.*, 2009]. Substorm waiting time, the time between onsets is another indicator of geomagnetic activity that varies throughout the solar cycle [*Tanskanen*, 2009; *Hsu et al.*, 2015]. However, solar cycle variations of substorm waiting time and duration have not been extensively studied because of a lack of long-term substorm onset data.

Variations in geomagnetic activity may be enhanced at the spring and fall equinoxes by three mechanisms: the Russell-McPherron effect [*Russell and Mcpherro.Rl*, 1973], the equinoctial effect [*Bartels*, 1932], and the axial effect [*Cortie*, 1912]. According to a recent study, semiannual geomagnetic variation is dominated by the equinoctial effect rather than the axial effect [*Svalgaard*, 2011]. *Cliver et al.* [2000] suggested that the equinoctial effect contributes more than Russell-McPherron effect. *McPherron et al.* [2013] found that about 40% of the semiannual variation in geomagnetic activity can be attributed to the Russell-McPherron effect and 60% to other processes when Ey =VBs is used as the solar wind coupling function (Ey is the duskward component of the electric field calculated from the solar wind speed V and southward interplanetary magnetic field Bs). The universal time variation in geomagnetic activity cannot be studied using auroral electrojet indices because the station coverage is biased in local time [*McPherron et al.*, 2013]. Such bias in universal time is avoided in the MPB index.

In this chapter, an MPB index is created to measure SCW current strength. In the second section, a database of over 40,000 substorm onsets from 1982 to 2012 is created using the MPB index refined with original data. In the third section, solar cycle variation of substorm onset and its correlation with the solar wind are examined. The seasonal and diurnal variations in geomagnetic activity and their good correlation with the equinoctial effect are shown. Solar cycle variations in substorm waiting time and duration of substorm expansion and recovery phases are examined.

2.2 Substorm database

2.2.1 Midlatitude positive bay index

Midlatitude positive bay is the magnetic perturbation of a substorm current wedge at midlatitudes (generally from 20-53 in magnetic latitude) [*McPherron et al.*, 1973]. Within an SCW, the northward component H is positive and symmetric about the central meridian; the eastward component D is antisymmetric about the central meridian in both hemispheres. The signature of MPB has been used to identify substorm onset when the H component increases sharply [*Caan et al.*, 1978]. The MPB perturbation is smoother and less influenced by the latitude of the electrojet than the negative bay of the westward electrojet in the auroral oval [*Chu et al.*, 2014a]. In addition, more stations are available at midlatitudes that guarantee better coverage in local time. In this chapter, an MPB index was created to measure SCW strength at one minute resolution from 1982 to 2012 (31 years). Similar to the AL index, which measures the westward electrojet of the SCW, the MPB index measures the FACs of the SCW. The MPB index is created in the following steps:

1. Magnetic field data are obtained from 41 stations at midlatitudes (20°<|magnetic latitude|<52°) from the International Real-time Magnetic Observatory Network (INTERMAGNET) and SuperMAG and converted to HDZ coordinates. The Z-direction points toward the center of the Earth; H points to the magnetic north pole; and D is orthogonal to H and roughly eastward.
2. Secular trend and solar-quiet variations are removed from original magnetic field data.

3. Magnetic field data are then detrended using a twelve-hour low pass filter to remove the effect of longer duration geomagnetic activity, such as magnetic storms and steady magnetospheric convection.
4. The amplitude of magnetic variations is calculated using the moving variance of changes in the H and D components $\Delta H^2+\Delta D^2$. Because the central meridian of the SCW is usually located at 23:30 MLT, only stations near midnight (within 5 hours to 23:30 MLT) are used.

The MPB index measures how much the magnetic field differs from the background level at midlatitudes. Its unit, nT^2, is proportional to the power of the magnetic perturbations rather than the amplitude.

2.2.2 Substorm onset list

A database of substorm onsets is created in this chapter. The criteria are listed below:

1. The MPB index must be larger than the threshold of 25 nT^2 to identify a substorm.
2. The timing of maximum substorm development (T_{max}) is identified when the MPB index reaches its maximum.
3. Only isolated MPBs are selected. Substorm events should be separated by 30 minutes.
4. Preliminary onset is defined at the time of the maximum of the second derivative of the MPB index, indicating the elbow point of the MPB index.
5. MPB onset is refined using the original magnetic field. A combined slope $\left((\frac{\partial H}{\partial t})^2 + (\frac{\partial D}{\partial t})^2\right)$ from stations with large magnetic perturbations (>10 nT in 20 min) near

midnight (within 5 hours to 23:30 MLT) is calculated. The refined onset is identified at the time of elbow of the combined slope.

6. The end of MPB (T_{end}) is defined as the time the MPB index changes from decreasing to quiet. It is identified at the elbow of the MPB index.
7. MPB onsets are identified from 1982 to 2012 (31 years). In total, 40,562 substorms were found.

2.2.3 Substorm example

An isolated substorm observed on 11 January 2002 is used for illustration. Figure 2.1a shows the absolute values of the AL index, which started to increase around 07:00 UT and increased sharply at 07:07 UT. It reached the maximum at 07:13 UT and then slowly decreased for over an hour. The MPB signatures at stations near midnight are shown in the H and D components in Figure 2.1b and Figure 2.1c. The H components from different stations began to increase at 07:00 UT and reached its maximum at 07:10 UT. The D components had both increases and decreases, the polarity of which depended on the local times and hemisphere of the stations. They began to change at about 07:00 UT. Both H and D became quiet after ~07:25 UT. After 07:25 UT, the background values of H and D were elevated. However, no signature of MPB (no increase in H and no diversion in D) was present, suggesting that the substorm current wedge had diminished. Both H and D were elevated after the substorm by either rotation of the Earth or the change in the magnetospheric state rather than by the SCW.

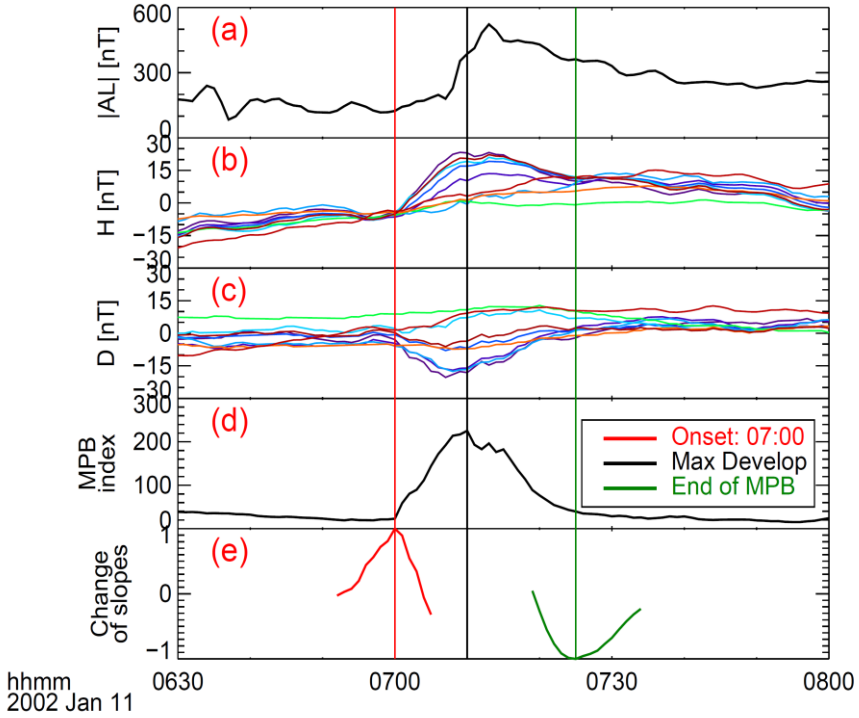

Figure 2.1. Midlatitude positive bays on 11 January 2002. The absolute values of the AL index is shown in panel (a). Panels (b) and (c) show H and D components from stations near midnight at midlatitudes. Panel (d) shows the MPB index. Panel (e) shows the change rate of the combined slope of H and D components from stations near midnight, which is normalized by its maximum value. Timings of MPB onset (red), maximum development T_{max} (black), and the end of the recovery phase T_{end} (green) are marked by vertical lines.

The SCW intensity, represented by the MPB index in Figure 2.1d, started to increase from 07:00 UT and reached its maximum (T_{max}) at 07:10 UT. Unlike the AL

index which had a long tail during the recovery phase, the MPB index decreased much faster and became quiet around 07:25 UT. The red line in Figure 2.1e shows the second derivative of the combined slope from stations near midnight, which is normalized by its maximum value. At 07:10 UT, it reached the maximum, which was identified as MPB onset. The green line in Figure 2.1d shows the second derivative of the MPB index (normalized by its maximum), which was decreasing at its fastest rate at 07:25 UT (T_{end}). The MPB onset, T_{max}, and T_{end} are marked by vertical lines.

2.3 Thirty-one years of MPB statistics

2.3.1 Correlation with auroral onset

The MPB onset database is validated using other substorm onset lists. Figure 2.2 shows the time delay analysis between the MPB onset and the auroral onset identified using global auroral observations from the IMAGE satellite [*Frey et al.*, 2004]. The epoch zero is the MPB onset. Positive (negative) time delay means that auroral onset occurs later (earlier) than the nearest MPB onset. A sharp peak near epoch zero is found in the time delay distribution, which is fit by a Gaussian function. The center of the Gaussian function is 0.4 min; its width is 1.9 min. Considering the ~2 min resolution of auroral observations from IMAGE and one min resolution of the MPB index, the width of 1.9 min suggests that the SCW is observed simultaneously by aurora at high latitude and MPB at midlatitude. The same analysis has been applied between MPB onsets and AL onsets identified using the AL index [*Hsu and McPherron*, 2012]. A sharp peak

around epoch zero centered at -0.8 min with a width of 5.0 min was found.

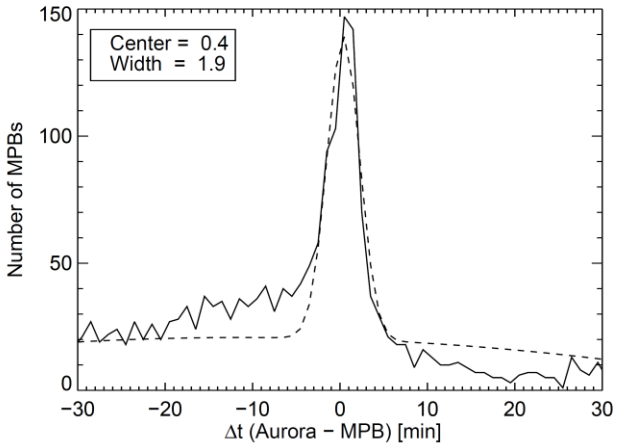

Figure 2.2. Time delay distribution between MPB onset and auroral onset identified by IMAGE spacecraft [*Frey et al.*, 2004]. Positive (negative) delay means that auroral onset occurs later (earlier) than MPB onset. The time delay distribution is fitted by a Gaussian function, which centers at 0.4 min with a width of 1.9 min.

2.3.2 Solar cycle variation

Solar cycle variation of MPBs from 1982 through 2012 is illustrated in Figure 2.3. As shown in the sunspot number (SSN) in Figure 2.3a, the 31-year span consists four solar cycles: the declining phase of solar cycle 21 (January 1982 to September 1986), full solar cycle 22 (September 1986 to May 1996), full solar cycle 23 (May 1996 to January 2008), and the rising phase of solar cycle 24 (January 2008 to December 2012). There are three solar minima (red squares) and three solar maxima (blue squares). The solar wind speed in Figure 2.3b is highly variable (higher during declining phases and lower during rising

phases) and not well correlated with the SSN. It peaks in 1982, 1994, and 2003 and has three minimums in 1987, 1997, and 2009.

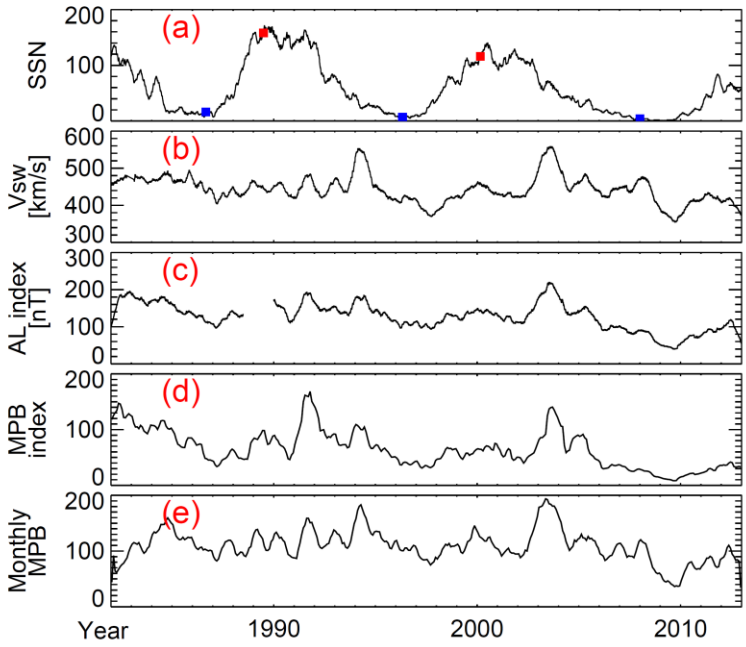

Figure 2.3. Solar cycle variations of (a) sunspot number, (b) solar wind speed, (c) AL index (absolute value), (d) MPB index, and (e) monthly number of MPBs from 1982 to 2012. Solar maximums and minimums are marked by red and blue squares in panel (a).

The AL index in Figure 2.3c (absolute values hereafter) shows that geomagnetic activity was well correlated with solar wind speed but not with sunspot number. The AL index is higher during declining phases (1982-1984, 1991-1993, and 2002-2003) when the solar wind speed was higher. Both the AL index and the solar wind speed are delayed from the solar maximums by several years. This result is consistent with previous studies that showed good correlations between geomagnetic activity and solar wind speed [*Hsu and McPherron*, 2007; *Svalgaard and Cliver*, 2007; *Newell et al.*, 2013]. The MPB index

in Figure 2.3d has a trend that is similar to that in the AL index. The MPB maximums (in 1982, 1991, and 2003) and minimums (in 1987, 1997, and 2009) occurred in the same years as those in the AL index. During the extreme solar minimum around 2009, the AL index and MPB index were considerably lower than previous values. Geomagnetic activity began to recover around January 2010. The monthly number of substorm onsets (monthly MPBs) is calculated using the substorm onset list identified using the MPB index in section 2.2.2 and shown in Figure 2.3e. More events were found in active years and fewer events in quiet years. Pearson correlation coefficients are 71% between the MPB index and the solar wind speed, and 83% between the substorm number and the solar wind speed.

2.3.3 Seasonal and diurnal variation

Figure 2.4 shows the solar cycle and diurnal variation of the MPB numbers in one-month-UT bin. It is higher in active years (1984, 1994, and 2003) and lower in quiet years (1987, 1997, and 2009). The diurnal distribution in UT is uniform from 1991 to 2012. From 1982 to 1990, fewer events were found between 12 to 18 UT. The diurnal distribution is biased in UT prior to 1991 because of the lack of stations in the Pacific Ocean which is located near midnight between 12-18 UT. The diurnal distribution of the MPB numbers is rather uniform from 1991 to 2012 when more stations became available in the Pacific Ocean.

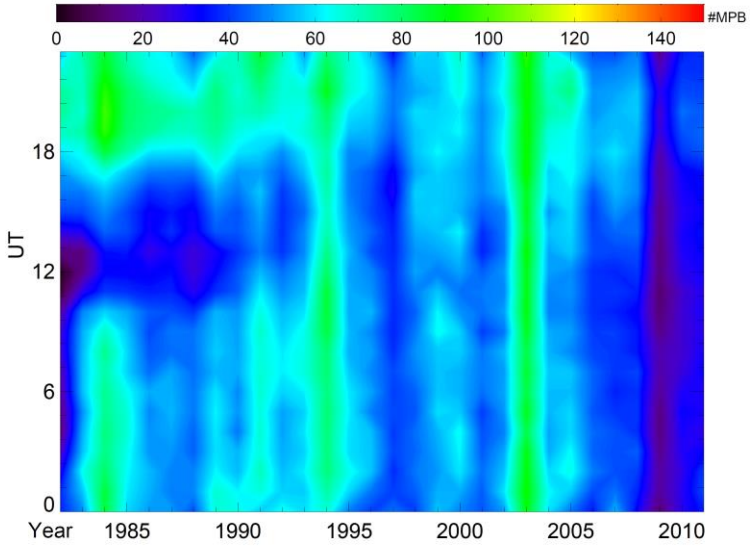

Figure 2.4. Solar cycle and diurnal variation of MPB numbers in one-month-hour bin from 1982 to 2012.

Figure 2.5 illustrates seasonal and diurnal variations in the MPB numbers. To avoid the bias in the diurnal distribution, the database of MPBs from 1991 through 2012 (22 years) is employed. On the right side, the diurnal distribution of MPBs is rather uniform, suggesting that the MPB onsets are not biased by the station coverage from 1991 to 2012. On the top, the seasonal distribution shows a semi-annual variation with maximums at equinoxes (in March and October) and minimums around solstices (in July and January). The seasonal distribution is asymmetric (higher in spring than fall). The colored contour shows the variation in the MPB numbers, with the outline of the dipole's tilt angle φ_{tilt} (the angle between the GSM z-axis and the dipole axis). The tilt angle is the complementary angle of the geomagnetic colatitude of the sub-solar point ψ, which controls the equinoctial effect ($\varphi_{tilt} = 90^{o} - \psi$). The tilt angle changes roughly between $\pm 33^{o}$,

corresponding to the range of the ψ between 90±33º. In this chapter, the tilt angle is used to study the equinoctial effect. Two minima of the MPB numbers were found at 16:00 UT in June and at 04:30 UT in December, and were co-located with the extremes of the tilt angle (contour of 30º and -30º). On the other hand, the maximums of the MPB numbers were found around spring and fall equinoxes. They (the maximums of the MPB numbers) were higher at later UTs in March and October, and at earlier UTs in April and September. The maximums were co-located with the contour of the tilt angle of 0º. The similarity between the contours of the MPB numbers and the tilt angle suggests that the geomagnetic activity can be explained by the equinoctial effect controlled by the tilt angle. To investigate the equinoctial effect on the MPBs, we fitted the Svalgaard function $S(\emptyset) = 1/(1 + 3cos^2\emptyset)^{2/3}$ [*O'Brien and McPherron*, 2002; *Svalgaard et al.*, 2002] to the distribution of the MPB numbers. We found that 62% of the seasonal and diurnal distribution is explained by the Svalgaard function and that the residual map only shows excess signal in the European sector and no clear pattern characteristic of the Russell-McPherron effect. While the equinoctial effect and the Russell-McPherron effect contribute to the geomagnetic activity, it is clear that some other underlying mechanisms are required to explain the observed seasonal and diurnal variations. As shown in Figure 2.3 and recent studies [*Newell and Gjerloev*, 2011b; *Guo et al.*, 2014b; *McPherron et al.*, 2014], the solar wind driving evaluated using various solar wind coupling functions reveals a clear annual variation. The seasonal variations of the MPB index are not symmetric respective to summer solstice and are modulated by the solar wind driving in every single year. The modulation by the solar wind driving strength partly contributes to

the seasonal variation in the substorm occurrence.

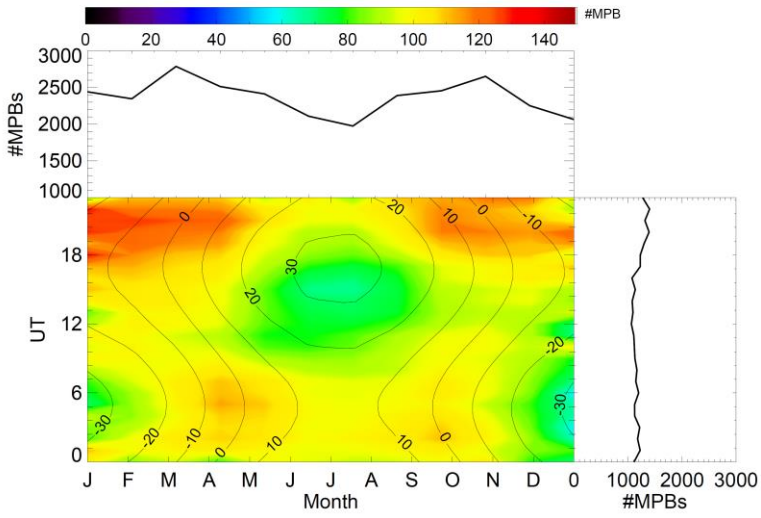

Figure 2.5. Seasonal and diurnal variation in MPB numbers in one-month-UT bin from 1991 to 2012 is shown as color contour outlined with Earth's tilt angle related to the equinoctial effect. Seasonal MPB numbers are shown in the top panel, and the diurnal MPB numbers are shown on the right.

2.3.4 Substorm waiting time

Substorm waiting time, the time between substorms, measures the characteristic time of the unloading process in the magnetosphere. Figure 2.6a shows the substorm waiting time distribution for MPB onsets from 1982 to 2012. The most probable waiting time value is 80 minutes. The median and mean values are ~3 and ~8 hours, respectively. The same analysis was performed on MPB onsets every year. Yearly mean values of the waiting time are shown in Figure 2.6b. The waiting times change over the solar cycles. Waiting time minimums were found in 1984, 1994 and 2003, which were active years.

The minimums of the mean values were ~4 hours, which corresponded to 6 substorms every day. Waiting time maximums were found in 1997 and 2009, which were quiet years. In 1997, the waiting time was ~9 hours, which corresponded to less than three substorms every day. The waiting time changed by a factor of two between 1997 and 2003. In the extreme minimum year of 2009, the waiting time was ~18 hours, which corresponded to only one substorm each day. The waiting time changed by a factor of five between 2003 and 2009.

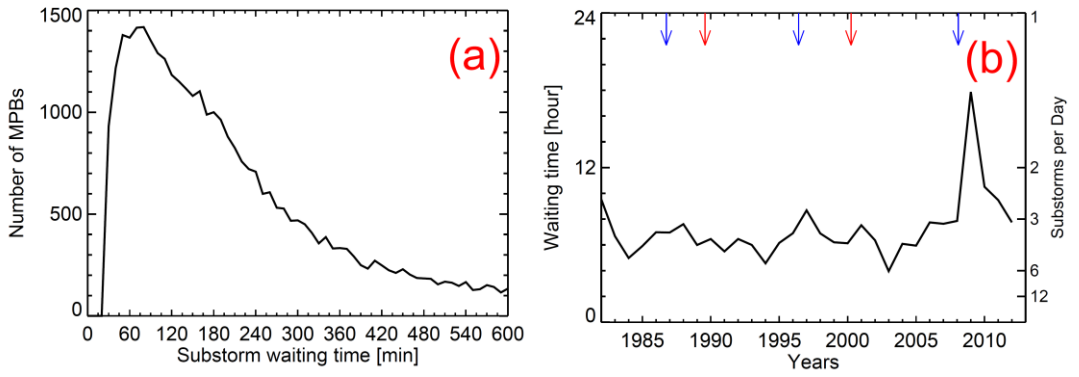

Figure 2.6. (a) Distribution of substorm waiting time. (b) Solar cycle variation of substorm waiting time from 1982 to 2012. Solar minimums and maximums are marked by blue and red arrows.

2.3.5 Substorm duration

Durations of different substorm phases were examined to study the general behavior of the substorms. Figure 2.7a shows the probability distributions for the durations of substorm expansion (purple), recovery (red), and the entire substorm (black) from 1982

to 2012. The most probable duration values are 16 min for expansion, 18 min for recovery, and 40 min for the entire substorm. The mean values are 21, 29, and 50 min, respectively. The same analysis is performed on every year of MPB onsets. Figure 2.7b shows the mean durations of expansion (purple), recovery (red), and the entire substorm (black). Unlike substorm waiting times, the durations do not change significantly throughout solar cycles.

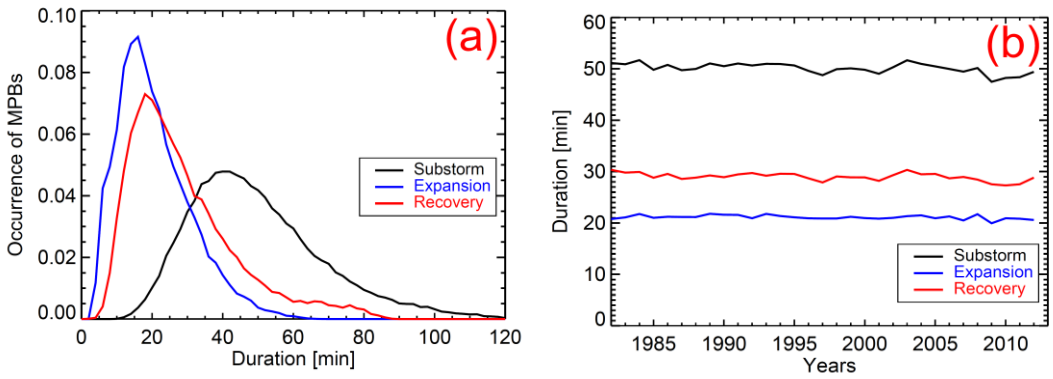

Figure 2.7. (a) Occurrence of durations of expansion (blue), recovery (red) phases and whole substorm (black) from 1982 to 2012. (b) Solar cycle variation of the durations of substorm expansion (blue), recovery (red) phases and whole substorm (black).

2.4 Discussion

2.4.1 Solar cycle effect

2.4.1.1 Substorm dependence on solar wind condition

Geomagnetic activity measured at mid latitudes correlates well with the solar wind

speed but not with the sun spot number. As shown in Figure 2.3, the minima and maxima of the AL and MPB index are delayed from those of the sunspot number by several years. They are higher during the declining phases instead of solar maxima, and lower during the rising phases rather than solar minima. The solar extreme ultraviolet (EUV) irradiance that induces the majority of dayside ionospheric conductivity is measured by the F10.7 index. The F10.7 index generally varies linearly with the sunspot number. The poor correlation between geomagnetic activity and the sunspot number suggests that the geomagnetic activity as measured by MPB is not directly controlled by dayside ionospheric conductivity induced by the solar EUV irradiance. On the other hand, the AL and MPB indices have good correlations with the solar wind speed. The correlation coefficients are 71% between the monthly averages of V_{sw} and the MPB index and 83% between V_{sw} and number of MPBs. *Svalgaard and Cliver* [2007] also found good correlation between the inter-hourly variability index at mid latitudes and solar wind condition (BV^2). Similar studies show good correlation between the AL index and the solar wind speed [*Crooker et al.*, 1977; *Newell et al.*, 2013; *Hsu et al.*, 2015].

A clear pattern of recurrence in geomagnetic activity is found throughout solar cycles. The geomagnetic activity is higher during declining phases and lower during rising phases. The most active years (1984, 1994, and 2003) were delayed from solar maximums by 2-3 years. The quietest years (1987, 1997, and 2009) were delayed from solar minimums by 1-2 years. As discussed above, geomagnetic activity is highly correlated with solar wind condition. Each peak in the MPB and AL indices corresponds to a peak in the solar wind speed and vice versa.

The most distinctive feature in cycle 23 is the extreme solar minimum in 2009. During the prolonged declining phase, the solar wind speed dropped to 350 km s^{-1} in 2008 and 2009, which was much lower than previous solar minimums. Geomagnetic activity was also extremely low in 2008 and 2009 and started to recover since 2010. In addition to the extreme solar minimum, the solar maximum in 2003 was also unusually high and lasted longer than that of cycle 22.

2.4.1.2 Substorm waiting time

Substorm waiting time, which measures how often the magnetotail releases energy, is highly dependent on solar wind condition. Figure 2.6a shows that the waiting time has a preferred value of 80 min, but the value varies over the solar cycle as shown in Figure 2.6b. In active years, more substorms were observed, and thus the substorm waiting time is shorter, and vice versa. Substorm numbers changed by a factor of 5 in different years. In addition, there is a general trend that the waiting time is larger during solar rising phases and lower during declining phases, which is also found using AL onset at high latitude [T. S. Hsu et al., submitted manuscript 2015]. Energy unloading in the tail is directly related to the energy input from the solar wind, which has been estimated using different equations. Akasofu's $\varepsilon = vB^2 sin^4\left(\frac{\theta}{2}\right) l_0^2$ [*Akasofu*, 1996] is proportional to the solar wind speed. The universal coupling function $\mathrm{d}\emptyset/\mathrm{dt} = v^{4/3}B^{2/3}sin^{8/3}\left(\frac{\theta}{2}\right)$ [*Newell et al.*, 2007] and the optimum coupling function $v^{1.74}B^{0.74}sin^{3.77}\left(\frac{\theta}{2}\right)$ [*McPherron et al.*, 2014] also suggest the solar wind input is directly related to solar wind speed.

2.4.2 Intrinsic pattern of magnetospheric unloading

An intrinsic pattern in the energy unloading process in the magnetosphere was found and does not depend on external solar wind speed. As shown in Figure 2.7a, the durations of substorm phases (expansion, recovery, and entire substorm) did not change throughout several solar cycles. This suggests that, unlike substorm waiting time, the durations of substorm expansion and recovery phases are independent of the solar wind coupling function, which depends on the solar wind speed. Figure 2.8 shows the probability distributions of expansion, recovery, and entire substorm durations categorized by the MPB strength measured by the MPB index. The probability distributions are almost identical for substorms of different sizes measured by the MPB index, suggesting that the durations of different substorm phases are independent of substorm size as well.

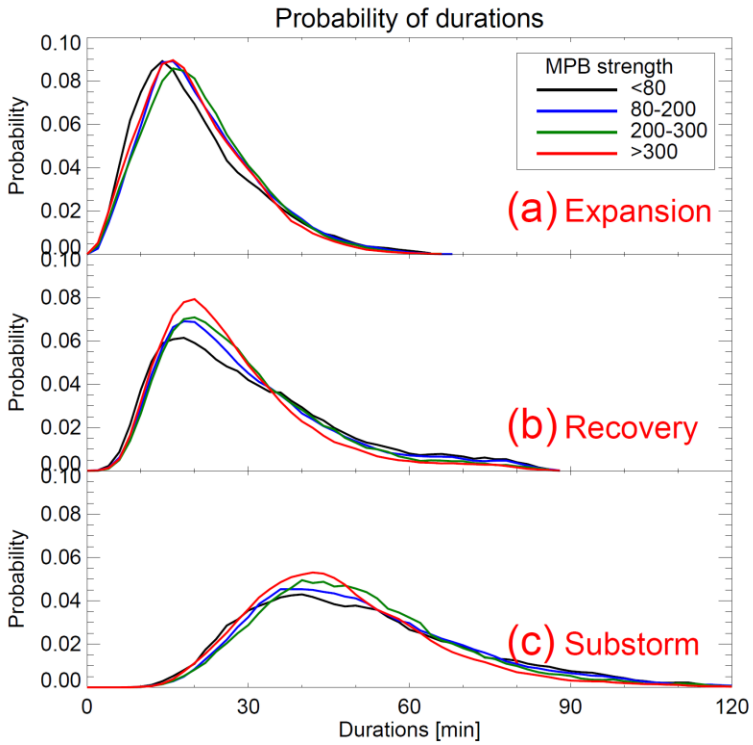

Figure 2.8. Probability distributions of durations of (a) expansion, (b) recovery phases and (c) substorms categorized by substorm size measured by the MPB index.

The unchanging duration of expansion and recovery phases implies that related dynamic processes in the magnetosphere have intrinsic patterns. During the substorm expansion phase, magnetic reconnection converts magnetic energy in the lobe to kinetic and thermal energy of fast flows. Fast flows are usually decelerated between 8-10 R_E, the transition region [*McPherron et al.*, 2011; *Hsu et al.*, 2012]. Flow deceleration is caused by the unbalanced forces among the thermal and magnetic pressures and magnetic curvature, which are dominated by the Earth's dipole field and are insensitive to the external solar wind condition. Braking and diversion of the flows bend magnetic field lines duskward or dawnward at different locations relative to the flows. Distortion of the magnetic field generates field aligned currents of the SCW [*Birn and Hesse*, 2014]. Therefore, the substorm expansion phase, corresponding to braking and diversion of the flows, has a fixed time scale that is controlled by the magnetosphere rather than the solar wind. Magnetic flux carried by fast flows is accumulated in the pileup region. During the substorm recovery phase, the flux is transported toward the dayside by enhanced magnetospheric convection [*Kissinger et al.*, 2012]. The amount of accumulated magnetic flux depends on the electric field of the flows. The enhancement of magnetospheric convection depends on the extra electric field (or accumulated magnetic flux) of the flows and the background magnetic field strength. The strength of the background magnetic field is dominated by Earth's dipole, which is rigid to the solar wind. Therefore, both the enhanced convection and the amount of accumulated flux

depend on the electric field of the flows. The timescale of flux decay is controlled by the property of the flows rather than solar wind. As a result, the substorm recovery phase also has a peculiar pattern and is independent of solar wind.

2.4.3 Difference between AL and MPB indices

Although onsets occurred at midlatitude and high latitude simultaneously, the pattern of the AL index is different from the MPB index. As shown in Figure 2.2, the good correlations (0.4±1.9 min between the MPB onsets and the auroral onsets and -0.8±5.0 min between the MPB onsets and the AL onsets) suggest that substorm onsets are well identified using auroral observations and indices from both high latitude and mid latitude. However, Figure 2.1 shows that the sharp increase in the AL index is delayed from the substorm onset; and the AL index has an unexpected long tail during the recovery phase even when no MPB signature of the SCW was present in the H and D components. The AL response is delayed from substorm onset because the AL index is biased by stations distribution in local time and latitude. It responds to the westward electrojet later than onset if the electrojet was first established far away from AL stations [*Chu et al.*, 2014a]. The unexpected long tail in the AL index is because it measures not only the westward electrojet of the SCW, but also the variations in the two-cell convection. The DP1 current is the equivalent ionospheric current of the SCW, basically the westward electrojet, which is related to the unloading processes in the magnetosphere and independent of solar wind driving. The DP2 current is the equivalent ionospheric current of the two-cell convection, which is directly driven by dayside reconnection by the solar wind and

nightside reconnection [*Siscoe and Huang*, 1985]. The MPB index is sensitive to the FACs of the SCW, which corresponds to the unloading processes independent of the solar wind driving. The AL index, which is the lower envelope of the H components in the auroral oval, measures the larger magnetic perturbation of either DP1 or DP2 current systems. During the expansion phase and earlier recovery phase, the AL index is dominated by the magnetic perturbations of the westward electrojet of the SCW. Later during the recovery phase, the SCW diminishes and the convection becomes relatively stronger and convects tail flux toward dayside. The change in the convection dominates the magnetic perturbations at AL stations, which causes a long tail in the AL index and a longer substorm duration as shown in Figure 2.1. Since the convection is also dependent on solar wind driving, the intrinsic pattern of unloading process independent of solar wind driving cannot be found from the AL index. This conclusion is supported by a recent study using auroral electrojet indices from IMAGE network, which found that substorm duration was longer in active years (3.3 hours in 2003) and shorter in quiet years (2.7 hours in 1997) [*Tanskanen*, 2009].

The difference in the MPB and AL indices are examined using the superposed epoch analysis (SPEA) of the MPB and AL indices relative to the MPB onsets shown in Figure 2.9. At the substorm onset, both indices increased sharply. The AL index reached its maximum 18 min after the onset, which is similar to the MPB index. During the substorm recovery phase, however, the AL index has a longer tail than the MPB index. This fact suggests that the SCW (unloading process) dominates the MPB index during the entire substorm. However, the AL index is dominated by the SCW during the expansion phase

and the contribution from the enhanced two-cell convection (direct-driven) grow larger during the recovery phase. The conclusion explains a previous study which used AL and ASYM indices and found that indices from different latitudes have different responses that were either correlated or uncorrelated with solar wind [*Clauer et al.*, 1983].

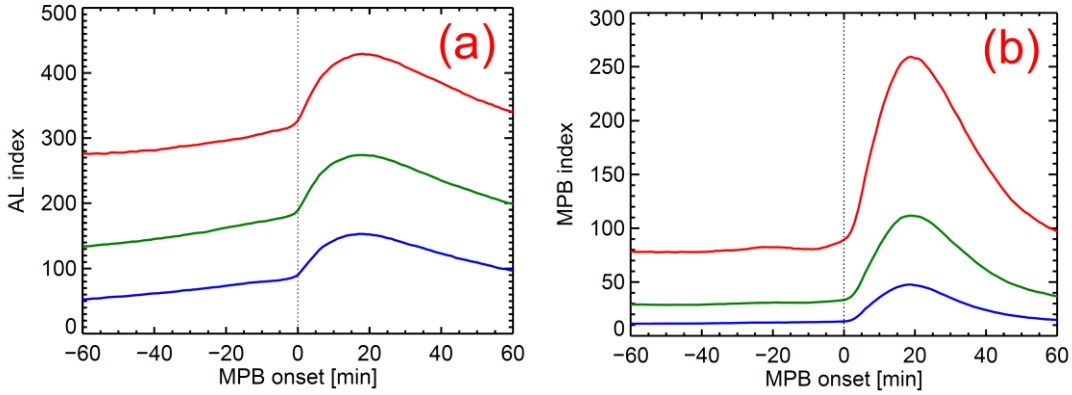

Figure 2.9. Superposed epoch analysis of (a) AL index and (b) MPB index at MPB onset.

2.4.4 Summary and conclusion:

In this chapter, an MPB index has been created to measure the strength of the SCW. A database of substorm onset was developed using the MPB index and refined by original magnetic field data. The MPB onset list exhibits good correlations with auroral onsets (0.4±1.9 min) from IMAGE spacecraft and AL onsets (-0.8±5.0 min). The seasonal and diurnal variation of MPB onsets could partially be explained by the equinoctial effect (62%); the residual shows excess signal in the European sector and no clear pattern characteristic of the Russell-McPherron effect. Both the monthly number of MPB onsets and the substorm waiting time show strong dependence on solar wind speed

rather than the sun spot number, suggesting that geomagnetic activity is controlled by solar wind driving rather than dayside ionospheric conductance. On the other hand, the durations of substorm expansion and recovery phases show rather stochastic stable distribution, which is independent of solar wind condition or substorm size. This result suggests that the unloading process, which is related to flux pileup and decay in the near-Earth region, has an intrinsic pattern independent of external driving. This result cannot be resolved from the AL index because it measures both the SCW and two-cell convection, and the latter is directly driven by the solar wind.

Chapter 3

Development and Validation of Inversion Technique for Substorm Current Wedge Using Ground Magnetic Field Data

The classic substorm current wedge model represents ground and space observations of the magnetic perturbations measured during magnetospheric substorms. In this chapter, an inversion technique is developed to calculate the intensity and parameters determining the geometry of the current system using magnetic field data at midlatitudes. The current wedge consists of four segments: a sheet-like field-aligned current downward to the auroral ionosphere postmidnight, a westward current across the auroral bulge, an upward sheet-like current from the westward surge premidnight, and an eastward current in the equatorial plane. The model has five parameters including the total current in the wedge, the locations and breadths of the two field-aligned current sheets. Simultaneous changes in the ring current are represented by the superposition of a symmetric ring current and a partial ring current characterized by three additional parameters. Parameters of the model are determined as a function of time based on midlatitude ground magnetometers, using realistic field lines and accounting for Earth's induction. The model is validated by a variety of techniques. Firstly, it was demonstrated that the model predicts more than 80 percent of the variance in the magnetic field observations. Second it was shown that the location, width, and strength of the current wedge agree with previous estimates of these quantities. Also, changes in the intensity of the current wedge and the ring current follow

the same trends seen in the westward electrojet and the SMR indices. Third it is found that the intensity of the westward electrojet derived from magnetic measurements in the auroral zone agrees extremely well with the wedge intensity derived from midlatitude observations. Finally it was shown that spacecraft observations of the aurora correspond with the evolution deduced from the magnetic observations. This inversion model of the substorm current wedge provides a valuable tool for the study of substorm development and its relation to phenomena in space.

3.1 Introduction

The earthward bursty bulk flows (BBFs) produced by magnetic reconnection (MR) in the mid-tail transport magnetic flux and energy toward the near-Earth region [*Angelopoulos et al.*, 1992; *McPherron et al.*, 2011]. Cross-tail current disruption occurs in the near-earth region during the substorm expansion phase and is associated with BBFs. The diverted current flows along the magnetic field lines (FAC) and connect through the ionosphere as the westward electrojet. This is the classic Substorm Current Wedge (SCW) [*McPherron et al.*, 1973]. A number of substorm onset paradigms exist, but two of them can summarize the main ideas and reveal the primary observational requirements. These include the 'current disruption' (CD) [*Lui et al.*, 1990; *Lui*, 1996] and the 'near-earth neutral line' (NENL) paradigms [*McPherron*, 1991; *Baker et al.*, 1996; *Baumjohann*, 2002; *Angelopoulos et al.*, 2008a]. The synthesis scenario of MR and CD [*Pu et al.*, 1999; *Pu et al.*, 2001; *Zhang et al.*, 2007; *Pu et al.*, 2010a] suggests flow braking might yield conditions favorable for auroral expansion. Resistive MHD simulation results also

suggest that the SCW is driven by the braking and diversion of the flows [*Birn and Hesse*, 1991; 1996; *Birn et al.*, 1999]. These simulations obtain current intensities consistent with observations [*Horning et al.*, 1974a; *Kisabeth and Rostoker*, 1977; *Baumjohann*, 1982]. The intensity of the FACs depends on three factors: pressure gradients, flow vorticity and inertial current [*Sato and Iijima*, 1979; *Hasegawa and Sato*, 1980]. The inertial current is small and commonly ignored [*Birn et al.*, 1999; *Keiling et al.*, 2009; *Lui et al.*, 2010]. Observational studies suggest that the azimuthal pressure gradient [*Xing et al.*, 2009; *Xing et al.*, 2011; *Xing et al.*, 2012; *Yao et al.*, 2012] and magnetospheric vorticity [*Keiling et al.*, 2009] are the major contributors to the FACs. The precise location of the satellites relative to the source region of the SCW is essential to understanding the driving mechanism. However, the limited spatial coverage of satellites in individual substorms cannot provide sufficient information to understand the cause of the SCW. Therefore, the locations and intensity of the SCW given by the inversion technique become particularly important.

Several methods utilize ground magnetic perturbations to study the topology of the SCW: 1) the auroral zone latitudinal profile of the SCW using latitudinal distributed magnetometers [*Bonnevier et al.*, 1970; *Kisabeth and Rostoker*, 1970; *Rostoker et al.*, 1970; *Kisabeth and Rostoker*, 1971; *Oldenburg*, 1976; *Connors*, 1998], 2) the distribution of the equivalent ionospheric current (EIC) in polar region [*Amm*, 1997; *Amm and Viljanen*, 1999; *Weygand et al.*, 2011] and 3) the inversion of midlatitude magnetic data to determine the parameters of the SCW such as its location and intensity [*Horning et al.*,

1974a; *Sergeev et al.*, 1996; *Vagina et al.*, 1996; *Sergeev et al.*, 2011]. The first method focuses on the latitude and intensity of the SCW, but not the longitudinal location. The current pattern can be derived by EIC, but this method cannot distinguish the SCW from other high latitude current systems. Consequently, the technique of midlatitude inversion becomes particularly useful. This method, first accomplished by [*Horning et al.*, 1974a], used the mid-latitude positive bay (MPB) signature [*McPherron et al.*, 1973] of the SCW to obtain the parameters of several current systems including the substorm current wedge, the ring current and the partial ring current (PRC). In the original work the currents were all confined to a dipole field. Later works improved this model by using more realistic magnetic field lines constructed by T89 model [*Tsyganenko*, 1989], azimuthally distributed sheet currents [*Sergeev et al.*, 1996; *Vagina et al.*, 1996] and more sophisticated current distributions in space [*Sergeev et al.*, 2011]. The inversion model by [*Sergeev et al.*, 1996] was validated by the fact that the location of the upward FAC was consistent with the westward travelling surge [*Pytte et al.*, 1976]. However, no clear relation between the structure of the aurora and the location of the downward FAC has been reported [*Pellinen et al.*, 1995]. This is partially a consequence of inadequate temporal resolution of the auroral observations and insufficient detail in the spectrum of the auroral emissions. In addition, no one has demonstrated equality between the intensities of the westward electrojet (I_{west}) and the SCW (I_{SCW}). [*Vagina et al.*, 1997] estimated Iscw using an inversion model without geomagnetically induced currents (GIC) and compared it with Iwest obtained using a high latitude magnetometer chain with the GIC [*Kotikov et al.*, 1987]. A factor of ~1.59 rather than 1.0 was found between Iscw and

Iwest. In this chapter, it will be shown that Iscw equals to Iwest when GIC are considered in the inversion technique.

In this chapter, a technique for inverting midlatitude magnetic data is developed to determine the parameters of the SCW (locations and intensity of the SCW, RC and PRC). Several important improvements are implemented, such as the inclusion of the induced current and the removal of the SQ variation. The inclusion of the induced current brings the ratio of I_{SCW} /I_{west} from 1.6 to 1.0. The removal of the SQ variation increases the prediction efficiency by ~10% (the proportion of the total variation explained by the inversion model). The location and evolution of the SCW will be compared with auroral observations. The correlation between the I_{SCW} and I_{west} will be studied. Finally, some limitations of the inversion technique will be discussed.

3.2 Data description

In order to perform magnetic inversions, this model uses ground magnetic field data recorded by 45 stations in mid-latitude region (20°<|magnetic lat|<53°) from International Real-time Magnetic Observatory Network (INTERMAGNET) and SuperMAG with time resolution of 1 minute. Almost every MLT bin has two stations except in the Pacific and Atlantic Oceans. The magnetic field data from all the stations are transformed into HDZ coordinates. The Z-direction points toward the center of the earth, H points to the magnetic north pole; and D is roughly eastward orthogonal to H.

To compare the model results with precipitation regions with auroral features, satellite-borne global auroral imaging are used. The far-ultraviolet (FUV) instrument onboard IMAGE consists of a Wide-band Imaging Camera (WIC) and the Spectrographic Imager (SI) [*Mende et al.*, 2000]. The WIC provides the auroral observation in a broad band of wavelengths from 140 to 170 nm, which consists of mainly LBH N_2 and some N1 lines. The SI-12 channel of the SI instrument observes Doppler shifted Lyman alpha while rejecting geocoronal 'cold' Ly-α. It monitors the global scale proton precipitation with primary energy greater than 1 keV [*Mende et al.*, 2000; *Frey et al.*, 2001]. The SI-13 channel images the OI 135.6 nm emission, which is primarily produced by soft electrons [*Hubert et al.*, 2002]. The time separation between images is approximately ~2 min.

The auroral electrojet indices (SML) and symmetric ring current index (SMR) were obtained from SuperMAG [*Gjerloev*, 2012]. The SML index measures the intensity of the auroral westward electrojet and the SMR index measures the intensity of the ring current once per minute.

3.3 Model description

An inversion technique is developed to invert the ground signature of mid-latitude positive bay (MPB) to determine the location and strength of the substorm currents. The technique takes the ground magnetic field as input and finds the optimal parameters of the current system as a function of time during the expansion and recovery phases of a

substorm. In this section, I will describe the geometry of the current system, the parameters controlling the system and the principals involved in the inversion procedure.

Three major current systems contribute to the MPB signature during substorms: the SCW, the symmetric ring current and the asymmetric partial ring current. This collection of currents is illustrated in Figure 3.1. The current wedge part consists of four segments. The downward and upward FACs are represented by azimuthal sheet currents flowing along realistic magnetic field lines constructed using the Tsyganenko T89 Model. The KP index is used as an input to the T89 model to allow the field to adapt to current condition. The field-aligned currents are connected in the ionosphere by a westward line current at 120 km altitude. The tail segment, which represents the reduction of the dawn-dusk cross-tail current, flows eastward opposite to the cross-tail current. These four segments form a current loop with constant current in all segments. The ring current is azimuthally symmetric and flows along a constant L shell in the magnetic equatorial plane. The PRC has geometry similar to the SCW except that it flows along a lower L shell and the direction of all currents is reversed. It flows into the ionosphere near noon and flows out in the evening sector. There are in total 30 (5+12+12 +1) free parameters in the model: the intensities of SCW in both hemispheres(x2), PRC (x2) and RC (x1); the MLTs, breadths and latitudes of the downward and upward FACs of SCW (x3 x2 x2= 12) and PRC (x3 x2 x2= 12); and the L shell value of RC (x1). The numbers of the parameters can be reduced by setting less significant parameters to fixed values. This is discussed in following paragraphs.

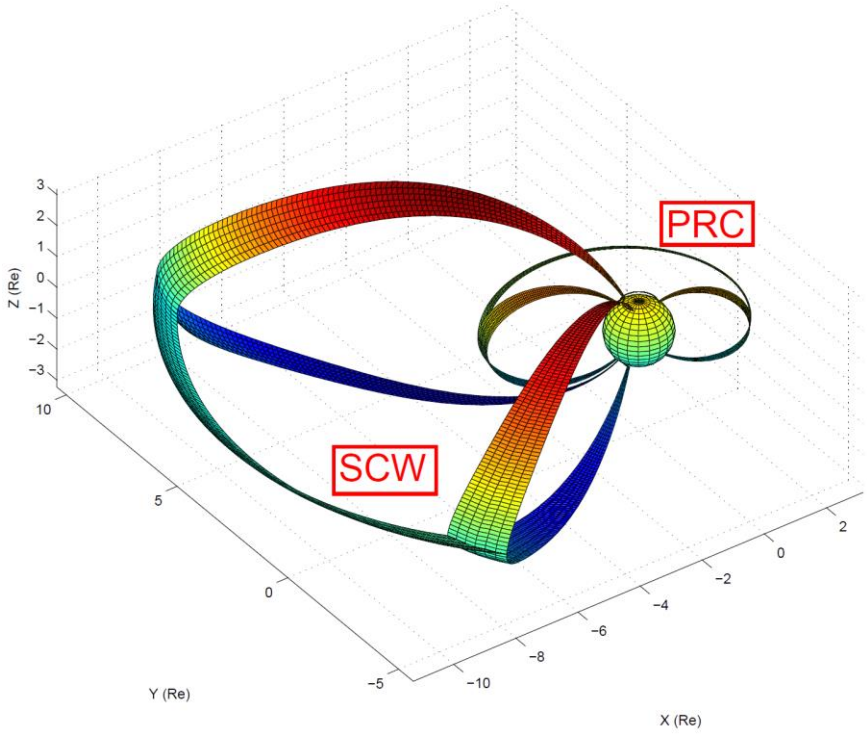

Figure 3.1 3-D schematic diagram of model current system during the substorm expansion phase. The sun is to the right. Three major current loops are included: the substorm current wedge, the ring current and the partial ring current. The ring current overlaps with the partial ring current and is not shown.

The inversion technique determines the optimal parameters for the current system using a non-linear fitting procedure called Levenberg-Marquardt algorithm [*Markwardt et al.*, 2009]. This technique takes mid-latitude magnetic field data as input, and outputs the optimal fit of the parameters for the current system. The temporal resolution of both the input of magnetic field data and the output of the parameters is one minute. As mentioned in the description of the current system, there are too many free parameters to

be resolved by the available ground stations. Also some parameters are not totally independent of others. In order to avoid over-fitting and achieve physically reasonable results, several constraints are applied to the parameters. 1) Due to the relatively sparse data in southern hemisphere, it is assumed that the current system is symmetric in both hemispheres. 2) The downward FAC of the SCW should be located eastward of the upward FAC. Similarly, the upward FAC of the PRC must be east of the downward FAC. 3) The ionospheric current of the SCW flows along constant corrected magnetic latitude of 66 degrees. The ionospheric current of the PRC flows along 60 degrees in corrected magnetic latitude. 4) The L shell of the RC is fixed at L = 4. 5) The width of the PRC is set to 12 hours in MLT. 6) The breadths of the FACs of PRC are fixed to 2 hours in MLT. After applying all the constraints, there are a total of eight free parameters left (I_{SCW}, I_{RC}, I_{PRC}; MLT_{in}, MLT_{out}, $breadth_{in}$, $breadth_{out}$, MLT_{PRC}). Further simplifications can be applied. For instance, the breadths of the FACs of the SCW can be set to fixed values. It should be noted that: 1) the breadths of the FACs are less well fitted parameters because the mid-latitude stations are far from most of the currents. The breadths are more reliable when data from higher latitude regions are available. 2) The parameters of the PRC are only crudely approximated as the current is not the focus of this chapter. The changes in the PRC are small compared to the changes in SCW and RC.

Given the parameters defining the current system, the magnetic disturbances at the locations of the magnetometers are calculated using the Biot-Savart Law. However, since the earth's surface is a conductor, the surface magnetic field is modified by currents

induced in the ground. There are several ways to calculate the magnetic effect of the induced currents (see discussion section). In the current inversion model, the effects of induced currents are calculated approximately using a procedure developed by [*Kisabeth and Rostoker*, 1977; *Mareschal and Kisabeth*, 1977] in which a perfect conducting layer is placed at 250 km below the ground surface. Inclusion of the induced currents in the model is essential because it reduces the total current inferred in the wedge by almost 60% and brings its value close to that inferred from auroral zone measurements (See Section 5 for details). To minimize the possible contamination of the magnetic field data by the solar quiet day variation (SQ variation) in the dayside region, a quiet time background is subtracted from the original data. To calculate the quiet time background, the running average of 21 days centered on Jan 11, 2002 is obtained from the original magnetic field data. The quiet time intervals in each day are found and the active intervals are flagged. A SuperPosed Epoch Analysis (SPEA) is performed on a data ensemble of 21 days to get the quiet time background. In addition, the initial value of the magnetic field at the substorm expansion onset is subtracted to minimize the contribution from other magnetospheric current systems. This time is identified as the earliest onset of an increase in H accompanied by a change in D seen anywhere in the night sector. As a result, the inversion technique gives the relative change of the SCW, RC and PRC from the onset, rather than their absolute values.

3.4 Substorm event on 11 January 2002

In this section, the SCW inversion technique is applied to an isolated substorm at

1658 UT on Jan 11, 2002. Figure 3.2 shows midlatitude observations in the interval 1650-1750 UT during the expansion and recovery phase of a substorm. The top two panels present the absolute value of the SML (SuperMag AL index) and the SMR (SuperMag Ring Current index) indices. The bottom two panels display original H and D components measured by midlatitude stations as a function of universal time. The H components in northern and southern hemisphere have the same polarity while the D components have opposite polarity. Therefore, the D components from stations in southern hemisphere are reversed for clearer illustration. In the last two panels, each trace is offset by 5 nT and sorted by MLT. From top to bottom, the traces are observations from noon, dusk, midnight, dawn and noon. Red lines represent observations from near midnight. H components near midnight start to decrease gradually from 1600 UT (not shown), and drop to a minimum around 1657 UT. This is a signature of substorm growth phase [*McPherron*, 1972]. It is followed by a sharp increase in the H components in the nightside region. D components changes are positive before midnight and negative after. These signatures of the MPB indicate the substorm expansion onset takes place at 1658 UT. However, the SML index is greater than 400 nT before 1708 UT when no activity is observed at midlatitudes. The ongoing substorm activity is observed by the SML index at 1708 UT, which is 10 minutes after the substorm onset. This delay is because of the lack of AE stations in the UT interval where the substorm takes place. The SML index reached a maximum at 1716 UT and started to decrease. This is the start of substorm recovery phase.

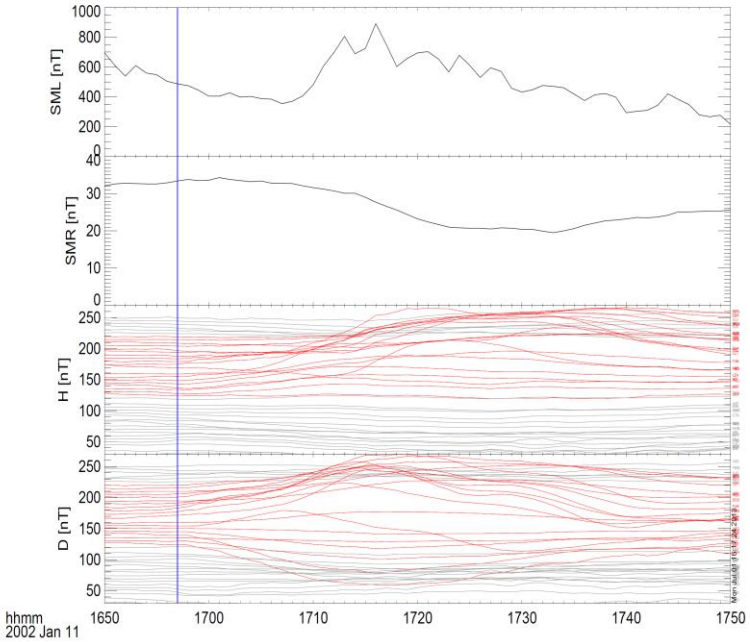

Figure 3.2 One hour observations (1650 – 1750 UT) of an isolated substorm on Jan 11th, 2002. Shown are the absolute value of SuperMAG AL index (SML) and SuperMAG Sym-H index (SMR) in the first two panels; magnetograms of H and D components from mid-latitude stations in the bottom two panels. The lines are offset and sorted by MLT. From top to bottom, the data are from noon, dusk, midnight, dawn and back to noon. The D components from stations in southern hemisphere are reversed. The blue vertical line marks the substorm onset.

Figure 3.3 shows the inversion results for this substorm during the interval 1655 UT to 1735 UT. The results include: 1) the current strength of the SCW (blue) and the RC (red); 2) and 3) the magnetic local time- universal time contour map (MLT-UT map) of H and D components [*Clauer and McPherron*, 1974a; b]. The background SQ variation is

subtracted from H and D components. On top of the contour map are the MLTs of the two FACs of the SCW. As indicated by the MLT-UT map, the H component shows positive changes in the pre-midnight region from 2000 MLT to 2400 MLT. In the same local time region, the D component shows positive change towards dusk and negative change towards dawn. The observations are consistent with the expected signatures of an MPB. This is evidence that the SCW was located in this MLT region. As shown by the inversion results, the downward FAC first formed around 2230 MLT. It expanded eastward reaching the most eastward point of 0018 MLT at 1703 UT. Subsequently it moved back toward 2300 MLT. The upward FAC formed at about 2100 MLT, and then expanded westward continuously during the substorm. It passed dusk (1800 MLT) at 1720 UT, and expanded further westward. The intensity of the SCW increased continuously after the onset, and reached a maximum of ~1 MA at 1717 UT and a second peak at 1721 UT. The rate of increase was ~ 1.0 MA / 21 minutes = 0.048 MA/min. The RC decreased by 0.35 MA relative to the value at the onset. The last panel shows the prediction efficiency, which is the ratio between the explained sum of squares (SSE) to the total sum of squares (SST). It represents the proportion of the total variation explained by the inversion model. The prediction efficiency is always larger than 70%. The prediction efficiency is larger in the middle of the substorm from 1710 – 1720 UT when the signal to noise ratio is largest. It is lower during the early expansion phase and the substorm recovery phase.

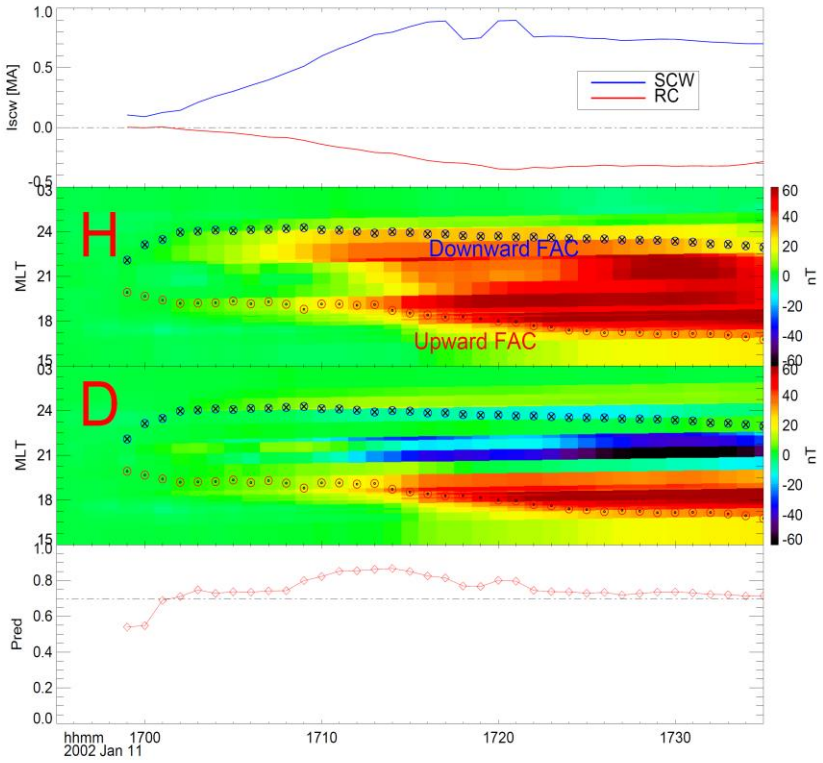

Figure 3.3 The parameters of the SCW from the inversion technique from 1655 – 1735 UT on January 11, 2002. Panel one shows the current strengths of the SCW (in blue) and the change in RC (in red). The contour map in the middle two panels are MLT-UT map of the H and D components. On top of the contour maps, the symbols represent the locations of the downward FAC (MLT_{in} in blue) and upward FAC (MLT_{out} in red) as a function of UT. The bottom panel displays the prediction efficiency of the model.

Figure 3.4 presents polar-view of auroral observations by the WIC imager at the following four selected times: 1658:15 UT (before the onset), 1700:18 UT (after the brightening), 1710:33 UT (the most eastward auroral expansion) and 1720:48 UT (the

auroral expansion reached dusk and continued travelling westward). Noon is at the top, midnight is at the bottom, dawn is at the right, and dusk is at the left. Before the onset, a pre-existing auroral arc extended between dusk and dawn at 1658:15 UT. Two minutes later (1700:18 UT), an auroral intensification was observed premidnight on the pre-existing arc around 2200 MLT. The auroral onset was identified at 1700:18 UT [Frey, 2004]. The onset actually takes place between 1658:15 UT and 1700:18 UT because of the 2-min resolution of the WIC imager. The ground MPB signature starts at 1658 UT, two minutes earlier than the auroral onset seen by the IMAGE spacecraft. After the onset, the aurora continued to brighten and expanded both westward and eastward. The eastward edge of the aurora reached its most eastward location around 0030 MLT at 1710:33 UT. After that, the eastward part of the aurora began to dim, and it became almost invisible by 1720:48 UT. The westward travelling surge was formed at onset. At 1720:48 UT, the surge reached dusk and continued its westward expansion. The footprints of the downward and upward FACs are represented by red and blue squares. The downward FAC moved eastward in association with the eastward expansion of the aurora. The upward FAC also travels westward as the WTS expands westward. The footprints from the inversion results are in good agreement with the auroral observation. A detailed study of their correspondence is interpreted with ewogram in the following paragraphs.

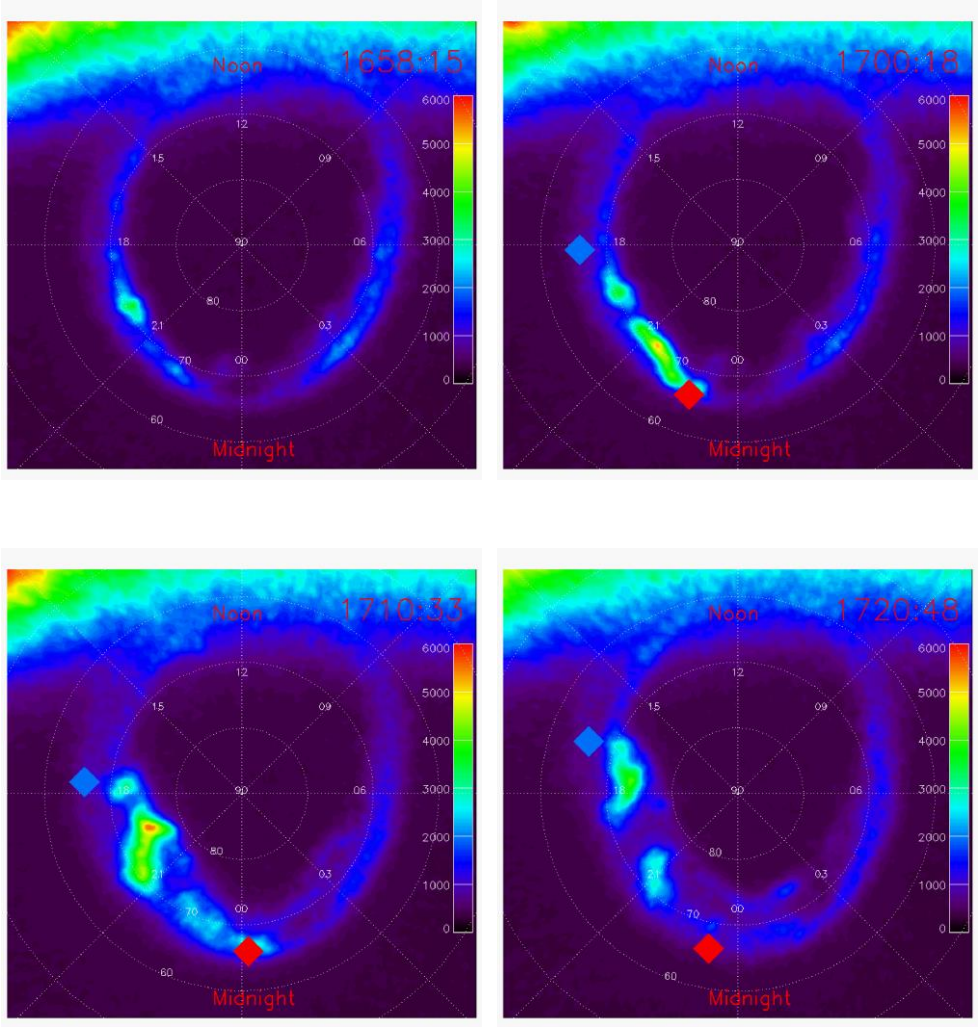

Figure 3.4 Four consecutive auroral polar views from the WIC imager by FUV onboard IMAGE at 1658:15 UT (before the onset), 1700:18 UT (after the brightening), 1710:33 UT (the most eastward auroral expansion) and 1720:48 UT (the auroral expansion reached dusk and continued travelling westward). The color bar of the count value is shown in the first snapshot. The locations of the downward and upward FACs are marked by red and blue squares.

Figure 3.5a shows the ewogram (east-west-o-keogram [*Donovan et al.*, 2006]) of the auroral observations from the WIC imager during this substorm. The color indicates the mean value of the brightness in each MLT bin of 0.2 hour integrated from 60° to 80° magnetic latitude. The locations of the downward and upward FACs obtained by the inversion are shown as black lines. Expansion of the aurora both east and west is clear in the ewogram. At the onset the west edge of the aurora formed at 2030 MLT, and then expanded westward. The WTS passed dusk at 1720 UT. The speed of the WTS is 2.5 MLT / 20 min, or ~1.9 degree/min. The eastward edge of the aurora was initially located around 2300 MLT, and then expanded eastward after the onset. The eastward expansion reached a maximum of 0030 MLT at 1709 UT, with a mean speed of ~1.5 MLT /9 min or ~1.7 degree/min. The eastward expansion of the aurora had a speed comparable to the WTS but persisted for a shorter time. These expansion speeds are consistent with previous statistical result of 1.1 ± 0.45 degree/min [*Carbary et al.*, 2000]. After reaching its most eastward extent, the eastward part of the aurora started to fade after 1714:40 UT. The locations of both FACs were closely correlated with the auroral observations. The upward FAC also moved westward as the aurora expanded westward, and it corresponds to the bright spot of the WTS very well throughout the whole substorm. This is consistent with previous studies that the upward FAC collocates with the WTS [*Pytte et al.*, 1976; *Baumjohann et al.*, 1981]. The downward FAC of the SCW also moved in an eastward direction. The location of the downward FAC agreed with the eastward edge of the aurora during the expansion phase. However, when the eastward aurora faded during the

recovery phase, the location of the downward FAC diverged from the eastward edge of the aurora.

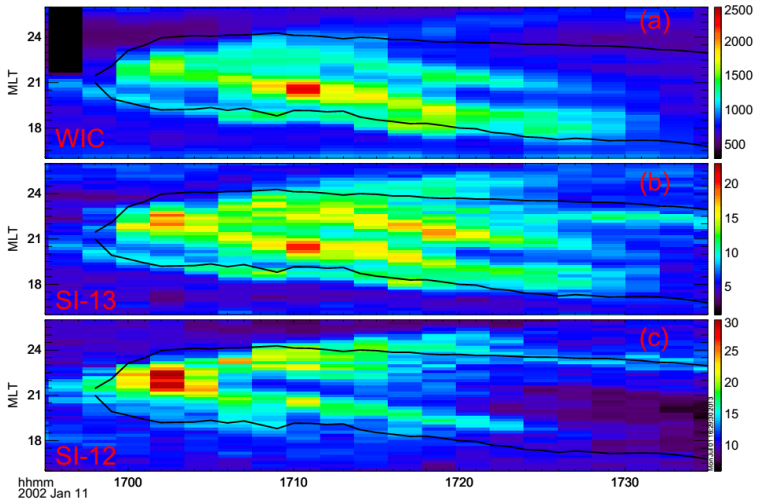

Figure 3.5 Auroral ewograms (east-west keogram) of WIC (wide-band aurora), SI-13 (electron aurora) and SI-12 (proton aurora) observed from 1655 – 1735 UT. The Y axis is MLT from 1600 - 0200 MLT. The color bar is shown for the count value of aurora. The black lines are the locations of downward and upward FACs.

The ewogram of the auroral observation from the SI-13 (soft electron precipitation) channel shows similar result in Figure 3.5b. The westward moving FAC agrees extremely well with the westward moving edge of bright aurora throughout the whole substorm. The downward FAC moves eastward along with the eastward expansion of the aurora during the expansion phase, but not in the recovery phase.

The ewogram obtained from SI-12 (proton aurora) is presented in Figure 3.5c. The proton aurora exhibited different signature from wide-band aurora or electron aurora. The eastward expansion is clear in the proton aurora, and agrees with the location of the downward FAC throughout the substorm, even in recovery phase. The westward expansion of the aurora is also clear in the proton aurora. However, there is no proton aurora but only electron aurora at the WTS because of the strong upward FAC.

In summary, the upward FAC corresponds with the wide-band and electron auroral WTS throughout the substorm, while no proton aurora is observed at the upward FAC. The downward FAC shows good agreement with the proton aurora throughout the whole substorm period. It agrees with the wide-band and electron aurora during the expansion phase and starts to show divergence during the recovery phase when the eastward wide-band and electron aurora fade.

Figure 3.6 illustrates the time evolution of the eastward equivalent current along the meridian of the IMAGE magnetometer network at a time resolution of 10 sec. The latitudinal profile of the current density in the horizontal direction is calculated using magnetic field observations from a latitude chain of magnetometers [*Vanhamaki et al.*, 2003]. The magnetometers of the IMAGE chain center at 20° in geographic longitude (magnetic local midnight at around 2130 UT). At the onset, the magnetometers are located at ~1830 MLT and thus the stations are not likely to be affected by the SQ variation on the dayside. The top panel shows the intensity of the 1-D current density for

the westward electrojet (red) and eastward electrojet (blue) versus corrected magnetic latitude as a function of time. The unit is A/m. Intensification in westward electrojet takes place at 1706 UT at 71° MLAT. The westward electrojet continues to intensify till 1720 UT while it slowly expands poleward. A quick equatorward expansion of the westward electrojet is observed at 1718 UT. However, the main westward current flows along the poleward edge. A relatively weak eastward electrojet is observed at lower latitude (62 ° MLAT) at 1705 UT. It strengthens for about 10 minutes and disappears after 1714 UT.

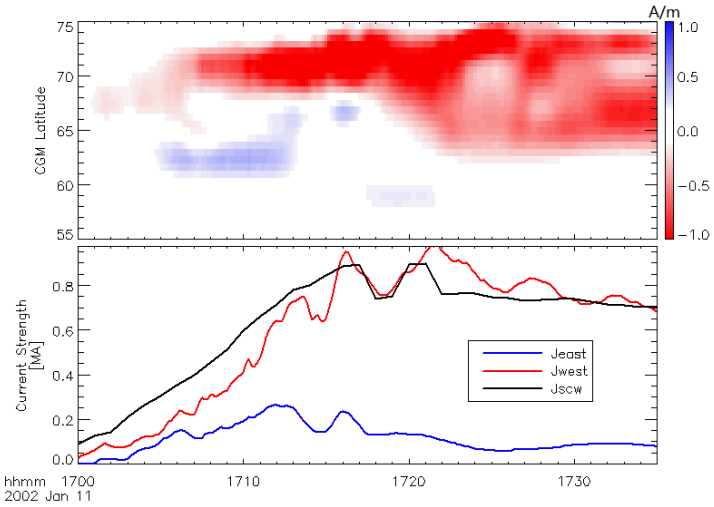

Figure 3.6 One dimensional equivalent ionospheric current (EIC) obtained using IMAGE magnetometer network from 1700 – 1735 UT. The first panel shows the contour map of the current density from 55 – 75° in corrected magnetic latitude. The unit is A/m. The second panel illustrates the current strength of the eastward (blue) and westward (red) electrojet as integrated from 1D EIC. The current strength of the SCW from the inversion technique is plotted in black.

The bottom panel of Figure 3.6 shows the integrated intensities of westward (red) and eastward (blue) electrojets. The westward electrojet shows a sudden enhancement at 1707 UT reaching its first peak of 0.95 MA at 1716 UT and the second peak of 0.97 MA at 1721 UT. The eastward electrojet flowing at lower latitude reaches a maximum of 0.26 MA at 1712 UT, which is much smaller than the westward electrojet by a factor of ~4. The intensity of the SCW is plotted in black, and is in good agreement with the intensity of the westward electrojet. There is about 10% difference between I_{scw} and I_{west} before 1704 UT, which will be discussed in detail later.

3.5 Validation

The inversion technique of SCW was validated using global auroral observations in three spectral bands, the ionospheric equivalent current and SMR index (SYM-H index from SuperMAG).

It is well established that the upward FAC of the SCW coincides with the WTS [*Baumjohann et al.*, 1981]. The auroral surge is excited by the high-energy electrons precipitating from the magnetosphere, which are the current carriers of the upward FAC. The electron aurora can be used as a proxy of the location of the upward FAC. As shown in Figure 3.5b, the electron aurora expands westward throughout the whole substorm. The location of the upward FAC also moves westward. The location of the upward FAC quantitatively agrees with the west edge of the WTS within an accuracy of one bin in MLT (0.2 hour in MLT). Considering our inversion technique uses ground data from

stations most of which are located ~4000 km from the auroral zone where the westward electrojet flows, this accuracy of < 0.5 hour in MLT is extremely good and promising. The location of the upward FAC is also in good agreement with the aurora observed by WIC as shown in Figure 3.5a. However, the upward FAC doesn't co-locate with the proton aurora observed by SI-12. The good agreement between the wide-band and electron auroral WTS and the upward FAC given by the inversion technique suggests the inversion technique is reliable.

The location of the downward FAC given by inversion is generally in good agreement with the eastward auroral expansion. Their association is more complicated because the current carriers of the downward FAC are up-going low-energy electrons from the ionosphere, which does not excite bright aurora. The precipitating protons from the magnetosphere carry much smaller current compared to up-going ionospheric electrons. Direct correlation between the location of the downward FAC and the eastward auroral expansion has not been reported in previous studies. As shown in Figure 3.5, the location of the downward FAC agrees well with the eastward edge of the aurora obtained from all three imagers onboard IMAGE during the expansion phase from 1658 UT to 1712 UT. However, different behavior in eastward expansion is observed in different spectral bands. As for the proton aurora obtained from SI-12, it agrees extraordinarily well with the downward FAC during the late recovery phase (1720 UT to 1735 UT). Although the precipitating protons do not contribute much to the downward FAC, the proton aurora can be used as a crude proxy of the location of the downward FAC. On the

other hand, the electron aurora from SI-13 also shows some agreement with the downward FAC, but not as good as the proton aurora. The wide-band aurora fades and retreats westward during the recovery phase, and no correlation is found with the downward FAC. In summary, the eastward expansion of the proton aurora during the expansion phase and the filament of the proton aurora during the recovery phase correlate well with the downward FAC.

The inversion technique is also validated against the strength of the westward electrojet calculated by a 1-D equivalent ionospheric current model using the IMAGE magnetometer network. The IMAGE magnetometer network is centered around 20° in geographic longitude and its magnetic local midnight is around 2130 UT. At the onset, the IMAGE network was located around 1830 MLT, around 2 hours to the west of the upward FAC. No electrojet was observed because the IMAGE magnetometers were not located inside the SCW at the onset. At 1706 UT it observed both a westward electrojet at high latitude (~71° in magnetic latitude) and an eastward electrojet at lower latitude (~63° in magnetic latitude). This is the signature of the Harang Discontinuity. The westward electrojet slowly expanded poleward during this substorm. At 1718 UT, it suddenly expanded equatorward and the eastward electrojet disappeared. This is mainly a spatial effect due to the westward movement of the westward electrojet along with the upward FAC. It suggests that to the east of the upward FAC, the westward electrojet spans a very large range in latitude, and no eastward electrojet exists. Nevertheless, the majority of the westward electrojet flows at the poleward boundary. The integrated intensity of the SCW

(I_{scw}), shown with a black line in Figure 3.6, displays very good agreement with the intensity of the westward electrojet (I_{west}, red line in Figure 3.6) during the substorm. Notice how the variations in the two current intensities correlate with each other; especially at two similar peaks (at 1716 UT and 1722 UT respectively) and one bottom (at 1718 UT). The correlation between the I_{scw} and I_{west} is shown in Figure 3.7a. The correlation coefficient between I_{scw} and I_{west} is 95.4%. However, it should be noted the curve is below the identity line (y=x) before 1716 UT which indicates that I_{west} is smaller than I_{scw} from the onset. The difference between I_{scw} and I_{west} can be explained by the fact that the IMAGE chain is not measuring the whole westward electrojet. The upward FAC has finite azimuthal breadth. Part of the westward electrojet is diverted out of the ionosphere before reaching the IMAGE network. Therefore when the IMAGE network is located within the upward FAC, only the portion of the westward electrojet flowing past IMAGE network is measured. Therefore, it is expected that the I_{west} is smaller than I_{scw}. They should be equal to each other if the upward FAC moves fully westward to the IMAGE network and the whole westward electrojet flows across the IMAGE chain. Figure 3.7b depicts the ratio of I_{west} to I_{scw}. The ratio increases from the onset and reaches 1.0 around 1716 UT. Thereafter it stays close to 1.0 meaning that I_{west} equals I_{scw}. In other words, the IMAGE network only observes part of the westward electrojet at the onset. As the upward FAC transverses the IMAGE network, more westward electrojet is measured. Until at 1716 UT when the whole upward FAC passed the IMAGE chain, and I_{west} equals to $I_{scw.}$ By including the induction effect, the total current I_{scw} inferred from the model is reduced by almost 60%, and quantitatively agrees with the intensity of the westward

electrojet I_{west} measured from auroral zone (see discussion section).

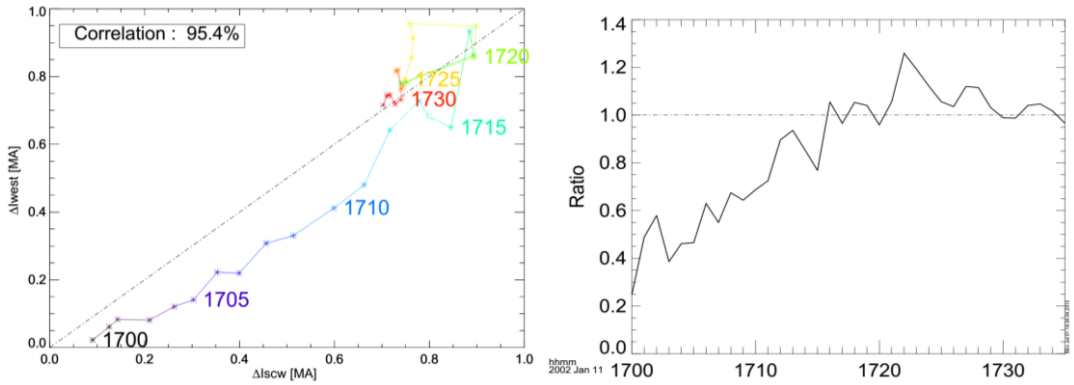

Figure 3.7 a) Correlation between the current intensity of the SCW (I_{scw}) and the integrated westward electrojet (I_{west}) using 1-D EIC. The time stamp is every 5 minutes. The dashed line is the identity line (y=x). b) The ratio of I_{west} to I_{scw} as a function of UT from 1700 – 1735 UT.

The change in the intensity of the RC (I_{RC}) obtained by inversion can be compared with the SMR index. In the top panel of Figure 3.3 it is demonstrated that the intensity of the RC decreased by 0.35 MA relative to its value at onset. The magnitude of the SMR index also decreased from ~34 nT at the onset to a minimum of ~20 nT at 1732 UT as illustrated in Figure 3.2. This correlation between the $|I_{RC}|$ and |SMR| is plotted in Figure 3.8. The correlation coefficient is 95.2% during 1700UT to 1722UT. Thus changes in the intensity of the RC inferred by the inversion are in very good agreement with changes in the symmetric ring current index SMR.

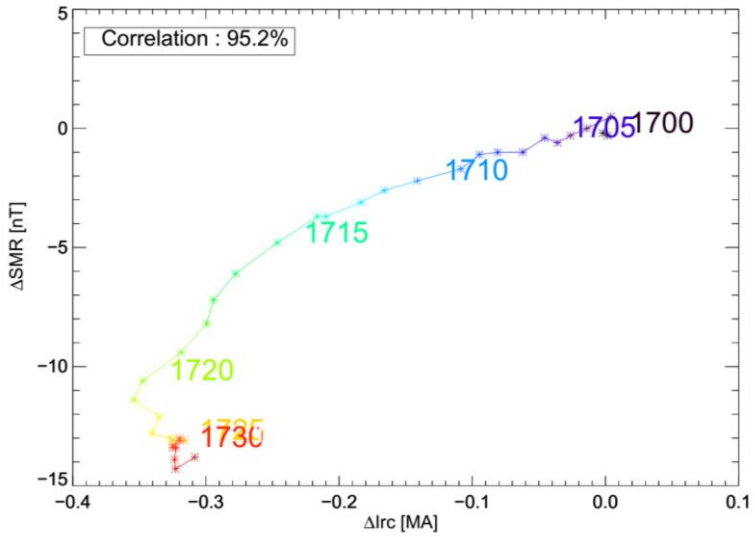

Figure 3.8 Correlation between the changes of current strength of the RC (ΔIRC) with the SMR index (ΔSMR) relative to their values at onset. The time stamps are every 5 minutes.

In this section, the results of the inversion technique were compared to other observations and very good agreement was found: 1) the locations of the FACs of the SCW and its evolution were validated using global auroral observations; 2) the intensity of the SCW (in another word, the intensity of the upward FAC) was validated against the intensity of the westward electrojet from 1-D equivalent ionospheric current; 3) the intensity of the ring current was correlated with the symmetric ring current index SMR.

3.6 Discussion

In this chapter, an inversion technique to determine the parameters of a modeled SCW is developed. This technique utilizes a non-linear fitting procedure to fit magnetic

disturbances in the mid-latitude region. It outputs the locations and intensity of the SCW and intensity of the RC. The two major improvements over previous work in our inversion technique are: 1) the magnetic effect of the geomagnetically induced currents is included with theoretically realistic model; 2) The background SQ variation is removed from the original magnetometer data.

The induction effect is generated by the response of the conducting earth to the magnetospheric currents. It increases the horizontal magnetic perturbation while reducing the vertical component. Therefore, to accurately evaluate the magnetic field perturbations, the induction effect must be considered. A major problem encountered when modeling the induction effect on a global scale is that the curvature of the earth is not negligible compared to the scale of the current system. Therefore, the previous method of using a flat conductor layer to calculate the induction effect is not applicable in the mid-latitude region. There are several ways to evaluate the induction effect on the Earth's sphere: 1) consider the earth's surface as several conductor layers with finite conductivity at different depths; 2) consider the earth's surface as a perfect conductor layer below the earth [*Mareschal*, 1976]; 3) multiply the horizontal magnetic perturbations of the source current by a constant of roughly 1.59 [*Mareschal and Kisabeth*, 1977; *Vagina et al.*, 1996; *Sergeev et al.*, 2011]. The third method can estimate the combined horizontal fields of the source and induced currents, but not the vertical component. In reality, the vertical component is reduced rather than enhanced. Although this method is qualitatively correct, it is not quantitatively accurate. The amount the H and D components change by adding

induction effect varies from 1.4 to 2.0 depending on distance relative to the SCW as a function of both longitude and latitude. Therefore, the ratio of ~1.59 is a mixed effect of different magnetic components from different magnetometers. Among three methods, the first one of using several conductor layers has the best accuracy but consumes more computation time. Compared to the first model, simulating the induction effect by assuming the earth as a perfect conductor has two advantages. First, it gives a theoretically simple analytic equation which saves enormous computation time. Second, the equation is independent of temporal variation of the source currents, so the induced field is in phase with the source field without any time lag. The instantaneous combined field (source field and induced field) can be calculated without considering the time delays present in finite conducting layers. Therefore, in the current inversion model, a perfect conducting layer underneath is used to represent the induction effect by the geomagnetically induced currents. By including the effect of geomagnetically induced effect, the current strength I_{scw} needed to produce magnetic perturbation of same magnitude is reduced by ~60%. In the validation section, good agreement between I_{scw} and I_{west} is found as shown in Figure 3.7. They quantitatively agree with each other. This result indicates the importance of the induction effect in the inversion technique.

The removal of the baseline from the magnetic field is essential in the current inversion technique. The baseline is produced by the ionospheric currents in the dayside region. The magnetic field can change by tens of nT in 6 hours, i.e. > 10 nT/hour. The magnetic perturbation of the SCW in the mid-latitude region is usually ~15 nT in ~20

min in the nightside sector corresponding to about 45 nT/hour. The SQ variation can therefore produce effects that are ~20% of the magnetic perturbation of the SCW. The effect of the SQ variation grows as substorm develops and reaches a maximum at the end of the substorm. Thus, the removal of the SQ variation is significant in reducing the contamination and increasing the signal-to-noise ratio during late substorm phase. In our inversion technique, the magnetic perturbation in the dayside region is mainly contributed by the RC and the PRC. Hence, the signal-to-noise ratio in the data is important in calculating the parameters of the RC and PRC, especially PRC. A separate inversion was performed where the SQ variation was not removed from the original magnetic field data. During the recovery phase, the prediction efficiency was ~66% for this run, much lower than ~73% obtained when the SQ variation was removed. As a result, the accuracy of the parameters of the inversion technique are significantly improved by removing the baseline from the original data.

A possible problem of the inversion technique is that the non-linear regression might converge to a local optimum rather than a global optimum. It will be demonstrated that by applying the constraints described in the modeling section, the inversion technique always converge to a global optimum. Figure 3.9 shows the contour of the prediction efficiency as a function of the locations of two FACs (MLT_{in} and MLT_{out}). For every coordinate of (MLT_{in} and MLT_{out}), the prediction efficiency is obtained by fitting other parameters. Assuming the width of the SCW to be larger than 1 hour in MLT ($MLT_{in} - MLT_{out} \geq 1$), only one optimum of the prediction efficiency is found and no other

optimum point exists. This fact indicates the inversion technique will give an optimal set of parameters for the SCW without influence by the initial values.

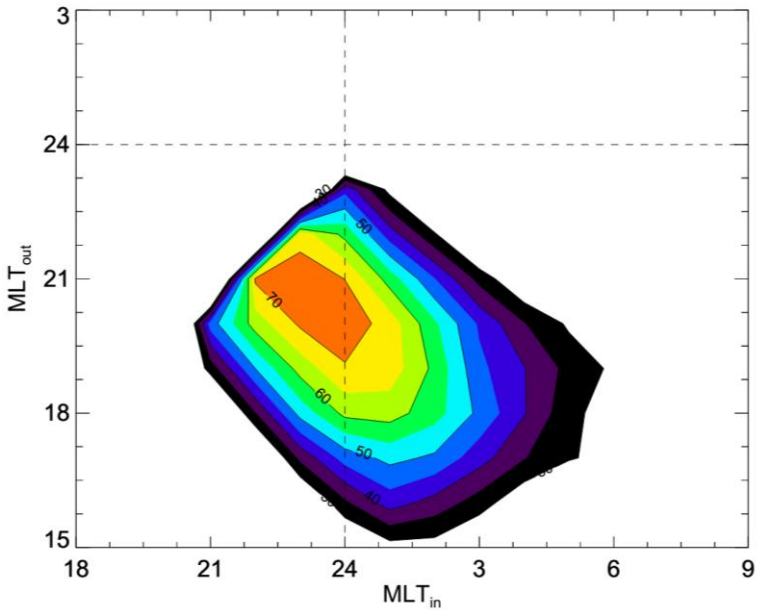

Figure 3.9 2D contour of Prediction efficiency as a function of MLT_{in} and MLT_{out}. Only one optimum of prediction efficiency is found which means the inversion technique gives an optimal set of parameters.

The errors of the inversion results are found not sensitive to the amplitude of noise. The model is first tested with a virtual SCW and 30 virtual magnetometers. The magnetometers are evenly distributed along MLT at three latitude layers of 25, 35 and 45 degrees in the northern hemisphere. Noise of different amplitudes (noise-to-signal ratio from 0% to 10%) are added to the magnetic fields obtained by virtual magnetometers. The inversion technique is then applied to the virtual observations. The inversion results

are then compared with the parameters of the virtual SCW. The relative change of the intensities of the SCW and RC are much less than the noise-to-signal ratio. For noise-to-signal ratio of 10%, I_{scw} and I_{rc} are changed by less than 3%. The relative change of locations of the FACs is less than 1 degree in longitude. The inversion technique is then tested with realistic observations. Then, noise was added (noise-to-signal ratio = 10%) to the magnetic observation at 17:08 UT from the substorm event. The intensities of I_{scw} and I_{rc} is changed by less than 4% while the locations of the FACs is changed by less than 1 degree in longitude.

The pattern of magnetic perturbations created on the ground by the substorm current wedge is very smooth because of the distance of the midlatitude stations from the various segments of currents and their images. As a general rule fine structure in the currents cannot be resolved because spatial smoothing characteristic of any potential field blurs details. Because of this our model is deliberately simple consisting of uniform sheets of fixed width centered at a given longitude. No attempt was made to estimate fine structure within the sheets as it is invisible at large distances. The errors is estimated in the central locations of the up and down sheets using the bootstrap method. Normally 45 stations are used in our inversion. From these stations, I randomly select 35 stations and perform the inversion on observations of this substorm. The same procedure was repeated 200 times and a histogram of the locations of the centers of the two sheets is created. The standard deviation for the downward sheet current is 0.33 hours in MLT, and for the upward

current it is 0.37 hours in MLT. The same procedure is repeated using data from different numbers of stations from 22 to 40. The standard deviations appear to decrease linearly as the number of stations increases changing from 0.6 with 20 stations to 0.2 with 40 stations. Therefore it is concluded that the inversion returns locations with errors that most of the times are close to the average separation between stations.

There are several factors that should be considered in applying this inversion technique:

First of all, the accuracy of the inversion technique depends on the signal-to-noise ratio. In our inversion technique, the original local time profile of magnetic perturbations is subtracted from all profiles after onset. In other words, the inversion technique uses the relative changes in the input data as a function of time after the onset. At onset, the signal-to-noise ratio is low because the magnetic perturbation is small. During the recovery phase, the decay of the magnetic perturbations produced by the SCW and possible growing contamination from an incompletely removed SQ variation result in a decrease of signal-to-noise ratio. In addition, the current system may become more complicated during the recovery phase so that it is not well represented by our model. This also reduces the signal-to-noise ratio. Therefore, the accuracy of our inversion technique is relatively high in the middle of the substorm when the magnetic perturbations are high. It is relative low at the start of the substorm and during late recovery phase. This is consistent with the prediction efficiency as shown in the bottom panel of Figure 3.3Figure 2.5.

Secondly, this inversion technique works under conditions when the major magnetic perturbation is produced by the SCW, the RC and the PRC. For instance, it also works during magnetic storms when the RC dominates. However, during highly disturbed period when the current system is too complicated to be represented by the three current circuits, the inversion technique is unlikely to work well.

Thirdly, although the locations of the FACs correspond to the auroral expansion very well, the current inversion technique cannot be used to examine the fine structure of the aurora or the field-aligned currents in the auroral oval, which may be related to localized structures in the tail [*Nakamura et al.*, 2001; *Liu et al.*, 2013a]. Previous studies suggest the structure of the FACs might be complicated both spatially and temporally. Multiple auroral onsets are observed during one substorm in different locations [*Chu et al.*, 2010a; *Pu et al.*, 2010a]; the aurora brightening corresponding to the downward and upward FACs are patch-like, which implies the FACs might be stripe-like [*Murphy et al.*, 2012]. The current inversion technique takes the mid-latitude magnetic perturbation as input. This process is a form of remote-sensing, which measures the integrated effect of the sheet currents of the SCW. Therefore, fine structure of the FACs cannot be studied unless in-situ measurements near the auroral oval or in space are used.

Fourth, the latitudes of the FACs are assumed to be located at 66°, which is quoted from the most probable latitude of the auroral brightening [*Liou et al.*, 2001; *Frey et al.*, 2004]. In this inversion technique, the magnetic latitude of 66° is used to be consistent with previous inversion models [*Horning et al.*, 1974b; *Sergeev et al.*, 1996]. This

assumption is not necessarily true for all substorms. The latitude of the auroral oval changes during the expansion phase as a function of both MLT and the intensity of geomagnetic activity [*Holzworth and Meng*, 1975]. Good agreement was found between the locations of the FACs and aurora, strength of SCW and westward electrojet. These facts suggest this assumption works well for the substorm in the current inversion model. Previous studies show that the latitudes of the FACs could be inferred from magnetic disturbances observed at higher latitudes [*Kisabeth and Rostoker*, 1971; *Rostoker and Kisabeth*, 1973; *Kisabeth and Rostoker*, 1977; *Connors*, 1998]. However, the structure of the ionospheric currents and the aurora could be very complex and localized, therefore special care is required to calculate the latitudes of the FACs. Determining the latitudes of the FACs using higher latitude stations will be studied in the future work.

Fifth, another current wedge model has been proposed [*Ohtani et al.*, 1990; *Birn et al.*, 1999] (see Figure 10 in Ohtani or Plate 4 in Birn]. In this new model the substorm current wedge as originally proposed is accompanied by an additional wedge of opposite sense flowing on a lower L-shell, but located in the same meridians as the current wedge. In the ionosphere the downward current in the outer L-shell splits with a fraction flowing equatorward and the remainder flowing westward. The reversed current wedge on the lower L-shell partially closes radially in the magnetosphere; outward post-midnight and inward premidnight. The remaining portion of this current closes westward in the equatorial plane as a partial ring current centered around midnight. Note that the diagram shown by [*Birn et al.*, 1999] has since been modified to include a westward segment in

the magnetosphere [personal communication]. A 2-loop model has also been proposed by [*Sergeev et al.*, 2011], who suggest all the inner loop current closes westward in the magnetosphere and does not speculate about the ionospheric closure. [*Ritter and Lühr*, 2008] have yet another version of this model. In this version there is no connection between the two loops either in the ionosphere or in the magnetosphere. Instead the inner loop is closed as a sheet current flowing eastward at midlatitudes. It should be noted that the lower current loop is suggested to be associated with dipolarization and flows in the tail [*Sergeev et al.*, 2011]. It is different from the PRC in other models which is connected to the ring current [*Crooker and McPherron*, 1972; *Tanaka et al.*, 2010; *Hashimoto et al.*, 2011].

It should be emphasized that the preceding 2-loop system cannot be detected by midlatitude magnetometers. If all current in the outer loop closes along a meridian in the ionosphere there would be no westward Pedersen current in the auroral bulge and the magnetic effects of the two loops would cancel each other at midlatitudes. If the current in the outer loop splits as described above the lower loop will partially cancel the effects of the outer loop and the total inferred current will be the difference in current between the two loops. Our current understanding of the high latitude electrodynamics is too poor to determine whether the westward electrojet in the auroral bulge is all Pedersen, all Hall, a combination of the two, or is a Cowling channel. The easiest way to prove that two loops would be to place spacecraft simultaneously between the two loops and inside both loops. Inside the double loop system there would be very large magnetic perturbations

compared to regions inside the loops.

The inversion technique of the SCW is an important tool for studying the driving mechanism of the FACs of the SCW. It can be universally applicable to studying the currents of the SCW system in any region with sufficient magnetic observations. Further statistical work of the SCW using the inversion technique is planned to study the general properties of the SCW and its dependence on the solar wind driving condition. This model might supplement to the models of Earth's magnetosphere such as Tsygenenko model during substorm periods and improve mapping technique. Besides, knowledge of the relative locations of the flows relative to the source region of the SCW is essential to understanding the driving mechanism of the SCW. I aim to study the correlation between flows and SCWs by taking the advantage of the inversion model in the future work.

3.7 Summary

In this chapter, an inversion technique to determine the parameters of a modeled SCW was developed. It takes magnetic observations from mid-latitude stations and gives reliable parameters for the intensity and locations of the FACs of the SCW and intensity of the RC:

1. The locations of the FACs given by the inversion technique are consistent with auroral observations in different spectral bands. The upward FAC of the SCW lies on the brightest spot of the WTS throughout the substorm period. There is no proton aurora near the upward FAC because there is no proton precipitation.

2. The location of the downward FAC is in good agreement with the auroral eastward expansion during the expansion phase. Good agreement is also found between the proton aurora and the downward FAC. Divergence between the downward FAC and the wide-band and electron aurora is shown during recovery phase when the aurora in the eastward region became diffusive.

3. The intensity of the SCW from our inversion technique is compared with the westward electrojet obtained by 1-D equivalent ionospheric current (Correlation coefficient 95.4%). The good agreement suggests our inversion technique gives reliable intensity of the FACs.

4. The inclusion of the induction effect reduces the current strength of the SCW by ~60%. The intensity of the SCW inferred from mid-latitude equals to the intensity of the westward electrojet.

5. The intensity of the RC has good correlation with the index measuring the ring current intensity (SMR index, correlation coefficient 95.2 %.).

6. Evidence is presented that the SCW may have a two-loop configuration. However, it is unclear whether this model is universal to all substorms. The occurrence frequency of the R2-like current loop and its signatures need to be studied.

Chapter 4

Magnetic mapping effects of substorm currents leading to auroral poleward expansion and equatorward retreat

Magnetotail fast flows, magnetic field dipolarization and its relaxation are linked to auroral brightening, poleward expansion, and equatorward motion during substorm onset, expansion and recovery respectively. While auroral brightening is often attributed to the field aligned currents produced by flow vorticity and pressure redistribution, the physical causes of auroral poleward expansion and equatorward retreat are not fully understood. Simplistically, such latitudinal changes can be directly associated to the tailward motion of the flux pileup region and the earthward flux transport towards the dayside that depletes the near-Earth plasma sheet. However, because the equatorial magnetic field profile and the magnetospheric field aligned current system change significantly, mapping is severely distorted. To investigate this distortion, I superimposed a substorm current wedge model (dynamically driven by ground based observations) on the global Tsyganenko model T96 during an isolated substorm on 13 February 2008, observed by the THEMIS and GOES 10 spacecraft and by ground ASIs. The model is validated by showing that the timing and ionospheric projection of the flux pile-up region and flow bursts observed at the spacecraft match auroral activations. The improved mapping enabled by the model is used to demonstrate that in this event, auroral poleward

expansion and equatorward retreat were mainly caused by SCW-induced mapping changes.

4.1 Introduction

The mechanism that triggers substorms, one of the most controversial topics in space physics, suggests different spatio-temporal scenarios of substorm development. Among models based on those scenarios, the near-Earth neutral line (NENL) model and the current disruption (NECD) model have received most attention (e.g., *Angelopoulos et al.* [2008a], *Lui* [2009] and references therein). Because timing of substorm signatures (ground auroral onset, flows in the near-Earth region, and reconnection onset in the midtail) have been used to differentiate between substorm models and because those signatures vary considerably in time and space, knowledge of onset location is as important as knowledge of timing.

Auroral signatures (brightening and expansion) reflect and are connected to processes in the magnetotail such as fast flows, flux pileup and dipolarization from the flows. In the ionosphere, the aurora brightens and then expands westward, poleward, and equatorward during the substorm expansion phase [Akasofu, 1964]. Auroral brightening (auroral substorms or localized intensifications) is correspondingly associated with fast flows in the tail [*Nakamura et al.*, 2001]. Auroral azimuthal expansion, a westward travelling surge, corresponds to an expanding current wedge observed as azimuthally expanding dipolarization at geosynchronous orbit [*Nagai*, 1982b] and westward

expansion speed of the flows in space [*Angelopoulos et al.*, 2008b]. According to Nakamura et al. [1993], auroral poleward expansion is produced by tailward expansion of the onset region observed as tailward-moving flux pileup, arising from flow braking. The flux pileup region is caused by pileup of magnetic flux via flow braking and diversion [Baumjohann et al., 1999; Birn et al., 1999; Petrukovich and Yahnin, 2006]. During the expansion phase, the aurora expands poleward monotonically; at the same time, the pileup region expands tailward, as reported in previous studies [*Jacquey et al.*, 1991; *Nakamura et al.*, 1993; *Baumjohann et al.*, 1999; *Zhang et al.*, 2011; *Cao et al.*, 2012]. Auroral equatorward expansion is attributed to earthward transport of plasma from the onset region [*Nakamura et al.*, 1993; *Sergeev et al.*, 2010]. [*Tang et al.*, 2013] also studied simultaneous auroral poleward and equatorward expansion after substorm onset.

To study the relationship between the aurora and flows, dynamic changes in the magnetosphere should be considered. The hypothesis that auroral poleward expansion corresponds to the tailward expansion pileup region is strongly based on the assumption of a static magnetosphere. The magnetosphere is highly dynamic during substorms, however. Dipolarization of the main field by the SCW, changes the ionospheric footprint of the substorm onset location and thus the location of the aurora. In this chapter, it will be investigated whether the tailward-expanding pileup region or magnetic dipolarization of the SCW causes auroral poleward expansion.

Although the effect of magnetic SCW dipolarization is significant, it has not been considered in previous models for mapping. Accurate mapping has been one of the difficulties in studying the relationship between fast flows and auroral observations. Different mapping techniques apply to different circumstances. The widely used Tsyganenko model [*Tsyganenko*, 1989; *Tsyganenko and Stern*, 1996], is a statistical model that reflects the average configuration of the magnetosphere. (It underestimates tail stretching during substorm growth phase and overestimates it after the expansion phase.) The event-oriented model [*Pulkkinen et al.*, 1991; *Kubyshkina et al.*, 1999; *Kubyshkina et al.*, 2011] adjusts the magnetospheric model by fitting in-situ observations from spacecraft. This model works for the slowly-varying growth phase but it depends on the availability of in-situ measurements in space [*Sergeev et al.*, 2012]. During substorms, the largest magnetic perturbation is created by the SCW, which is highly dynamic. Therefore, the effects of the SCW on accurate mapping are non-negligible. However, how the dynamic SCW affects the mapping has not been studied in previous magnetospheric models because the location and intensity of the SCW are unknown. These parameters can be obtained from an inversion model for SCW [*Chu et al.*, 2014a] and used to evaluate the effects of the SCW.

In this chapter, the relationship between aurora and flows has been investigated by taking the effect of the SCW into consideration. During an isolated substorm event on 13 February 2008, a good spatial and temporal correlation between several flows and successive auroral brightenings was found. This is evidence that the flows were located

near the source region of precipitation causing the aurora. It is consistent with previous studies that flow vortices and azimuthal pressure gradients generated the field-aligned currents (FACs) [*Birn et al.*, 1999; *Keiling et al.*, 2009; *Yao et al.*, 2012]. Using results from the SCW inversion model [*Chu et al.*, 2014a], the flows are mapped using a dynamic magnetospheric model, which superposes the SCW model on the Tsyganenko T96 model [*Tsyganenko*, 1997]. The magnetic field is calculated by superposing the magnetic field of currents from both T96 and SCW model. It was found that the footprints of the flows followed the trend of the poleward expansion and equatorward recovery of the auroral brightenings. Thus it was concluded that the dipolarization by the SCW is the major cause of the poleward motions during substorm expansion and equatorward motions during recovery. Section 2 describes the dynamic magnetospheric model. The observations is presented in section 3 and follow with discussion in section 4.

4.2 Data and model description

From 0200 to 0400 UT on 13 February 2008, two of the identically-instrumented THEMIS probes (P3 and P4) were located in or near the plasma sheet in the premidnight region. Three second spin-averaged ion data from the probes' electrostatic analyzer (ESA) [*McFadden et al.*, 2008] and magnetic field data from their fluxgate magnetometer (FGM) [*Auster et al.*, 2008] were used. Auroral observations with a time resolution of 3 sec were obtained from the all-sky imagers (ASIs) [*Mende et al.*, 2008]. The auroral electrojet index (AE, AU and AL) was calculated from THEMIS ground magnetometers at a time resolution of 20 sec [*Russell et al.*, 2008]. The lower envelope AL index

measures the westward electrojet, which is the ionospheric part of the SCW. The GSM coordinates are used to display spacecraft locations and velocities. One min magnetic field data from GOES 10 are obtained in PEN coordinates. The Hp component, which points northward, is perpendicular to the orbit plane and essentially parallel to Earth's rotation axis. The He component is perpendicular to the Hp and Hn components and points earthward. The Hn component is normal to both Hp and He components and points eastward. Geotail (21.9 R_E, -15.5 R_E, -6.4 R_E) was upstream of the Earth and interplanetary magnetic field data (IMF) are shifted to the bow shock [*Weimer et al.*, 2003; *Weimer*, 2004].

The footprints of the flows are obtained by tracing the modified magnetic field calculated using the dynamic magnetospheric model which is a superposition of the magnetic fields of the currents in the inversion for SCW [*Chu et al.*, 2014a] and the Tsyganenko T96 model [*Tsyganenko and Stern*, 1996]. The magnetic field is calculated by superposing the magnetic field of currents from both T96 and SCW model. The solar wind input for the T96 model is obtained from the OMNI database (omniweb.gsfc.nasa.gov). The currents in T96 model is only controlled by the solar wind input. The additional currents from the inversion model consist of the SCW, the ring current, and the partial ring current, which are the dominant causes of currents in magnetic field during substorms. The SCW consists of four segments: the downward and upward FACs, the westward electrojet in the ionosphere and the tail current in the magnetic equator. The FACs are represented by sheet currents flowing along realistic

magnetic field lines calculated using the T96 model. Field-aligned currents are connected by the westward electrojet in the ionosphere at 120 km altitude. The tail current flowing eastward in the magnetic equator represents the reduction of the dawn-dusk cross-tail current. The location of the tail current is determined by tracing the auroral oval to the magnetic equator (at magnetic latitude of 66-68º depending on the local time), which generally maps to X = -8 Re to -12 Re. The radial distances of the tail parts are different at different local times because the asymmetry of the magnetosphere. Therefore, the tail part of the SCW is sheet-like as shown in Figure 4.1 in a previous paper [*Chu et al.*, 2014a]. Optimal parameters of these currents such as the intensities and locations are obtained as a function of time at 1 min resolution from the inversion model. To perform the inversion, the model uses ground magnetic field data recorded by 53 stations at midlatitudes from the International Real-time Magnetic Observatory Network (INTERMAGNET), SuperMAG [*Gjerloev*, 2012] and THEMIS ground magnetometers with time resolution of 1 min.

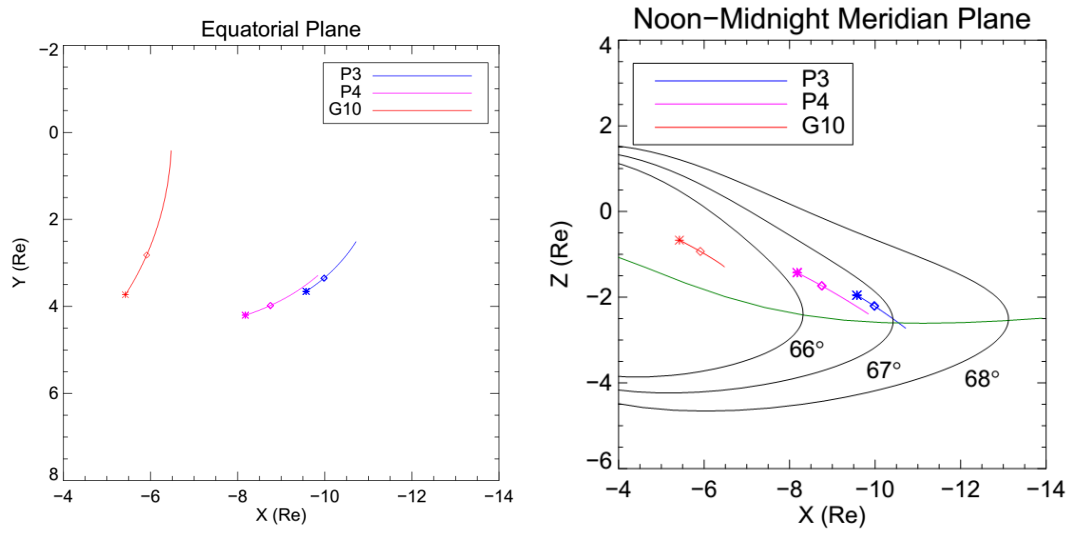

Figure 4.1 Projection of THEMIS P3 and P4 and GOES 10 in the equatorial plane (a) and noon-midnight meridian plane (b) in GSM coordinates from 0200 to 0400 UT on 13 February 2008. The starting positions at 0200 UT are marked as asterisks. The locations at onset (0237UT) are marked by squares. The magnetic equator is shown as a green line. The magnetic field lines are tracked using T96 model from the ionosphere at magnetic latitudes of 66°, 67° and 68°.

4.3 Substorm event on 13 February 2008

A moderate substorm took place at 0237 UT on 13 February 2008. Figure 4.1 shows the position of THEMIS P3, P4 and GOES 10 on the equatorial plane (Figure 4.1a) and the noon-midnight meridian plane (Figure 4.1b) in GSM coordinates from 0200 to 0400 UT. Three probes were located in premidnight region at the onset (Figure 4.1a) and

above the magnetic equator (Figure 4.1b). The field lines were tracked from the ionosphere at 66°, 67°and 68° respectively using T96 model.

Figure 4.2 is an overview of the IMF Bz at the bow shock (shifted from Geotail) (Figure 4.2a), the THEMIS AE indices (Figure 4.2b), the magnetic field and plasma velocity in GSM coordinates from THEMIS P3 (Figure 4.2c, d) and P4 (Figure 4.2e, f), and plasma betas (Figure 4.2g) from 0225 to 0320 UT. Before the substorm, the IMF Bz was negative for about half an hour. At the same time, the AL index was quiet and increasing slowly (not shown). The IMF Bz started to turn northward at ~02:31 UT. Six minutes later, a sharp decrease in the THEMIS AL index began at 0237 UT and reached a minimum of -370 nT at 0246 UT. These observations suggested this substorm was triggered by the northward turning of the IMF. Both P3 and P4 were inside the plasma sheet as the plasma β (Figure 2.3 4.2g) were greater than 1.0 throughout this event. As shown in Figure 4.2d and 2f, earthward fast flows (blue) were observed by both P3 and P4. The earthward flow observed by P3 reached a maximum of 570 km s^{-1} at 02:37:20 UT and was accompanied with transient strong magnetic fluctuations. The plasma velocity at P4 reached a maximum of ~280 km s^{-1} at 02:37:09 UT. More permanent dipolarizations (red traces, lasting longer than tens of minutes) were observed after the earthward flows by both P3 and P4. A bipolar flow signature was observed by P4, the spacecraft at larger Y, the earthward flow turned tailward and then earthward again. The bipolar flow was accompanied by strong duskward diversion, permanent dipolarization and low plasma beta. These observations are consistent with the existence of a localized plasma vortex. A second flow channel was observed around 02:50 UT. It first reached

THEMIS P4 at 02:50:15 UT at a maximum earthward speed of ~250 km s^{-1}. The same flow was observed by P3 at 02:50:21UT and its maximum velocity was ~300 km s^{-1} with strong duskward diversion. A third flow arrived at P3 at 02:54:45 UT and arrived at P4 at 02:55:18 UT. A fourth flow was observed at ~03:08 UT by P3 and P4 during the recovery phase. The Bz component continued to increase during the second, third and fourth flows but at much lower rates relative to the initial dipolarization that accompanied the first flow.

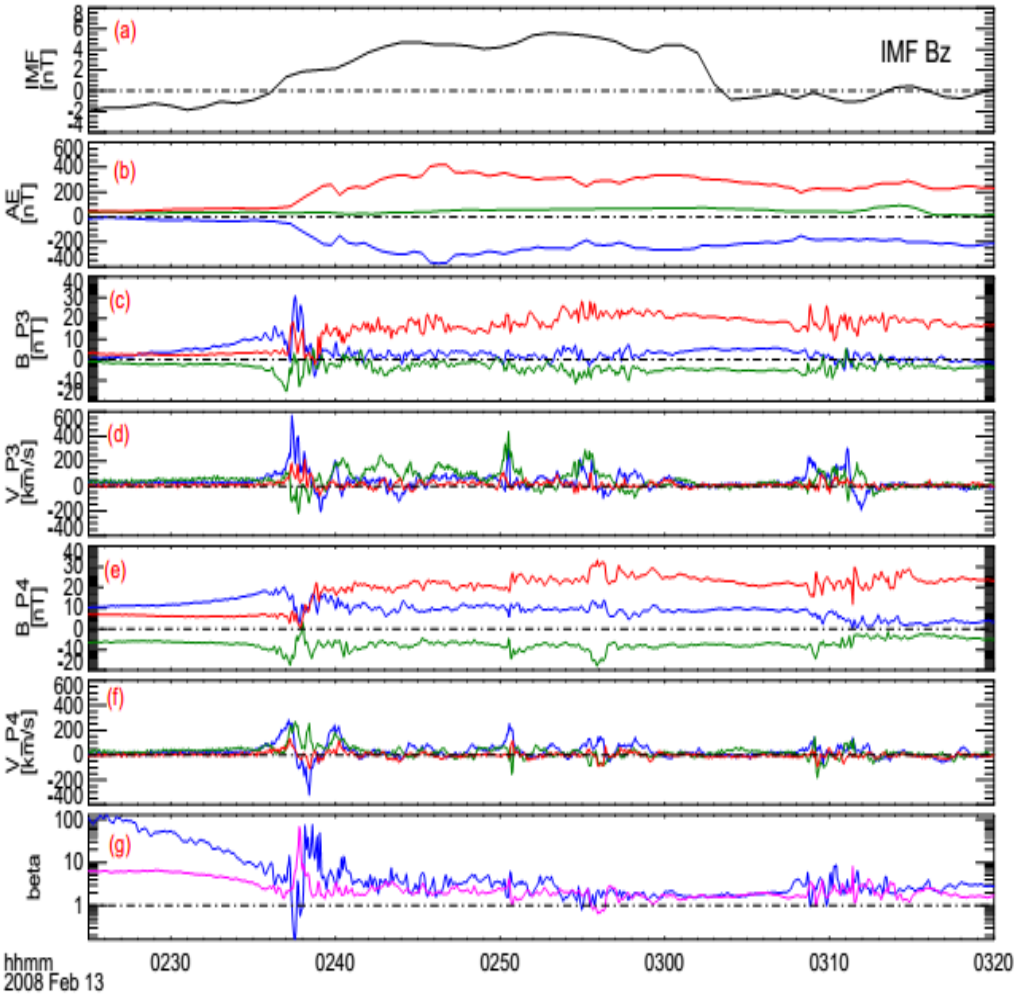

Figure 4.2 Overview of observations from Geotail, THEMIS P3 and P4 and GOES 10 from 0225 to 0320 UT. The IMF Bz at the bow shock was shifted from Geotail and shown in panel (a). The auroral electrojet indices (AE, AU and AL) are calculated using THEMIS ground magnetometers as shown in panel (b). The magnetic field and plasma velocity in GSM coordinates from THEMIS P3 and P4 are shown in the next four panels. The last panel shows the plasma beta of P3 (blue) and P4 (purple).

Figure 4.3 shows the magnetic perturbation and the magnetic inclination observed by GOES 10 at geosynchronous orbit in PEN coordinates. GOES 10 was located about 2 hours before midnight. Before the onset, the vertical component Hp decreased and the earthward component He increased. The inclination decreased at the same time indicating the development of a tail-like magnetic field. This is signature of substorm growth phase [*McPherron*, 1970]. After onset, Hp increased from 63 nT to 76 nT and the inclination increased. These changes indicate a rotation of the field from a tail-like to more dipolar configuration, i.e. a dipolarization. The dipolarization suggests that GOES 10 was located inside the SCW both radially and azimuthally: GOES 10 was located on lower L shell than the SCW and was between the two FACs in the azimuthal direction. The eastward component Hn experienced a positive perturbation similar to that seen at midlatitudes west of the central meridian. This is the evidence that GOES 10 was located near the upward FAC. Unlike general geosynchronous dipolarizations [*Nagai*, 1982b; *Ohtani et al.*, 1992b], this dipolarization was preceded by a dip in the Hp component. A possible interpretation of this change is presented in the discussion section.

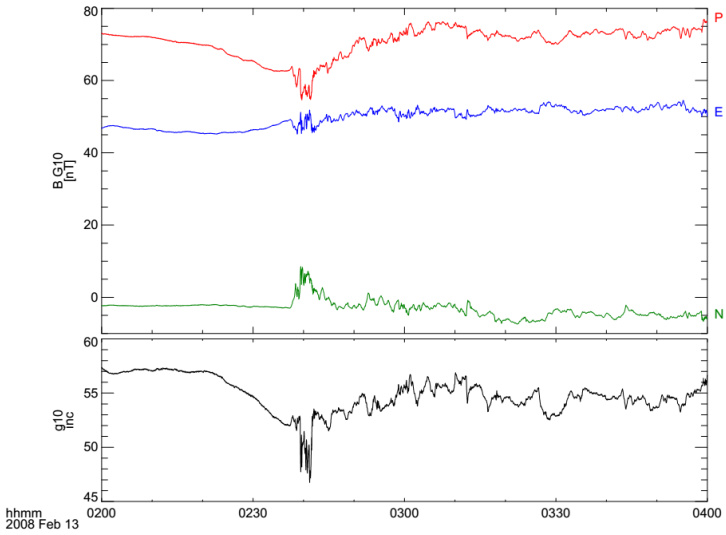

Figure 4.3 Magnetic field observation and the inclination angle obtained by GOES 10 from 0200 UT to 0400 UT in PEN coordinates. Three components Hp, He and Hn are represented by red, blue and green lines. The Hp component is perpendicular to the orbit plane and positive northward. The He component is perpendicular to Hp and Hn and points earthward. Hn component is perpendicular to Hp and He and points eastward. An inclination of 90º means the magnetic field is almost dipolar-like and points northward.

Figure 4.4 displays the locations and strengths of the currents obtained using the inversion model and its validation using geosynchronous observations [*Chu et al.*, 2014a]. In Figure 4.4Figure 2.5a, the strength of the current in the SCW (Iscw) reached a maximum of ~0.3 MA at 02:58 UT during the expansion phase and then slowly decreased during the recovery phase. The strength of the SCW followed the trend of the AL index (Figure 4.2b) throughout this event. The change in the ring current after the substorm onset (Figure 4.4 Irc) is smaller than the SCW. It reached a maximum of 0.07

MA at 02:57 UT. Figure 4.4b illustrates the magnetic local times (MLTs) of the downward and upward FACs of the SCW and the positions of THEMIS P3, P4 and GOES 10 in magnetic local time. The downward FAC was formed around 0400 MLT and hardly moved during the substorm. The upward FAC was first established around 2100 MLT (i.e. -3 MLT in Figure 4.4Figure 2.5) and then expanded westward. It reached 1850 MLT at 03:28 UT, 52 minutes after the onset (not shown). All three probes were located inside the two FACs of the SCW in magnetic local time. This fact indicates that the flows observed by THEMIS P3 and P4 were also located inside the current wedge. In other words, the FACs of the SCW are likely to be consequences of the observed flows. Figure 4.4c shows the comparison between the observed vertical magnetic field at GOES 10 and the prediction using the inversion model. Both the observed and predicted magnetic variations were transformed into solar magnetic coordinates. The onset time, the trend and the amplitude of the magnetic dipolarization are reasonably well predicted by SCW model determined by the inversion technique. Note that the inversion technique takes ONLY ground observations and no input of in situ measurement from spacecraft. The capability of predicting geosynchronous dipolarization using ground data suggests that the inversion model works well in the near-Earth region. The magnetic dip before the permanent dipolarization could be explained by a second current loop of opposite polarity located on a lower L shell than the classic SCW. See discussion section for more details of this possibility.

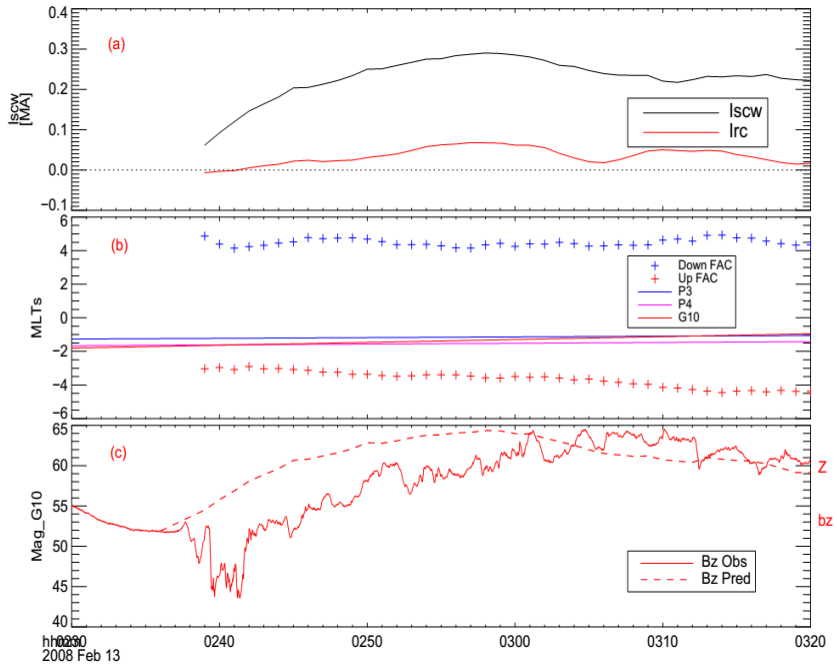

Figure 4.4 Overview of inversion results of the SCW and prediction and observation of Bz at GOES 10. The current strengths of the SCW (black) and the ring current (red) are shown in the first panel. The MLTs of the downward (blue) and upward (red) FACs are shown as asterisks in the second panel. The MLTs of THEMIS P3 (blue), P4 (purple), and GOES 10 (red) are shown as solid lines. The observed Bz at GOES 10 is represented by a red solid line in the last panel. The prediction by the inversion model is plotted as a red dashed line.

Figure 4.5 illustrates the ground auroral observation by THEMIS ASI at the following times: 02:36:00 UT (before the auroral onset), 02:38:00 UT (after the auroral brightening), 02:44:00 UT (auroral expanding poleward) and 02:50:00 UT (the second auroral intensification). The bright patch to the left in each image is the moon. From left

to right the imagers and their magnetic coordinates are GILL (332.78º, 66.18 º), SNKQ (356.99 º, 66.45 º) and KUUJ (13.23 º, 66.89 º). The footprint of the upward FAC is shown as an inverted blue triangle. Before the onset (Figure 4.5a), no auroral activity was observed. Two minutes later (Figure 4.5b), an intensification of the aurora was observed in the field of view (FOV) of KUUJ, which was located around 2220 MLT. The auroral onset was identified at 02:37:12 UT when the aurora suddenly brightened. The upward FAC was near the westward edge of the aurora. After the onset, the auroral brightening expanded both azimuthally and poleward during the expansion phase. This can be seen at KUUJ as westward and poleward extension of bright aurora, and at SNKQ and GILL as intensification of the auroral arc. No auroral streamer or poleward boundary intensification was observed during this event. At 02:44:00 UT (Figure 4.5c), a poleward expansion is evident in the KUUJ image, a westward surge is passing through the SNKQ FOV, and the aurora brightened and extended in the FOV of GILL (most left ASI). The westward travelling surge was more active and located at higher latitude than the auroral arc. The upward FAC was located on the westward travelling surge, which is consistent with the previous study [*Chu et al.*, 2014a]. The aurora expanded to its most poleward location at 02:57 UT and then started to retreat equatorward. Some bright light are present in the bottom of the FOV of KUUJ image from 02:48 UT to 02:58 UT. These lights were not observed in the overlapping FOVs of GBAY or CHBG (to the south of KUUJ), so was most likely caused by localized, transient light contamination such as cars or other sources.

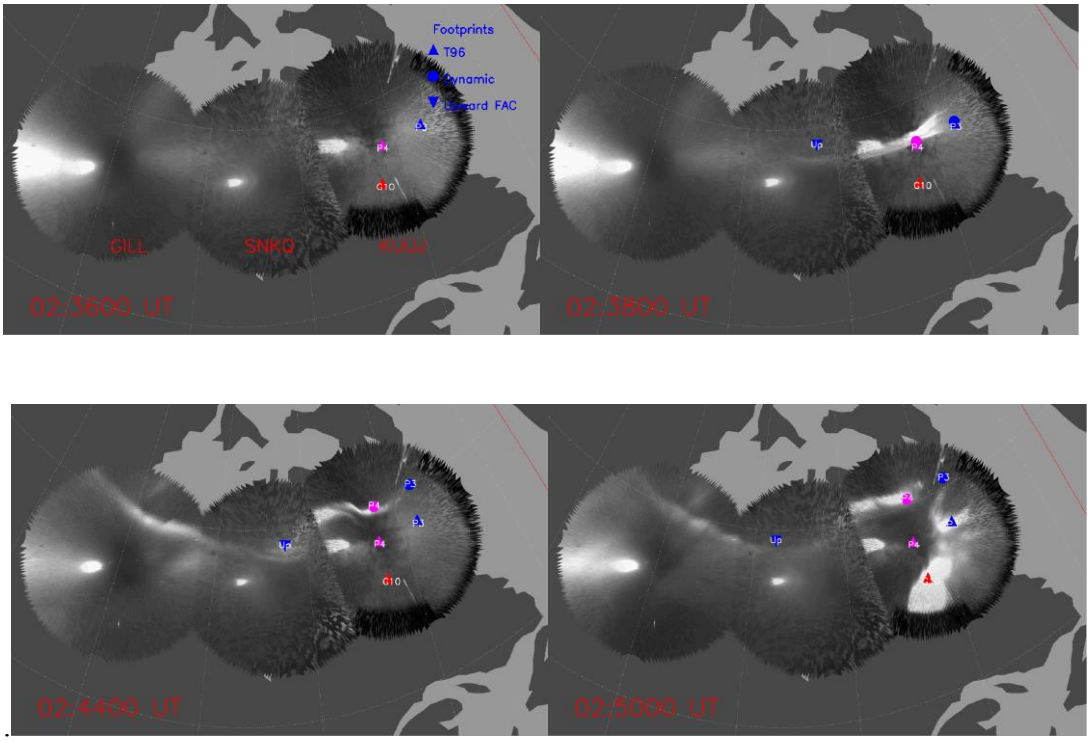

Figure 4.5 Auroral observations from THEMIS ASIs (GILL, SNKQ and KUUJ from left to right) at the following four times: 02:36:00 UT (before auroral onset), 02:38:00 UT (after auroral brightening), 02:44:00 UT (auroral poleward expansion) and 02:50:00 UT (the second auroral intensification). The bright spots in each FOV of the ASIs were moonlight contaminations. The midnight meridian is represented by the red line. The footprints of THEMIS P3 (blue triangle), P4 (purple triangle), and GOES 10 (red triangle) are calculated using T96 model. The revised footprints of P3 and P4 using the dynamic magnetospheric model are represented by circles. The footprint of the upward FAC is shown in blue downward triangle.

Footprints of the three spacecraft (P3, P4 and G10) using the classic T96 model are shown in the FOV of KUUJ in all four images. These were initially located near or below the auroral arc (Figure 4.5a and 5b) and hardly moved in latitude. As the expansion phase progressed their actual latitudes increased due to the change in magnetic field inside the current wedge. Their modified locations predicted by the dynamic magnetospheric model are shown at higher latitude in Figure 4.5c and Figure 4.5d. Since the footprint of P3 was located at the east edge of the auroral brightening, this study focuses more on P4. Immediately after the onset (Figure 4.5b), the revised footprint of P4 were also located on the auroral arc. The revised footprint did not change much because the SCW was still weak. During the expansion phase (Figure 4.5c and 5d), as the SCW grew, the revised footprint moved poleward and were co-located with the aurora. The dynamic magnetospheric model explains the auroral poleward expansion of ~3° with negligible error (much less than half degree).

The temporal changes of the revised footprints are compared with an auroral keogram in Figure 4.6. The top panel shows the current strengths of the SCW and the ring current. The bottom panel displays the auroral keogram of KUUJ during this substorm. The moonlight contamination is removed by fitting a flat-top Gaussian function during quiet times before and after the substorm. The auroral brightening below mlat = 68° from 02:48 UT to 02:58 UT was the light contamination discussed in the last paragraph. The auroral keogram (Figure 4.6b) shows that the aurora first brightened at mlat = ~68° at the onset. It then expanded poleward during the expansion phase, which

followed the trend of the strength of the SCW (Figure 4.6a). The aurora reached the highest magnetic latitude at 02:57 UT which coincides with the maximum of current strength of the SCW. During the recovery phase following this time, the aurora started to move equatorward as the SCW became weaker. Superposed on the general poleward expansion there were three sudden auroral intensifications and short poleward expansions at 02:37 UT (the onset), 02:49 UT, 02:54 UT and 03:07 UT. Those four auroral intensifications and expansions took place at the same times as the flows were observed by P3 and P4 (red arrows in Figure 4.6b).

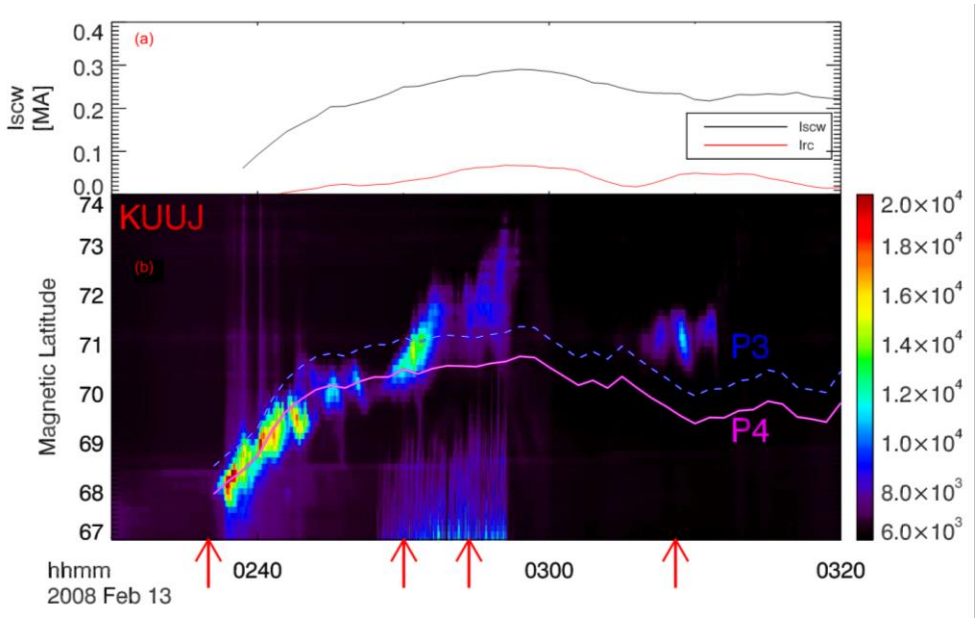

Figure 4.6 Current strengths of the SCW and auroral keogram of KUUJ from 0230 to 0320 UT. The first panel shows the current strengths of the SCW (black) and the ring current (red). The keograms shown in the second panel are integrated in the magnetic latitude bin, and the moonlight contamination is removed by fitting flat-top Gaussian

function during quiet times. The latitudes of the revised footprints of P3 (dashed) and P4 (solid) are shown. The four arrows in the bottom indicate the times when flows were observed by P3 and P4.

The magnetic latitudes of the revised footprints of P4 and P3 are shown as solid lines in Figure 4.6b. At the onset, the footprint of P4 was located at the same latitude as the auroral brightening and in the same meridian as the zenith of the KUUJ ASI. After the onset, the footprint of P4 started to move poleward during the substorm expansion phase. The footprint reached its highest latitude at 02:58 UT at the same time as the strength of the SCW reached its maximum. Then the footprint moved equatorward during the recovery phase as the SCW weakened. The latitude of the footprint of P4 agrees with the auroral intensification very well throughout the substorm. The discrepancy between the footprint and the aurora was less than 1º in latitude. P3 was located to the east of auroral brightening, thus the footprint was located at different latitude (see Figure 4.5).

Figure 4.7 shows the change in the magnetic field lines when the intensity of the SCW reached its maximum at 02:58 UT. The tail part of the SCW was located radially between P4 and GOES 10. It is sheet-like because the tail part was located at different radial distances at different local times. Both P4 and GOES 10 were located ~10 degrees above the magnetic equator. The revised field line from P4, although tailward of the SCW, became dipole-like and bent toward higher latitude than the original one. Thus the footprint of P4 moved to higher latitude. The revised field line from GOES 10, which was earthward of the SCW, was also bent toward higher latitude. Besides, the field line

earthward of the SCW became highly dipolarized near the magnetic equator.

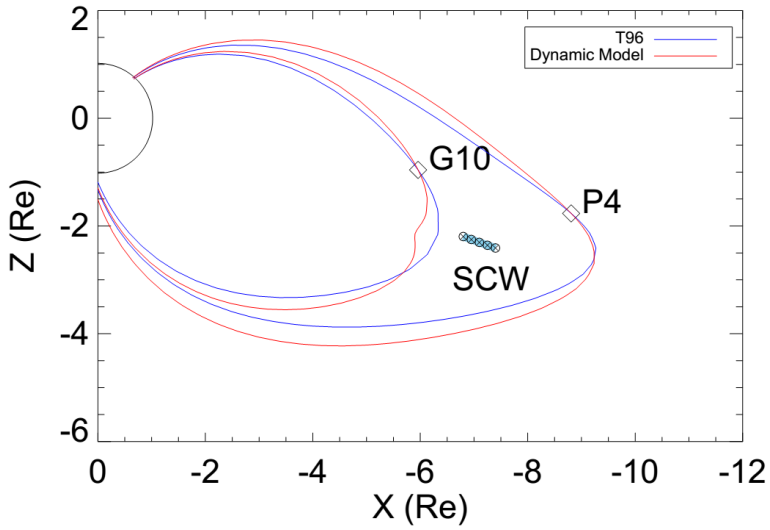

Figure 4.7 Comparison of the revised magnetic field lines (red, from the dynamic magnetospheric model) and the original field lines (blue, from T96 model) from P4 and GOES 10 when the intensity of the SCW reached its maximum at 02:58 UT. The magnetic field lines are projected into the XZ plane. The tail part of the SCW flows into the plane.

4.4 Discussion

In this chapter, I studied the relationship between magnetic field perturbations, auroral expansion, and fast flows observed by THEMIS and GOES 10 spacecraft and ground ASIs during an isolated substorm at 0237 UT on 13 February 2008. Four flows were found to be associated with successive auroral brightenings. When the dynamic

magnetospheric model was used, the revised footprints of the flows and the aurora were colocated with each other not only at the start of the expansion phase but also throughout the substorm.

4.4.1 Onset location and auroral poleward expansion

Understanding the relationship between auroral expansion and onset location in the magnetic equatorial plane is important in addressing the substorm triggering mechanism. Two phenomena, tailward movement of the flux pileup region and dipolarization of the SCW, could contribute to auroral poleward expansion and they are not exclusive. The first is based on the assumption of a static magnetosphere, which is not necessarily true during substorms. During the substorm expansion phase, the magnetic field in the near-Earth region changes from tail-like to dipole-like because of magnetic dipolarization associated with the SCW. This magnetospheric reconfiguration changes flow footprints. Therefore, the dynamic effect of the SCW is non-negligible in studying the mapping from the flows to the aurora and is the subject of this investigation.

During a substorm on 13 February 2008, auroral brightenings observed by ASIs were found to coincide with successive flows observed by P3 and P4. The good correlation between the auroral brightenings and flow breaking and diversion suggested that the flows at |X| = ~9 Re were in the source region of the SCW. During the expansion phase, the aurora expanded poleward from mlat = 68° to almost 74° in 20 minutes. In the static T96 model this expansion corresponds to a tailward retreat of the flux pileup region from |X| = ~9 Re to |X|= ~65 Re, and requires a speed of ~ 300 km s^{-1}, much higher than the

previously observed speed, ~50 km s^{-1} [*Baumjohann et al.*, 1999; *Zhang et al.*, 2011; *Cao et al.*, 2012]. This discrepancy rules out tailward movement of the flux pileup region as the sole cause of auroral poleward expansion. What other mechanisms contribute to auroral poleward expansion?

It can be concluded that auroral poleward expansion was mainly a consequence of magnetic field dipolarization caused by the SCW. In the dynamic model, dipolarization of the SCW was taken into account by adding the SCW and the ring current from the inversion model to the T96 model. Before the onset, the dynamic model is the same as the 96 model because no SCW exists. As shown in Figure 4.5, the footprints from both models overlapped with each other and was co-located with the auroral arc. After the onset, the dynamic model maps the flows to higher latitudes as substorm develops. As the SCW grew stronger during the expansion phase, the magnetosphere inside the current wedge became more dipole-like, and the aurora expanded to higher latitude. During the recovery phase, the footprints map to lower latitudes as the strength of the SCW decreased. The strength of the SCW is an indicator of the dipolarization of the magnetosphere and the locations of the FACs of the SCW determine the region of dipolarization. This is why auroral poleward and equatorward movement have the same trend as the strength of the SCW. As shown in Figure 4.6, the revised footprint of P4 agrees very well with the auroral poleward expansion. Any possible effects of the tailward retreat of the pileup region cannot be examined in this case due to lack of measurements. However, the good agreement between the aurora and revised footprints

suggests that the effect of flow retreat was small in this event. If enough in-situ observations become available, this effect will be examined in the future.

The fact that the auroral motion followed the trend of SCW intensity can be explained in terms of magnetospheric convection. During quiet times, dayside and tail reconnection is approximately balanced, and magnetic flux is transferred toward the dayside by magnetospheric convection. During the substorm expansion phase, earthward flows created by tail reconnection bring in too much flux to be immediately balanced by convection. Magnetic flux piles up and results in dipolarization in the near-Earth region. As more flux accumulates, the magnetosphere becomes more dipole-like, and the aurora moves toward higher latitudes. As the magnetic fields become more twisted by diversion of the accumulated magnetic flux, the substorm current wedge strengthens [*Birn and Hesse*, 2014]. The stronger the SCW, the higher the onset location map in latitude. Note that more than one flow could contribute to flux pileup and thus SCW development. In this event, all four successive fast flows and continuous earthward flows of ~50 km s^{-1} brought magnetic flux into the near-Earth region, resulted in brightening and slight poleward expansion of the aurora, and contributed to the strengthening of the SCW. The first flow was the most important one because it created the largest dipolarization. As more flux is accumulated, the magnetospheric convection is enhanced. The recovery phase begins when the rate of convection exceeds that of flux pileup [*Kissinger et al.*, 2012]. As the flux is transported away by the convection, the magnetic field becomes less dipole-like, and the aurora moves equatorward. During this process the magnetic field

lines becomes less twisted, and the SCW weakens. To sum up, the latitudes of the footprints of the flows and the aurora are closely correlated with the strength of the SCW.

The theory that the SCW is built by accumulating flux is consistent with not only the global SCW but also with narrow current wedgelets surrounding the flows [*Liu et al.*, 2013b; *Sun et al.*, 2013; *Yao et al.*, 2013]. Although the currents surrounding flows do not connect to the ionosphere initially (no magnetic perturbation has been observed in advance of flow arrival), they will contribute to the global SCW as they are stopped in the near-Earth region [*Zhang et al.*, 2011]. Using results from the inversion model, good agreement was found between the intensities of a current wedgelet and cross-tail current reduction for a single flow during a small substorm on 22 March 2010 [*Yao et al.*, 2014] . For substorms with multiple flows, current wedgelets could contribute to the global SCW by accumulating magnetic flux when flows stop in the near-Earth region. This is consistent with the discussion in the previous paragraph.

4.4.2 Mapping using dynamic magnetospheric model

Mapping during active periods has long been problematic in previous models, such as two widely used magnetospheric models: the Tsyganenko models [*Tsyganenko*, 1997] and the event-oriented model [*Pulkkinen et al.*, 1991; *Kubyshkina et al.*, 2011]. The Tsyganenko model, which is rather a steady model, works for an average configuration of the magnetosphere. It usually underestimates tail stretching during the substorm growth phase and overestimates it during the expansion phase. In the event-oriented model, in-situ measurements obtained from spacecraft are used to adjust magnetospheric currents in

the Tsyganenko model. With sufficient in-situ measurements in space and during the substorm growth phase when variations in the tail are slow, the event-oriented model works.

In this chapter, a dynamic magnetospheric model is developed by superposing the dynamic SCW on the T96 model. This new model has several advantages. First, it works for dynamic conditions such as substorms. In case of substorms, Tsyganenko model hardly changes the mapping because the main magnetic perturbations during substorms are created by the SCW. Including the effects of this current is essential to an accurate magnetospheric model and thus mapping during substorms. In previous models, the current wedge was either not included or not updated in real-time. In the dynamic magnetospheric model, the effects of these currents are included and updated every minute using the inversion model (which depends on temporal resolution of the input data). Therefore, the new magnetospheric model better represents substorm dynamics. The new magnetospheric model is expected to work during storms because the ring current was included in the model. This will be investigated in future work. Second, the revised model is not restricted by the availability of in-situ measurements in space. Third, the parameters of the SCW could be obtained through a long history. The parameters of the currents are easy to obtain using the inversion model for SCW, which takes ground magnetic field data at midlatitudes as input. Fortunately there is a long history and large database of such data. Fourth, the magnetic effects of geomagnetically-induced currents (GICs) contributes to the mapping technique. The conducting surface of the Earth

responds to the magnetic variations of the ionospheric and magnetospheric currents. Geomagnetically-induced currents are currents under the Earth's surface. The GICs generally increases the horizontal magnetic perturbation (H and D component) and reduces the vertical variation (Z component) on Earth's surface. Therefore, they cause more northward twisting of the magnetic field lines inside the SCW. In other words, without the induced currents, the magnetospheric reconfiguration would be underestimated closer to the ground and the accuracy of mapping would be reduced.

The changes in the magnetic field due to the SCW is represented by the dynamic model to a good approximation. Ideally, the FACs of the SCW should exactly follow the revised field lines from the dynamic model instead of the original ones. This could be achieved by forcing the currents to flow along the revised field lines until the angles between the FACs and the revised field lines are negligible in successively iterations. However, the magnetic perturbations are more sensitive to the strength and location of the SCW rather than the change in the shape of the FACs. The azimuthal or latitudinal locations of the SCW mainly determine the region of the dipolarization. Besides, Figure 4.7 shows that the original and the revised field lines were very close and that the differences between their magnetic perturbations were negligible in the near-Earth region. At latitude higher than 5 degrees from the magnetic equator, the angles between the revised field lines and the original ones has a mean value lower than 2 degrees, which is very small and does not change the dipolarization significantly. P4 was located 10 degrees higher than the magnetic equator, therefore mapping P4 to the northern

hemisphere is fairly accurate because the revised field line did not pass the magnetic equator. Besides, as shown in Figure 4.7, the field line from P4 near the equator was not bent much because it was not earthward of the SCW. Therefore, to save computation time, the FACs were not forced to follow the revised magnetic field lines in the current model. Its effect on mapping will be examined in future work (such as from GOES 10 where the magnetic field is highly dipolarized).

4.4.3 Dipolarization and two-loop SCW model

Geosynchronous dipolarization has been observed in regions radially inside and azimuthally between two field-aligned currents (FACs) of the SCW [*McPherron et al.*, 1973]. As the SCW strengthens and expands azimuthally during the expansion phase, dipolarization is observed with a time delay at locations farther away from the center of the SCW [*Nagai*, 1982b]. For the event studied in this chapter on 13 February 2008, geosynchronous dipolarization was observed by GOES 10 which was located inside the SCW. The magnetic dipolarization was predicted using the SCW inversion model. As shown in Figure 4.4c, the amplitude and the trend of the predicted dipolarization agrees very well with the observations at GOES 10.

The ability to predict dipolarization suggests that, to a good approximation, the classic one-loop SCW is able to represent large-scale magnetic perturbations in the near-Earth region. In other words, the classic SCW works well to improve mapping. However, it should be noted that a transient magnetic dip was observed at GOES 10 at ~02:38 UT, before the permanent dipolarization, which suggests the existence of a thin current layer

in front of the broad region of permanent dipolarization. This is consistent with the two-loop SCW model in which an additional current loop of opposite polarity exists at lower latitude underneath the classic SCW [*Obayashi and Nishida*, 1968; *Ritter and Lühr*, 2008; *Yang et al.*, 2010; *Sergeev et al.*, 2011; *Birn and Hesse*, 2013]. They found that the inner current loop was probably located around geosynchronous orbit, and the outer current loop near X = -11 Re. The magnetic dip at GOES 10 could be explained by the combined effect of the inner and outer FAC loops. This thin current layer is likely produced by reflected ions ahead of the flows [*Zhou et al.*, 2014b]. This might be true even at low velocities, and those ions would be several hundred kilometers ahead of the flow front given that their gyroradius was similar to the distance between P4 and GOES 10. Therefore, although fast flows did not likely penetrate into geosynchronous orbit [*McPherron et al.*, 2011; *Hsu et al.*, 2012], there were still ion injections near geosynchronous orbit accompanied by a peak of 30 km s^{-1} in Vx around onset [*Gabrielse et al.*, 2014]. The inner current layer is much more transient and localized than the outer one. This conclusion is consistent with recent result by *Murphy et al.* [2013]. He found that although the detailed structure of the SCW is significantly more complex than the equivalent line current model, the overall longitudinal structure of the net FACs (averaged over latitude) resembles the simpler equivalent line current of SCW. [*Connors et al.*, 2014] found that SCW development from AMPERE consistent with inversion result using ground measurement. Their results are also consistent with my result that, by introducing classic SCW into the magnetosphere model, the permanent dipolarization at GOES 10 was well predicted and the auroral poleward motion was explained. These

results also suggest that the localized inner current loop has little effect on auroral poleward motions.

4.5 Summary

In the study of an isolated substorm on 13 February 2008, a good correlation was found between four auroral brightenings and four flow breakings and diversions observed by THEMIS P3 and P4, suggesting that the onset location was near |X| = ~ 9 Re. The inversion model for SCW was applied to this event to obtain the strengths and locations of the currents (SCW and ring current) every minute. The results were validated by comparing the observed and predicted geosynchronous dipolarization at GOES 10. By superimposing the magnetic fields of currents in the inversion model on those of T96 model, a dynamic magnetospheric model was developed. It was found that:

1. Successive flow breakings and diversions in the near-Earth magnetotail contributed tos the generation of auroral brightenings, slight auroral poleward expansions, and the global SCW.

2. Geosynchronous permanent dipolarization (lasting longer than tens of minutes) was well predicted by the inversion model for SCW, suggesting that the overall longitudinal structure of the net FACs averaged over latitude resembles the classic SCW.

3. The footprints of the flows calculated using the dynamic magnetospheric model were

colocated with auroral brightenings. The footprints followed the auroral poleward expansion during the expansion phase and equatorward retreat during the recovery phase.

4. The evidence above suggests that the auroral poleward expansion and equatorward retreat in this substorm event were mainly caused by the magnetic dipolarization of the global SCW. Although minimal in this event, the effect of the tailward expanding flux pileup region could not be excluded.

Chapter 5

Is the pressure gradient a driver of the substorm current wedge? A statistical study

Substorm current wedge (SCW) formation is believed to be related to the flow braking and diversion process. In this chapter, good temporal and spatial correlations are found between earthward flows during five THEMIS tail seasons and substorm onsets identified using the midlatitude positive bay index. Flow occurrence is found to peak at substorm onset. More than half the flows observed within one hour of substorm onsets occur within ten minutes of onsets. In addition, Most of these flows (85%) are found inside an SCW between its upward and downward field-aligned currents (FACs). It has been suggested that these FACs are generated either by flow vortices, pressure gradient, or both. It is shown here that the flow speed (related to the flow vortices) decays quickly within several minutes. On the other hand, the equatorial thermal pressure (related to the pressure gradient) increases and persists for about an hour, and has a trend similar to that for the westward electrojet and FACs of the SCW. Therefore, the SCW is likely sustained by the pressure gradient rather than short-lived flow vortices. The pressure gradient, calculated when three THEMIS probes were distributed in a triangular configuration in the equatorial plane, was found to be well organized relative to the central meridian (CM) of the SCW. The component ∇P_x increases for all substorms; while ∇P_y increases in magnitude and points toward the center of the current wedge. The non-alignment of ∇P and ∇V should generate an SCW with a quadrupole FAC pattern, similar to that seen in

global MHD and RCM-E simulations. In these simulations the inner current loop is weaker than the outer loop so that the magnetic effect at geosynchronous orbit and on the ground is that of the outer loop diminished in strength by the inner loop, which resembles a classic SCW.

5.1 Introduction

The substorm current wedge (SCW) is a central feature of the expansion and recovery phases of a magnetospheric substorm. It consists of a reduction of the cross-tail current in the tail, field-aligned currents (FACs) connecting the magnetotail to the ionosphere, and a westward electrojet in the ionosphere. An SCW is believed to be generated by flow braking in the near-Earth region [*Haerendel*, 1992b; *Shiokawa et al.*, 1997; *Shiokawa et al.*, 1998a; *Shiokawa et al.*, 1998b]. Although earthward flows are known to be associated with substorms [*Hones et al.*, 1973; *Hones*, 1977], they can occur at any level of magnetic activity [*Angelopoulos et al.*, 1994]. Because flows are more common than substorms, there is no one-to-one correspondence between them [*McPherron et al.*, 2011]. Furthermore, the speed of earthward flow drops significantly inside 12 R_E [*McPherron et al.*, 2011], which is believed to be the flow braking region in which SCWs are generated. Therefore, it is reasonable to expect earthward flows in the flow braking region to be well correlated with SCW formation. Such temporal and spatial correlations of these flows with the substorm current wedge are investigated in this chapter.

Substorm current wedge formation has been studied using theory, simulations and observations [*Birn et al.*, 1999; *Keiling et al.*, 2009; *Xing et al.*, 2010; *Yao et al.*, 2012; *Birn and Hesse*, 2014]. Theory suggests that FACs in an SCW are generated by an inertial current, flow vortices, and pressure gradient [*Vasyliunas*, 1970]. The inertial current is usually neglected because it is considerably weaker than the current created by flow vortices and pressure gradient [*Haerendel*, 1992b; *Shiokawa et al.*, 1997; *Shiokawa et al.*, 1998a; *Shiokawa et al.*, 1998b; *Birn et al.*, 1999]. On the other hand, event studies show that flow vortices and pressure gradient can generate FACs strong enough to support a typical SCW [*Keiling et al.*, 2009; *Xing et al.*, 2010; *Yao et al.*, 2012]. Global MHD simulations suggest that a depleted plasma bubble with thermal pressure lower than the ambient plasma flowing earthward can set up flow vortices and azimuthal pressure gradient pointing away from the flow, generating a quadrupole distribution of FACs [*Birn and Hesse*, 1991; 2014]. A quadrupole SCW has an outer current loop the same as pictured in the classic SCW (usually referred as a region-1-sense current), and a weaker inner current loops flowing in the opposite direction at the same local time (referred as a region-2-sense current). The magnetic effect of the inner current loop partially cancels the effect of the outer loop on the ground and at geosynchronous orbit. Thus their combined magnetic effect is equivalent to a classic SCW with current corresponding to the difference current. Therefore, as suggested by simulations, the pressure gradient and flow vortices are expected to be organized relative to the central meridian of the current wedge. Obtaining the pattern of pressure gradients and flow vortices requires the knowledge of FAC locations since the current wedge can occur at any local time in the

night sector. The FAC locations are unknown from in situ observations, because FACs are weak and spread over large regions relative to the satellite coverage. Furthermore, in situ observations are sometimes transient and localized and not necessarily related to a global SCW. In this chapter, the FAC locations were obtained from a recently developed inversion technique for SCW using ground magnetometer data based on the positive bay signature at midlatitudes [*Chu et al.*, 2014b]. The pattern of the pressure gradients and flow vortices will be examined relative to the central meridian of the SCW (in the SCW frame).

The database of the flows and substorm onset will be described in section 2. Observations are presented in section 3 and discussion in section 4.

5.2 Data and model

Auroral electrojet indices (AE, AU and AL) are obtained from the World Data Center for Geomagnetism in Kyoto at 1 minute resolution. The midlatitude positive bay (MPB) index, which measures the strength of the FACs in the SCW, is calculated using magnetometer data at midlatitudes obtained from InterMagnet and SuperMAG at 1 minute resolution [*Chu et al.,* 2015b]. The substorm onset list is obtained by processing the MPB index and using the original magnetometer data [*Chu et al.*, 2015b]. The time of maximum current wedge development and the end of the substorm as seen at midlatitudes are also identified. This onset list is designed to detect only major onsets because it is insensitive to pseudo breakups and localized intensifications. The strengths and locations of the FACs in the current wedge are obtained every minute using the

inversion technique for SCW using ground magnetometer data at midlatitudes [*Chu et al.*, 2014b].

Flow events are determined from the identically-instrumented Time History of Events and Macroscale Interactions during Substorms (THEMIS) probes (P1-P5) during five tail seasons from 2008 to 2012 [*Angelopoulos*, 2008]. The apogees of the five probes are 30 R_E for P1, 20 R_E for P2, and 10-12 R_E for P3, P4 and P5. The flux gate magnetometer (FGM) [*Auster et al.*, 2008] provides three second spin averaged magnetic field. The electrostatic analyzer (ESA) [*McFadden et al.*, 2008] obtains ion and electron measurements in the 5 eV to 25 eV energy range and have been processed to remove background (penetrating) electrons and an accurate subtraction of the effect of spacecraft potential. The solid state telescope (SST) obtains ion and electron fluxes in the 25 keV to 1 MeV range. I have removed the sun-contamination, applied detector calibration, and obtained accurate partial moments for energetic particles [*Angelopoulos*, 2008]. The plasma moments (density, velocity, and temperature) have been calculated from a combination of the measurements of both ESA and SST instruments.

Using THEMIS observations, a list of earthward flows is created for P3, P4 and P5 (whose apogees are near 12 R_E). Only observations in the magnetotail region $\sqrt{Y^2+Z^2} < 12R_E$, X<0 R_E and $\sqrt{X^2+Y^2+Z^2} > 6R_E$ are considered. Observations are restricted to the plasma sheet by requiring plasma beta (β), the ratio of thermal pressure to magnetic pressure, be greater than 0.5. The plasma velocities are separated into parallel ($V_{\parallel}$) and perpendicular velocities ($V_{\perp}$) based on the magnetic field. Fast earthward flows are defined as $V_x \geq 0$ km/s and $V_{xy} \geq$ 150 km/s, where V_{xy} is the

speed in the GSM equatorial plane. Flow onsets are defined when V_{xy} exceeds 100 km/s, and the end is defined when V_{xy} is lower than 100 km/s. Another list of earthward flows is created for THEMIS P2, whose apogee is about 20 R_E, during the first two tail seasons in 2008 and 2009 using the same criteria. Unless otherwise specified, the earthward flows in this chapter are those observed by THEMIS P3, P4 and P5 earthward of 12 R_E.

5.3 Observations

5.3.1 Substorm example

An isolated substorm was observed by THEMIS probes P3, P4, and P5 between 0120 UT and 0200 UT on 07 February 2008. Figure 5.1 is an overview of the observations. The MPB and AL indices, which measure the FACs and the westward electrojet of the SCW respectively, started to change sharply at around 01:28 UT. The MPB index reached its maximum at 01:43 UT and the AL index was close to its extreme value during the same time period. The two indices showed that the SCW lasted for half 30 minutes. The locations of the upward and downward FACs in the SCW, obtained from the inversion technique for SCW, are shown in magnetic local time (MLT). The downward FAC was centered at 0300 MLT, and the upward FAC at around 1900 MLT. The central meridian of the SCW was located at one hour premidnight. The downward FAC expanded eastward after onset, as did the central meridian. THEMIS probes were located at 2300 MLT at the onset as shown by the thin nearly horizontal lines. They were co-located with the central meridian at the onset, and became duskward of it after the onset.

Plasma beta at the three probes was larger than one, suggesting that they were located in the plasma sheet. Earthward flows of ~1000 km/s were observed by three probes at the onset, which lasted for less than 2 minutes. The flows were observed at the central meridian and inside the SCW between two FACs. No other flow bursts were observed during the remainder of the substorm. The equatorial thermal pressure was calculated using $P_{eq} = P_{th} + \frac{(B_x^2+B_y^2)}{2\mu_0}$ assuming that B_Z was relatively constant near the current sheet [*Xing et al.*, 2009; *Xing et al.*, 2011]. The equatorial thermal pressure started to increase after the flows (next to bottom panel). Because three probes were very close (within 2 R_E) and in a triangular configuration on the equatorial plane, the pressure gradient ∇P can be calculated assuming pressure changes linearly with distance in the equatorial plane. The calculated pressure gradient ∇P at the three probes are plotted in the bottom panel. Before the onset, ∇P_x was positive and ∇P_y was around zero, suggesting that the thermal pressure increased radially earthward. When the flows were observed, the equatorial pressure started to increase and a transient change in pressure gradient was observed. The component ∇P_x increased while ∇P_y decreased sharply, suggesting that the thermal pressure was higher earthward and toward the central meridian. When the flows disappeared, the pressure gradient dropped quickly to almost background value. During the substorm, the equatorial thermal pressure increased and a prolonged change in pressure gradient was observed. The component ∇P_x increased and ∇P_y decreased relative to background values during the remainder of the substorm. Although the pressure gradient during the substorm was smaller than that during flows, it

lasted longer and had the same trend as the AL index.

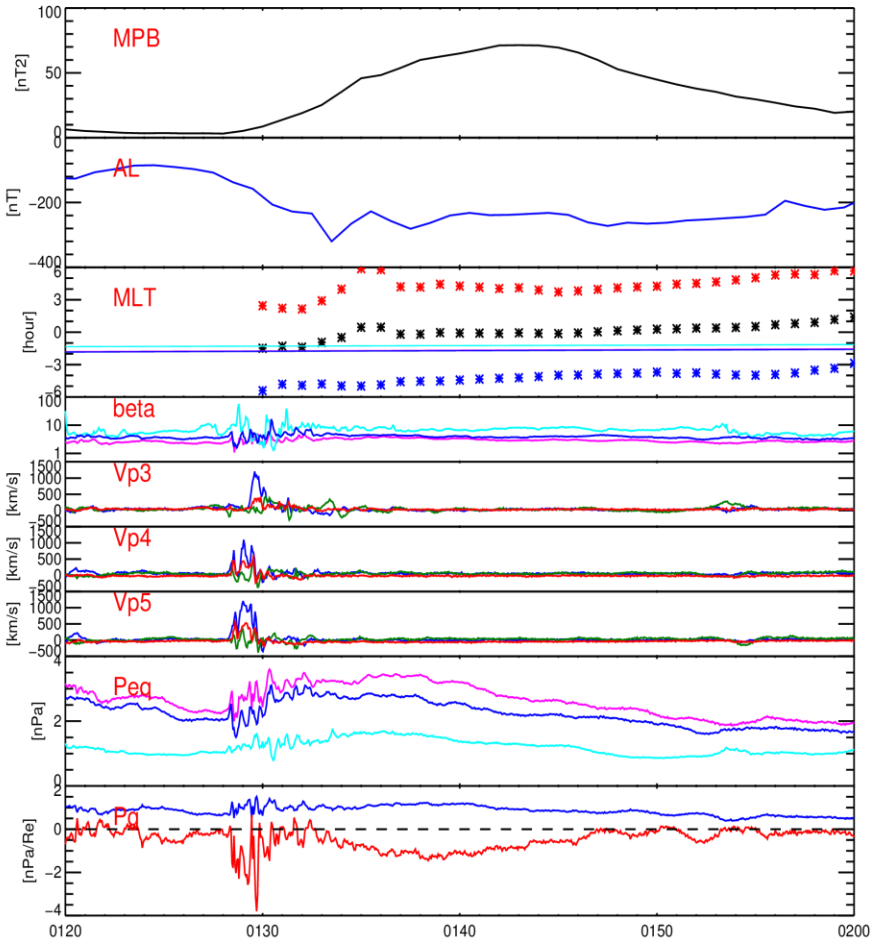

Figure 5.1 An overview of observations for an isolated substorm on February 07 2008 is presented. The MPB and AL indices are shown in the first two panels. The locations of the upward (blue) and downward (red) FACs and their central meridian (black) are shown in MLT (asterisks in the third panel). The MLT of THEMIS P3 (light blue), P4 (blue), and P5 (purple) are shown as solid lines. The plasma beta at THEMIS probes is shown in the fourth panel. The flow velocity at THEMIS probes is shown in the

following three panels. The equatorial thermal pressures observed at three probes is shown in the next panel. The pressure gradients ∇P_x (blue) and ∇P_y (red) are shown in the last panel.

5.3.2 Temporal correlation between flows and substorms

Figure 5.2a shows the time delay analysis between flow onset and substorm onset with a time window of ± 1 hour. All flows observed within 12 R_E were used because it is believed to be the flow braking region. In the time delay analysis, the MPB substorm onset was set to epoch zero. Thus, positive (negative) time delay means that flows were observed after (before) the substorm onset. A total of 703 flows was observed within 1 hour of substorm onset. A sharp peak was found at epoch zero in the time delay distribution. More than half of these flows (356) were found within 10 minutes of substorm onsets, which are referred to as 'onset-associated flows'. The good temporal correlation suggests that most flows were observed simultaneously with substorm onsets.

Flow occurrence during different substorm phases is also investigated in Figure 5.2b. Because the substorm durations vary between events, they were normalized to 1 and divided into ten bins. Substorm duration is defined as the time interval between substorm onset and the end of substorm [*Chu et al.,* 2015b]. The mean value of the substorm durations was 46 minutes. A total of 1299 flows were found from -1 to 2 substorm durations. The flow occurrence normalized by substorm duration also peaked at substorm onset. At other times, the flow occurrence was much lower, but not zero. Furthermore, the flow occurrence was slightly higher before the substorm onset (during the substorm

growth phase) than after the substorm onset.

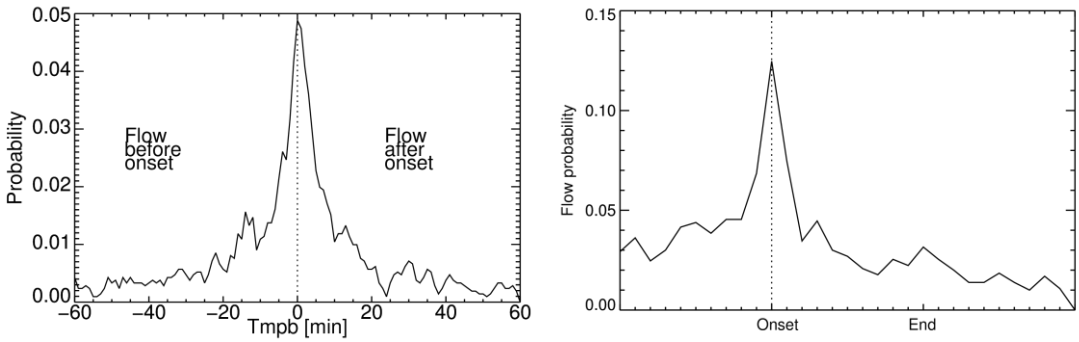

Figure 5.2. (a) Time delay analysis between the earthward flows observed by THEMIS P3, P4, and P5 within 12 R_E and substorm onsets identified using the MPB index. The substorm onsets have been set to epoch zero. Positive (negative) delay means that flows were observed after (before) the substorm onsets. (b) The probability of flows normalized by substorm duration.

5.3.3 Spatial correlation between flows and SCWs

As shown in Figure 5.1, the onset-associated earthward flows were located inside the SCW between the two FACs. A statistical analysis was carried out to study the spatial correlation between the earthward flows and the FACs. To ensure that the locations of the FACs were available, only onset-associated flows were selected (flows that occurred within 10 minutes of substorm onset; see section 3.2). Then the locations of the FACs were determined using the inversion technique for SCW. Since the widths of the SCWs between two FACs vary among different substorms, the locations of two FACs were normalized by the width of the SCW. Thus, the location of the upward (downward) FACs was set to zero (one). Figure 5.3 shows the probability of the flows' locations relative to

the FACs. The occurrence distribution peaked inside the SCW between two FACs. Among 589 onset-associated flows, more than 85% (501) were found inside an SCW. Moreover, the occurrence distribution was asymmetric, skewed toward the upward FAC. Note that an SCW is also asymmetric as the two FACs have different widths. The upward FAC is narrow and the downward FAC is wider as indicated by horizontal bars at the top of the plot. The spatial correlation between the flows and the FACs suggests that these flows generate upward FAC on the duskside and downward FAC on the dawnside.

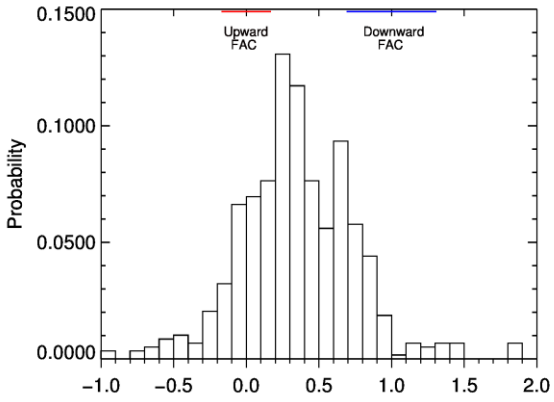

Figure 5.3. The probability distribution of flow locations associated with substorm onset as a function of FAC locations in the SCW. The FACs' locations have been normalized so that the location of the upward (downward) FAC is zero (one). The FAC widths are indicated by horizontal bars at the top. More than 85% of the flows are located between the upward and the downward FACs.

5.3.4 Pressure and flows

To investigate the contribution of flow vortices and pressure gradient to FAC generation, superposed epoch analysis (SPEA) of the flow velocity and the equatorial

thermal pressure was performed. Figure 5.3 shows the SPEA of the MPB and AL indices, flow velocity, magnetic field B_Z, and equatorial thermal pressure relative to onset-associated flows within 12 R_E. Both the MPB and AL indices started to change sharply after the substorm onset, suggesting that the FACs and the westward electrojet of the SCW strengthened. These currents reached a maximum in about 20 minutes and then gradually recovered. The currents in the SCW persisted for about an hour. The equatorial thermal pressure increased sharply after epoch zero and slowly decayed within about an hour. The magnetic field B_Z rapidly increased after the onset, reaching a maximum in about 20 minutes and then decreasing slowly in the next hour. This is magnetic dipolarization associated with the SCW formation. The trends of the equatorial thermal pressure and the magnetic dipolarization are similar to that of the currents in the SCW. The flow velocity, however, had a sharp peak at epoch zero which lasted for less than 3 minutes and quickly decayed. Although the flow occurrence was non-zero after the onset as shown in Figure 5.2, the SPEA of the flow velocity was washed out by time periods when no flow was present. It should be noted that the equatorial thermal pressure reached its maximum much quicker than the dipolarization of B_Z.

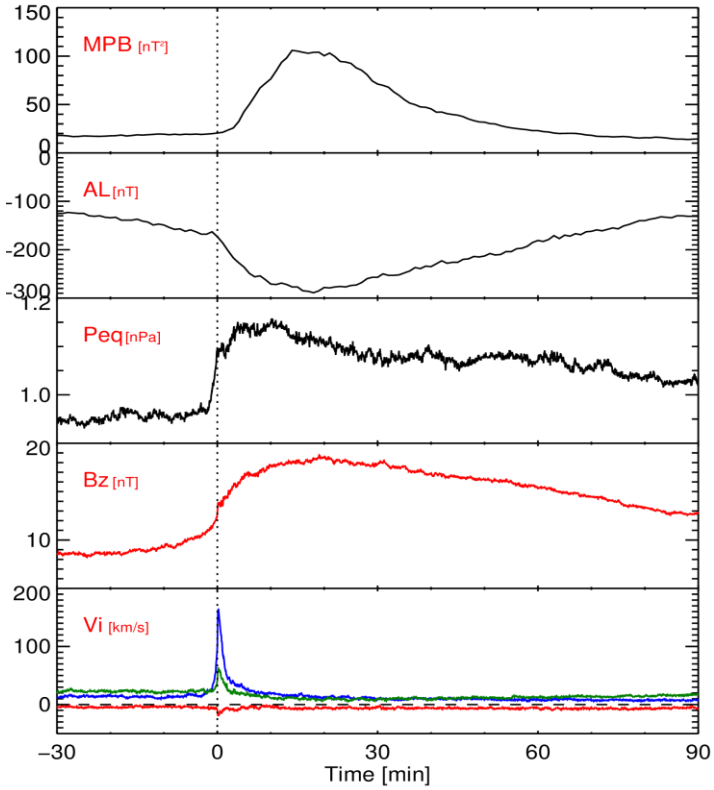

Figure 5.4. Superposed epoch analysis of the MPB and AL indices, the equatorial thermal pressure, the magnetic field B_Z, and the flow velocity relative to onset-associated flows within 12 R_E.

Figure 5.5 shows the SPEA of the equatorial thermal pressure, plasma pressure, density, temperature, and magnetic field B_Z relative to flows observed by THEMIS P2 tailward of -12 R_E (from -12 to -20 R_E). Note that the equatorial thermal pressure was almost constant after the flows. Although the plasma density decreased in the plasma bubble, the temperature increased significantly. Therefore, the thermal pressure increased after the flow onset. The magnetic field B_Z had a spike at the flow onset, which was the signature of a dipolarization front [*Runov et al.*, 2009; *Liu et al.*, 2014]. The B_Z reached a

maximum in about 10 minutes and then slowly decreased. The percentage of change in B_Z was larger than the change in the equatorial thermal pressure. Therefore, in regions tailward of 12 R_E, the magnetic dipolarization was clear while the equatorial thermal pressure kept constant.

The results above suggest that as flows travel earthward, plasma temperature and equatorial thermal pressure increase, with the majority of the heating in the near-Earth region. The flow velocity, on the other hand, did not last long enough to sustain an SCW. Therefore, the gradient of the increased pressure is more likely sustaining the FACs of the SCW.

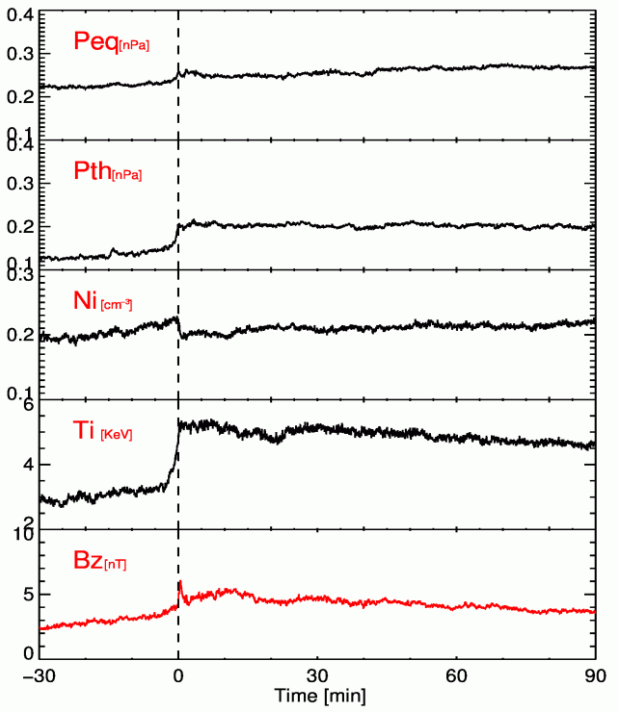

Figure 5.5. Superposed epoch analysis of the equatorial thermal pressure, the thermal pressure, plasma density, thermal temperature, and the magnetic field B_Z relative to the flows observed between 12 and 20 R_E.

5.3.5 Pressure gradient in SCW frame

In this section, the distribution of the pressure gradient in the SCW frame is investigated. To obtain the pressure gradient, three THEMIS probes (P3, P4, and P5) are required to be located in a triangular configuration near the equatorial plane and close to each other (within 2 R_E). During five tail seasons, 42 time intervals with a total of 253 hours of data satisfy these criteria. Most occurred in 2008 because the THEMIS probes were separated in the z direction in later years. In these time intervals, 23 isolated substorms including the substorm example in Figure 5.1, were found. For each event, the central meridian of the SCW was obtained using the inversion technique for SCW. The change in the pressure gradient ∇P was obtained by subtracting the initial value at the onset. Figure 5.6 shows the changes in ∇P_x and ∇P_y as a function of local time relative to the CM of the SCW. The $\delta\nabla P_x$, pointing toward the Earth, increased during most of the substorms, suggesting that the equatorial pressure increased closer to the Earth. The $\delta\nabla P_y$, pointing duskward, increased on the dawnside of the central meridian, and decreased on the duskside. It suggests that the maximum of the equatorial thermal pressure was co-located with the central meridian of the SCW. This is consistent with the result in Figure 5.3 that the flows were located inside the SCW between two FACs. These results indicate that the high pressure region created in the flow braking process was co-located with the central meridian of the SCW. And the downward FACs were generated on its dawnside and the upward FACs on its duskside.

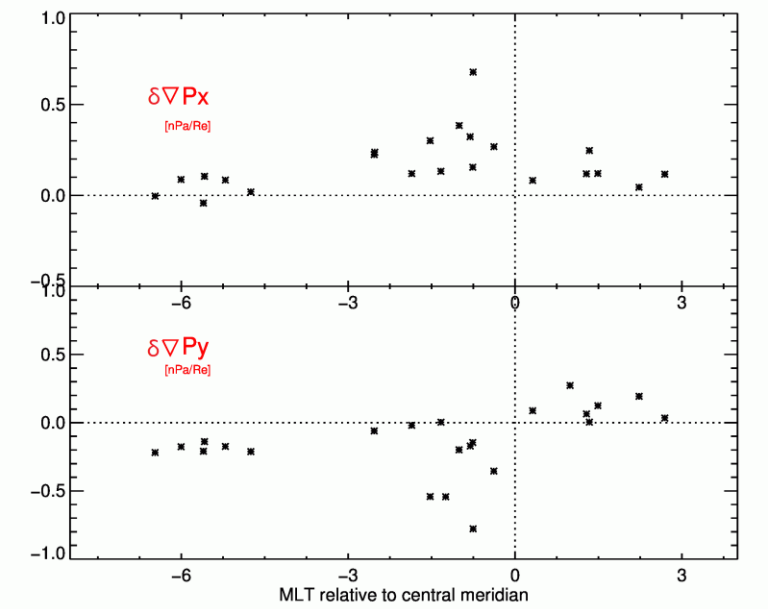

Figure 5.6. The changes in the components of the pressure gradients $\delta\nabla P_x$ and $\delta\nabla P_y$ during substorms as a function of local time relative to the central meridian of the SCW are shown.

5.4 Summary and Discussion

Substorm current wedge formation is usually attributed to pressure gradient and flow vortices created in flow braking and diversion process. Therefore, pressure gradient and flow vortices are expected to be organized relative to the central meridian of the SCW, but it cannot be obtained from in-situ observations in space. The central median of the SCW was obtained with the inversion technique, and the generation mechanisms of the FACs were investigated statistically in the SCW frame. In this section, we will discuss how these results shed light on the generation mechanisms of the SCW.

5.4.1 Flow occurrence relative to substorm onset

Although earthward flows are known to be associated with substorms, they can occur at any level of magnetic activity, so there is no one-to-one correspondence between them. Since the SCW is believed to be generated in the flow braking region inside 12 R_E, the temporal correlation between the earthward flows inside 12 R_E and substorm onsets identified using the MPB index was investigated. Figure 5.2a shows the time delay analysis between the flows and substorms with a one hour time window. The flow occurrence peaks at substorm onset and more than half of the flows were observed within 10 min of substorm onset. A similar good temporal correlation was found between earthward flows and substorm onsets identified using the AL index (which measures the westward electrojet) [*McPherron et al.*, 2011]. The flow occurrence normalized by substorm duration in Figure 5.2b also peaks at substorm onset. These results support the idea that SCW formation is associated with flow braking. It should be noted that the flow occurrence is non-zero all the time, consistent with the fact that flows can occur at any level of magnetic activity and with recent studies showing that only a small fraction of fast flows can trigger a substorm [*Ohtani et al.*, 2006; *Takada et al.*, 2006; *Weygand et al.*, 2008]. The penetration depth of an earthward flow is generally thought to depend on its entropy, rather than its initial flow velocity [*Dubyagin et al.*, 2011; *Sergeev et al.*, 2014a]. The flow has an entropy lower than the ambient plasma when it is created by magnetic reconnection [*Pontius and Wolf*, 1990]. The flow is expected to move earthward adiabatically, conserving its lower entropy, and reaches a location where the background

plasma entropy equals that of the flow. It should also be noted that the flow occurrence is higher before the substorm onset during growth phase and lower during the expansion phase. The occurrence of ground Pi 2 pulsations, associated with fast flows, was also higher during substorm growth phase [*McPherron*, 1994]. The reason is that the magnetic field lines become highly dipolarized during the expansion phase, which makes it more difficult for later flows to penetrate into the near-Earth region. In other words, the background entropy decreases when the magnetic field lines become dipolarized, and thus the flows stop at locations farther from Earth.

5.4.2 Flow location in the SCW frame

The statistical results show not only good temporal correlation between the flows and the SCW, but also a good spatial correlation. As suggested by simulations, the pressure gradient and the FACs are expected to be organized by the local time of the flows. Although the occurrence distribution of the flows centers at 2300 MLT, the flows can come from any local time in the night region [*McPherron et al.*, 2011]. In addition, the central meridian of the SCW also centers at 2300 MLT, but it can be anywhere in the nightside. Therefore, the spatial correlation between the flows and the SCWs has been investigated statistically for the first time. As shown in Figure 5.3, more than 85% of the onset-associated flows were located inside the SCW between two FACs, suggesting that FACs are usually located on both sides of the flow. In other words, earthward flows generate FACs of different polarities on each side. This is consistent with numerical MHD simulations of current wedge formation, in which the pressure gradient and the

flow vortices have different polarity on each side of the flows, generating FACs of different polarity.

In addition, the flow distribution in Figure 5.3 is asymmetric, skewed toward the duskside of the flow. The FACs in an SCW are also known to be asymmetric, with a narrow upward FACs and wider downward FACs. The skewness of the flow distribution is likely due to the asymmetry of the FACs. One possible reason is that ion acceleration is more effective on the duskside of the flows, and the plasma is heated more on the duskside [*Zhou et al.*, 2014a; *Zhou et al.*, 2014b]. The asymmetry in plasma heating might produce asymmetric pressure increase, and thus asymmetric pressure gradient generating asymmetric FACs. The asymmetric pressure distribution is also evident in Figure 5.6, in which both ∇P_x and ∇P_y are stronger on the duskside in the SCW frame, resulting FACs with stronger current density on the duskside.

5.4.3 Substorm Current Wedge Generation Mechanisms

Because the SCW formation is usually attributed to pressure gradient and flow vortices caused by flow braking, their contributions to FACs are investigated. As shown in Figure 5.4, FACs and westward electrojet in the SCW increased sharply after the onset and lasted for about an hour. The equatorial thermal pressure also increased after the onset, and had a temporal trend similar to the strength of the SCW. The flows, however, lasted for less than 3 minutes, significantly shorter than the SCW measured by the MPB and AL indices. Therefore, the pressure gradient is likely sustaining the FACs in the SCW rather the flow vortices. In an event study, it was shown that a flow vortex with a

final speed of 500 km/s and a radius of 1 R_E can generate enough FACs for an SCW [*Keiling et al.*, 2009]. In another event study, it was found that the total FACs from the flow vortices and the azimuthal pressure gradient are comparable to a typical SCW [*Yao et al.*, 2012]. The flow vortices lasted less than 5 minutes in both studies. Therefore, although flow vortices and azimuthal pressure gradient could generate FACs with strong current density, the pressure gradient is the dominant contributor to the FACs in an SCW because the flow vortices disappeared quickly.

The equatorial thermal pressure within 12 R_E increased by about 20% as shown in Figure 5.4. The equatorial thermal pressure changed slightly in the mid tail from 10 to 20 R_E, although the thermal pressure increased. In any case, the equatorial thermal pressure did not drop inside the flow, suggesting a picture slightly different from simulations in which the thermal pressure decreased inside the flow [*Yang et al.*, 2011; *Birn and Hesse*, 2013]. Note that this does not contradict previous statistical studies showing that thermal pressure decreases after a dipolarization front [*Runov et al.*, 2011; *Liu et al.*, 2013c]. In their results, the decrease in the thermal pressure lasted less than two minutes and then increased above background level. The transient drop in the pressure is related to a localized current structure surrounding the dipolarization front rather than a global SCW. As shown in Figure 5.1, both transient and prolonged pressure gradients are observed. The transient pressure gradient was observed to be associated with decreases in the equatorial pressure when flows were present; the prolonged pressure gradient was observed to be associated with increased equatorial pressure even when no flow was present. The transient pressure gradient is usually related to a narrow current system

(current wedgelet) [*Birn and Hesse*, 2013; *Liu et al.*, 2015] and the prolonged pressure gradient to the global SCW.

Because the pressure gradient sustains the global SCW, the pressure gradient pattern was investigated in the SCW frame. Figure 5.6 demonstrates that $\delta\nabla P_x$ increased for almost all substorm events, suggesting that the thermal pressure is higher toward the Earth. The $\delta\nabla P_y$ decreased on the duskside of the central meridian and increased on the dawnside, pointing toward the central meridian on either side. Therefore, it can be concluded that the azimuthal pressure gradient is well organized in the SCW frame, suggesting that the pressure is higher closer to the CM of the SCW. In other words, the center of the high pressure created by flow braking is co-located with the CM of the SCW. This is consistent with FAC generations on each side of the flows, as shown in Figure 5.4. In addition, both $\delta\nabla P_x$ and $\delta\nabla P_y$ are larger on the duskside than on the dawnside, which corresponds to stronger current density of the FACs. The asymmetry in the pressure gradient may be responsible for an asymmetric SCW (with narrower, stronger upward FACs and weaker, wider downward FACs). The results also suggest that the earthward flow heats the ambient plasma as it travels earthward, leaving a high pressure region behind. The equatorial pressure increases not only in near-Earth region within 12 R_E but also in the mid-tail region. The pressure increased more than the magnetic field B_Z in the near-Earth region, and less in mid tail. Although the plasma density drops in the mid tail, the temperature increases significantly to overcompensate for the density decrease.

The current density of FACs is determined not only by pressure gradient ∇P but also

by the gradient of flux tube volume ∇V. However, ∇V cannot be obtained from in situ observations since it is determined by an integration from the magnetosphere to the ionosphere. It can, however, be roughly inferred from the magnetic dipolarization. In the dipolarization region, the Bz increases and the flux tube volume V decreases. It results in the ∇V pointing away from the central meridian or the dipolarization region. This configuration of the equatorial pressure and gradient of the flux tube volume is similar to the RCM-E simulation of an idealized plasma sheet bubble (Figure 5 in [*Yang et al.*, 2011]), in which a quadrupole pattern of FACs is generated.

Substorm current wedge formation is illustrated in Figure 5.7. Magnetic reconnection generates an earthward flow with dipolarization front (or reconnection front) [*Angelopoulos et al.,* 2013], that accelerates the plasma ahead of it and forms a high-pressure front [*Zhou et al.*, 2014a]. The currents surrounding a dipolarization front are related to narrow current wedgelets in the ionosphere [*Liu et al.*, 2013b; *Liu et al.*, 2015]. As the flow approaches the near-Earth region, especially the transition region, it is quickly slowed down and diverted azimuthally [*McPherron et al.*, 2011]. Flow braking and diversion create two flow vortices on each side and a high-pressure region. Initially at the onset, both the flow vortices and the pressure gradient generate FACs feeding the SCW [*Keiling et al.*, 2009; *Yao et al.*, 2012]. The flow vortices disappear within several minutes as the flow vanishes. The high pressure lasts for about an hour and the associated pressure gradient sustains the SCW. The peak of magnetic dipolarization is located more tailward than the high-pressure region as illustrated in Figure 5.7. According to the Vasyliunas equation, nonalignment between their gradients generates an SCW with

quadrupole FACs. The outer current loop is a classic SCW, which is region-1-sense; the inner current loop is a region-2-sense current loop. The existence of quadrupole SCW was also suggested by previous simulations [*Yang et al.*, 2011; *Birn and Hesse*, 2014] and observations [*Sergeev et al.*, 2014b]. The combined magnetic effects of these FACs on the ground and at geosynchronous orbit can be represented by their net current, which is similar to a classic SCW.

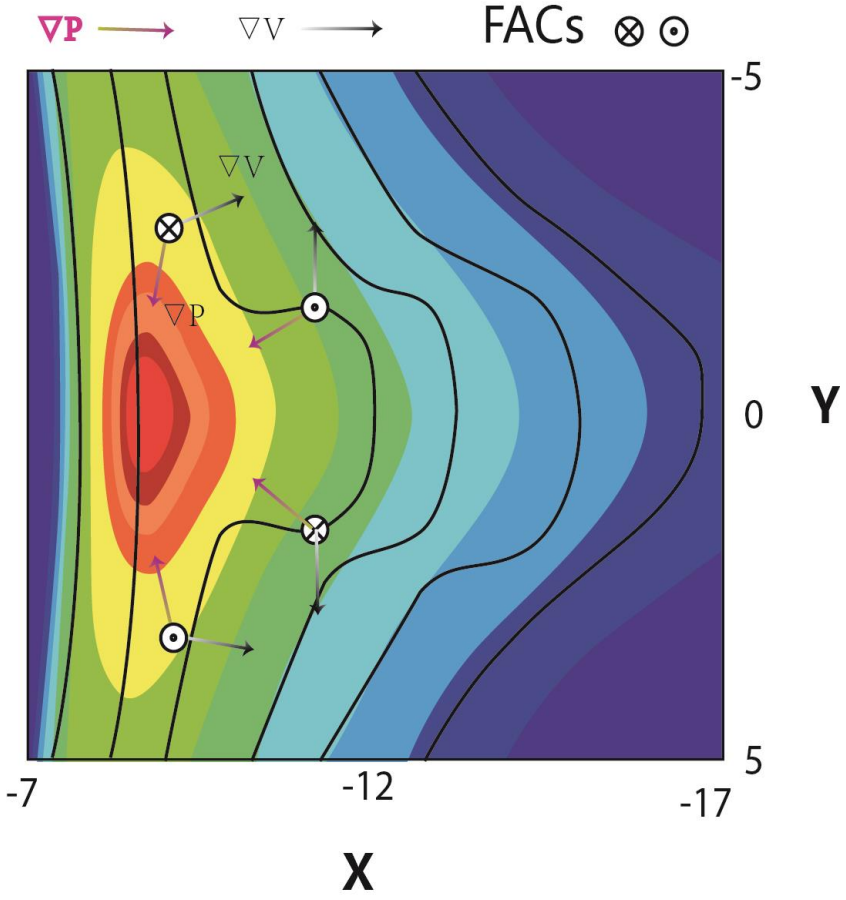

Figure 5.7. Illustration of substorm current wedge formation. The colored contours show the plasma pressure on the equator. The lines are the contours of the magnetic field B_Z. The purple and black vectors represent the gradient of thermal pressure and flux tube

volume. The directions of the FACs are obtained from the Vasyliunas equation.

5.5 Conclusions

In this chapter, substorm current wedge formation is investigated using the earthward flows observed during five THEMIS tail seasons and substorm onsets identified using the MPB index. Flow occurrence is found to have peaked at substorm onset in the time delay analysis between substorm onsets and the flows observed within 12 R_E, where the flow speed dropped significantly. The good temporal correlation suggests that SCW formation is highly correlated with the flow braking process. In addition, it is found that most (85%) of the onset-associated flows were located inside the SCW between two FACs. Such a good spatial correlation suggests that FACs are generated on both sides of the flows. Then thermal pressure and flow vortices relative to the flow onsets are investigated. The equatorial thermal pressure is found to have lasted for about an hour, which is comparable to the durations of FACs and westward electrojet in the SCW. The flows associated with flow vortices, on the other hand, lasted for less than 3 minutes, which was significantly shorter than the SCW. Therefore, the SCW is likely sustained by high pressure generated in the flow braking process rather than transient flow vortices. Furthermore, the pressure gradient is found to be well organized in the SCW frame. The ∇P_x increased for almost all substorms; the ∇P_y increased on its dawnside of the central meridian and decreased on its duskside. This suggests that the center of the high pressure region caused by flow braking is co-located with the central meridian of the SCW, which is consistent with the result that FACs are generated on both sides of the flows. Although

the gradient of the flux tube volume cannot be obtained from in situ observations, it can be inferred from the magnetic dipolarization of B_Z. The flux tube volume is smaller in the dipolarization region. Therefore the ∇V points away from the central meridian, which is consistent with simulation results. The nonalignment between the gradient of the flux tube volume and pressure can generate an SCW with quadrupole FACs. Their combined magnetic effects on the ground and at geosynchronous orbit are similar to their net current, which is a classic one-loop SCW.

Chapter 6

Magnetotail flux accumulation leads to auroral expansion and a substorm current wedge: case study

Reconnection-generated earthward flows, magnetic field dipolarization, and auroral expansion are related to substorm current wedge (SCW) development. Field-aligned currents (FACs) of the SCW have been suggested to be generated by flow vortices, pressure gradients, or both. Related observations have shown that the generation mechanism differs from one event to another, perhaps due to the different observation location relative to the SCW central meridian and time relative to the SCW's evolutionary state. A pattern of space observations consistent with a generation mechanism has yet to emerge. Interpreting these observations relies on FAC locations, which are unknown because magnetotail observations are scarce. To solve this problem, a newly-developed SCW inversion technique was used to determine FAC locations and analyze connections among magnetospheric and ionospheric phenomena. Then I analyzed magnetic flux, a parameter less reliant on FAC locations, during an isolated substorm on 13 February 2008 (same event discussed in Chapter 4). The temporal variation of flux released by reconnection and transported by earthward flows was calculated. Some transported flux accumulated in the near-Earth region and some was transported azimuthally by flow diversion. Temporal variations of the accumulated flux that causes magnetic dipolarization in the SCW and of the flux within the auroral

poleward boundary were calculated. They are in good agreement with the flux transported by earthward flows. This agreement suggests that the accumulation of the magnetic flux generated the SCW, causing magnetic dipolarization and auroral poleward expansion. The amount of accumulated flux appears to be positively correlated with the amplitudes of these substorm-related phenomena.

6.1 Introduction

A magnetospheric substorm is an important unloading process in the magnetosphere during which magnetic reconnection converts open magnetic flux in the lobes into closed magnetic flux in the plasma sheet and lobe magnetic energy into thermal and kinetic energy of fast flows. Earthward fast flows, which transport magnetic flux and energy into the inner magnetosphere, usually stop at around 8-10 R_E [*Angelopoulos et al.*, 1992; *McPherron et al.*, 2011; *Hsu et al.*, 2012; *Runov et al.*, 2014; *Sergeev et al.*, 2014a]. Flow braking creates a high pressure region that diverts these flows, distorting magnetic field lines and generating field-aligned currents (FACs) in a substorm current wedge (SCW) [*Birn and Hesse*, 2014; *Kepko et al.*, 2014]. Field-aligned currents, which are connected through the westward electrojet, cause auroral brightening in the ionosphere [*Akasofu*, 1964; *McPherron et al.*, 1973]. After brightening, the aurora expands poleward as the substorm current wedge strengthens and magnetic field lines become more dipolarized [*Chu et al.*, 2015c].

The mechanism that generates FACs has been studied using theory, observations, and simulations [*Birn et al.*, 1999; *Keiling et al.*, 2009; *Xing et al.*, 2010; *Yao et al.*, 2012;

Birn and Hesse, 2014]. Theories suggest that the FACs are generated by inertial current, flow vortices, and pressure gradients [*Vasyliunas*, 1970]. The inertial current is usually neglected because it is considerably smaller than the flow vortices and pressure gradients [*Birn et al.*, 1999]. Addressing FAC generation by interpreting in-situ observations of flow vortices and pressure gradients requires FAC location. These locations are unknown, however, because such in-situ observations are scarce. Using our recently developed inversion technique for SCW with ground magnetometer data, the locations of FACs were obtained [*Chu et al.*, 2014b]. In addition, field-aligned currents in an SCW, which connect the magnetospheric source region to aurora in the ionosphere, usually flow along magnetic field lines calculated using a magnetospheric model (Tsyganenko model) [*Tsyganenko and Stern*, 1996]. This magnetospheric model, however, is inaccurate during substorms because the most important current, the SCW, is missing. Thus, the aurora expands poleward during substorm expansion phase, and sometimes reaches a latitude that maps to the distant tail rather than the flow braking region. Mapping flows to aurora has been improved using a dynamic magnetospheric model that takes substorm currents into account using the inversion technique for SCW [*Chu et al.*, 2015c]). Even with FAC location information, in-situ observations are sometimes transient and localized and not necessarily related to a global SCW. Therefore, a global parameter, less reliant on FAC locations and areas, is needed to determine the strengths of FACs in the SCW and the strength of substorm-related phenomena. Such a global parameter, magnetic flux transported and accumulated at the inner edge of the plasma sheet, which can be calculated from both spacecraft and ground observations, helps elucidate

substorm current wedge generation.

Magnetic flux transport and accumulation during an isolated substorm on 13 February 2008 was analyzed (same event as discussed in Chapter 4). Using different methods, magnetic flux associated with various substorm phenomena were found to be comparable: transported by earthward flows, accumulated in the inner magnetosphere causing magnetic dipolarization inside the SCW, and responsible for auroral expansion. It was shown that magnetic flux released by tail reconnection is partly accumulated in the inner magnetosphere and partly diverted azimuthally. Magnetic flux transported by earthward flows and accumulated in the inner magnetosphere is consistent with that responsible for SCW generation and auroral poleward expansion. Section 2 describes the database used in this study. Observations are presented in section 3 and discussion in section 4.

6.2 Data and model

Data from the identically-instrumented Time History of Events and Macroscale Interactions during Substorms (THEMIS) probes P1, P3, and P4, were used. P3 ([-10.0, 3.3, -2.2] R_E in GSM coordinates and same thereafter) and P4 ([-8.8, 3.9, -1.8] R_E) were located in the plasma sheet in premidnight region and P1([-27.4, 10.0, -5.2] R_E) was located in the magnetotail at 0240 UT [*Angelopoulos*, 2008]. The Flux Gate Magnetometer (FGM) [*Auster et al.*, 2008] provides three second spin averaged magnetic field; the electrostatic analyzer (ESA) [*McFadden et al.*, 2008] obtains ion and electron measurements in the 5 eV to 25 eV energy range and the Solid State Telescope (SST) [*Angelopoulos*, 2008] obtains them in the 30 keV to 1 MeV range. Auroral observations

were provided by all-sky imagers (ASI) with a time resolution of 3 seconds [*Mende et al.*, 2008]. The auroral electrojet index (AE, AU and AL) is calculated from THEMIS ground magnetometers at a time resolution of 20 sec [*Russell et al.*, 2008]. The midlatitude positive bay (MPB) index is calculated using magnetic field data from INTERMAGNET and SuperMAG ground magnetometers at midlatitudes at a time resolution of 1 min [*Chu et al.*, 2015a]. The MPB index represents the amplitude of the MPB signature, therefore it measures the strength of the SCW. The interplanetary magnetic field (IMF) and plasma measurement are obtained from Geotail shifted to the bow shock [*Weimer et al.*, 2003; *Weimer*, 2004]. The mapping is computed using a dynamic magnetospheric model, which includes dynamic substorm currents (the SCW, the ring current and the partial ring current) [*Chu et al.*, 2015c]. The strengths and locations of the substorm currents are obtained every minute from SCW inversion technique using ground magnetometer data [*Chu et al.*, 2014b].

6.3 Observations

6.3.1 Substorm overview

An isolated substorm was observed by THEMIS probes P1, P3, and P4 between 0200 UT and 0400 UT on 13 February 2008. Figure 6.1 shows the positions of those probes on the equatorial plane (Figure 6.1a) and noon-midnight meridian plane (Figure 6.1b) in GSM coordinates. P3 and P4 were located above and near the magnetic equator in the premidnight region.

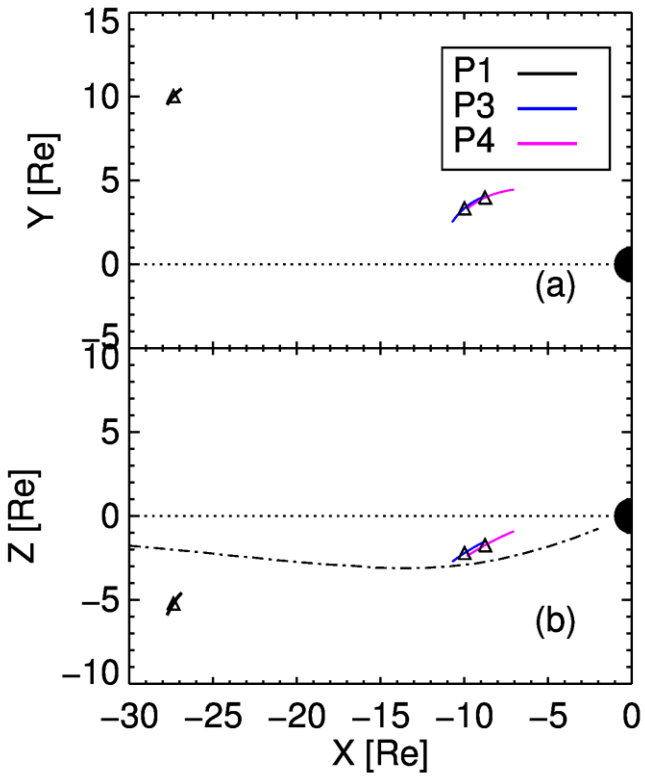

Figure 6.1 Projection of THEMIS P1 (black), P3 (blue), and P4 (purple) in the equatorial plane (a) and noon-midnight meridian plane (b) in GSM coordinates from 0200 to 0400 UT on 13 February 2008. Their locations at the onset (0237 UT) are marked by triangles. The magnetic equator represented by the dotted-dashed line in (b).

Figure 6.2 shows an overview of the substorm. The MPB and AL indices (Figure 6.2a), which measure the field-aligned current and the westward electrojet parts of the SCW, respectively, started to change sharply at 02:37 UT. The AL index reached its minimum at 02:46 UT and the MPB index peaked later at 02:58 UT. Auroral brightening and poleward expansion are illustrated using the auroral keogram obtained from the ASI at KUUJ (Figure 6.2b). The aurora first brightened at 68 °(magnetic latitude) at 02:37:12

UT (auroral onset), then expanded poleward and reached the most poleward edge at 02:57 UT. The purple line shows the temporal variation of THEMIS P4's revised footprint calculated using the dynamic magnetospheric model, which was in good agreement with the auroral poleward expansion [*Chu et al.*, 2015c]. Successive earthward flows were observed at P3 and P4 (Figure 6.2d and 6.2f) at onset and later during the substorm. Those flows were accompanied by transient magnetic dipolarizations or fluctuations (several minutes) and longer lasting dipolarization (tens of minutes) (see B_z increase and B_x decrease in figure 6.2c and 6.2e). On the other hand, the changes in B_y were always associated with flows. Therefore, the changes in B_y were due to localized passing of flows rather than global change in the magnetic field configuration due to global SCW. The earthward flux transport rate per unit length (2h) was calculated from the integration of the electric field E_y at P3 and P4 (2g) using $\Phi_{flow}/l_{flow} = \int E_y dt = \int -(V \times B)_y dt$. The electric field was calculated from the ion bulk velocity and the magnetic field. Φ_{flow} is the earthward flux transport and l_{flow} is the width of the flows. At P3 and P4 E_y was comparable during the substorm except for a sharp spike observed by P3 at onset (see Figure 6.5 for enlarged plot) that was likely due to a localized flow vortex. The earthward flows transported about 40 MWb/R_E of magnetic flux during this event at P4. The cumulative flux transport rate at P3 was lower than at P4, likely because P4 was closer to the center of the flows. The azimuthal transport rate per unit length (2i) was calculated using $\Phi_{dusk}/l_{flow} = \int(-E_x)dt = \int(V \times B)_x dt$. It was mainly duskward because the probes were located premidnight and the flows were diverted

duskward. The duskward flux transport was about 35 MWb/R_E, comparable to the earthward flux transport rate. Note that, due to different widths (l_{flow}) of the earthward and duskward flows, the amounts of magnetic flux transported earthward Φ_{flow} and duskward Φ_{dusk} were not necessarily comparable. The duskward transport rate was much higher at P3 than P4 during this event except the first several minutes. It suggests that more flux was diverted duskward at locations further tailward.

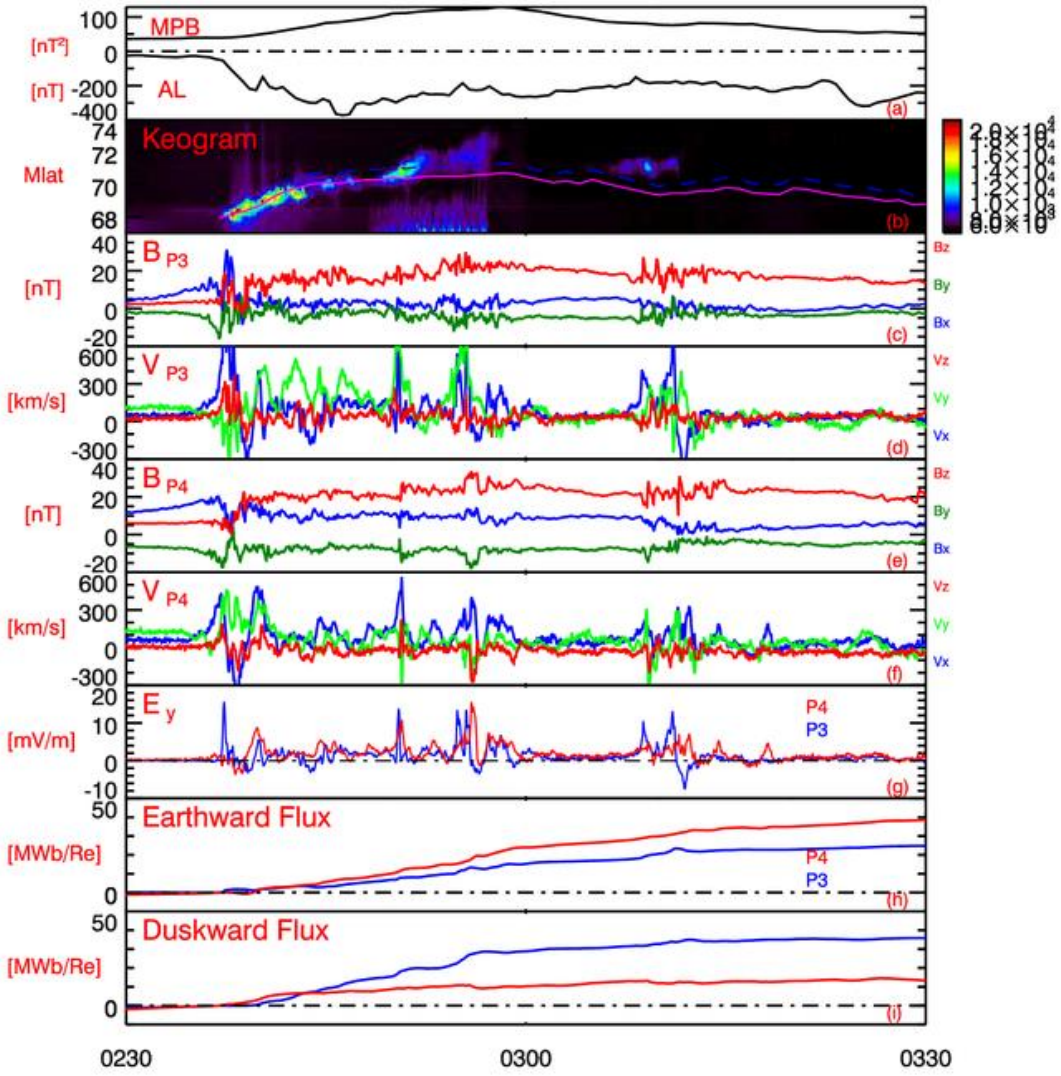

Figure 6.2 Overview of observations of the MPB and AL indices, the aurora from THEMIS ASI and flows from P3 and P4. The MPB index and the AL index were shown in Figure 6.2a. The auroral keogram obtained from the ASI at KUUJ ((13.23°, 66.89°) in magnetic coordinates) was shown in Figure 6.2b. The magnetic field and plasma velocity from THEMIS P3 and P4 are shown in the next four panels. The earthward and duskward flux transport rates are shown in the last two panels.

6.3.2 Auroral observations

Figure 6.3 shows auroral snapshots from THEMIS ASI located at KUUJ ((13.23°, 66.89°) in magnetic coordinates) at 02:37:00 UT (before auroral onset), 02:39:00 UT (after onset), 02:42:30 UT, and 02:50:00 UT. The black patch at the center of each snapshot is the artifact of removing the moon (See [*Chu et al.*, 2015c] for details). The bright light in the bottom (Figure 6.3d) is contamination from cars. Before the auroral onset (02:37:12 UT), KUUJ was located about 2.4 hour premidnight. The pre-existing arc extended through the field-of-view (FOV) of KUUJ and two other ASIs to the left (SNKQ and GILL, not shown here. See figure 5 in [*Chu et al.*, 2015c]). After onset, the aurora brightened in the east of the FOV and then expanded poleward and westward. At 02:50 UT, the aurora reached 71° in magnetic latitude and extended for 30° (between -5° and 24°) in magnetic longitude. The poleward boundary of the aurora is marked by a black line (figure 6.3b, 6.3c and 6.3d); the lower line denotes the quiet-time boundary through the pre-existing arc (Figure 6.3a). Magnetic flux corresponding to the auroral poleward expansion could be estimated using the magnetic flux between two boundaries.

It was calculated using $\Phi_{aurora} = \int B_z \cdot dS$ and its temporal variation is shown in Figure 6.5.

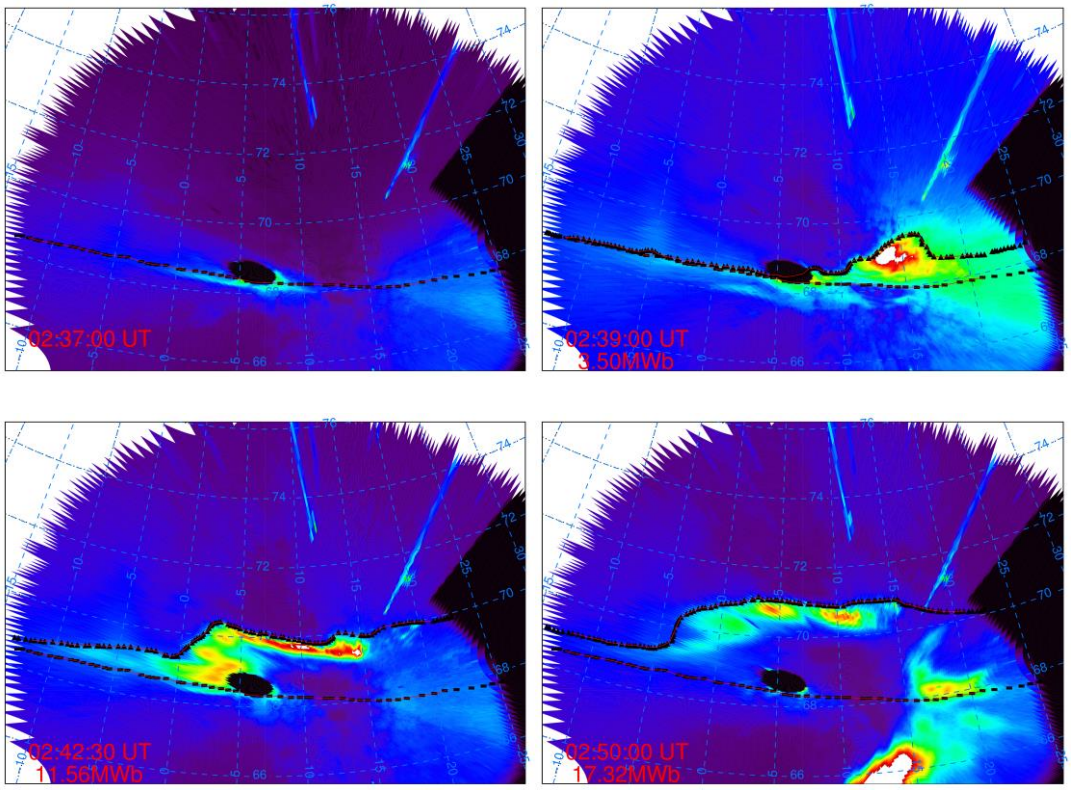

Figure 6.3 Auroral observations from THEMIS ASI KUUJ in magnetic coordinates at the following times: 02:37:00 UT (before the auroral onset), 02:39:00 UT (after the onset), 02:42:30 UT and 02:50:00 UT. The patch at the center of each snapshot was the moon. The bright light in the bottom of Figure 6.3d was light contamination from cars. The poleward boundary was marked in each figure. The poleward boundary of the quiet-time pre-existing arc was marked with dashed lines for reference.

6.3.3 Substorm current wedge-induced dipolarization

Figure 6.4 shows the magnetic perturbation ΔB_z induced by the current wedge on the equatorial plane at 02:44:00 UT. The parameters describing the substorm currents (strengths and locations) were calculated using the inversion model for SCW shown in figure 4 of *Chu et al.* [2014b]. At 02:44:00 UT, the strength of the SCW was ~0.18 MA and its width was ~7.5 hours in magnetic local time. The magnetic perturbation ΔB_z was positive inside two FACs. ΔB_z was strongest immediately earthward of the tail closure of the SCW connecting two equatorial FAC footprints, which represented cross-tail current reduction. Tailward the SCW, ΔB_z was slightly negative. The polarity of ΔB_z changes along longitude or local time was consistent with the H (positive northward) component of the midlatitude positive bay on the ground. In the tail at X= -10 Re, the ΔB_z was consistent with magnetic dipolarizations, and the negative change (tailward of the SCW) was consistent with the ΔB_z decrease after the earthward flows passed [*Liu et al.*, 2013b]. ΔB_z was not symmetric with respective to SCW's central meridian. It was stronger on the dusk side because the upward FAC was more concentrated and the downward FAC was wider. The magnetic flux inside the SCW can be obtained by integrating ΔB_z on the equatorial plane. In this study, the magnetic flux Φ_{SCW} has been integrated in the local time sector corresponding to the auroral brightening region, which covered about 30 degrees in magnetic longitude (Figure 6.3d). At 02:44:00 UT, magnetic flux of Φ_{SCW} =~19.2 MWb was accumulated in the shaded area inside the SCW. Its temporal variation is shown in Figure 6.5.

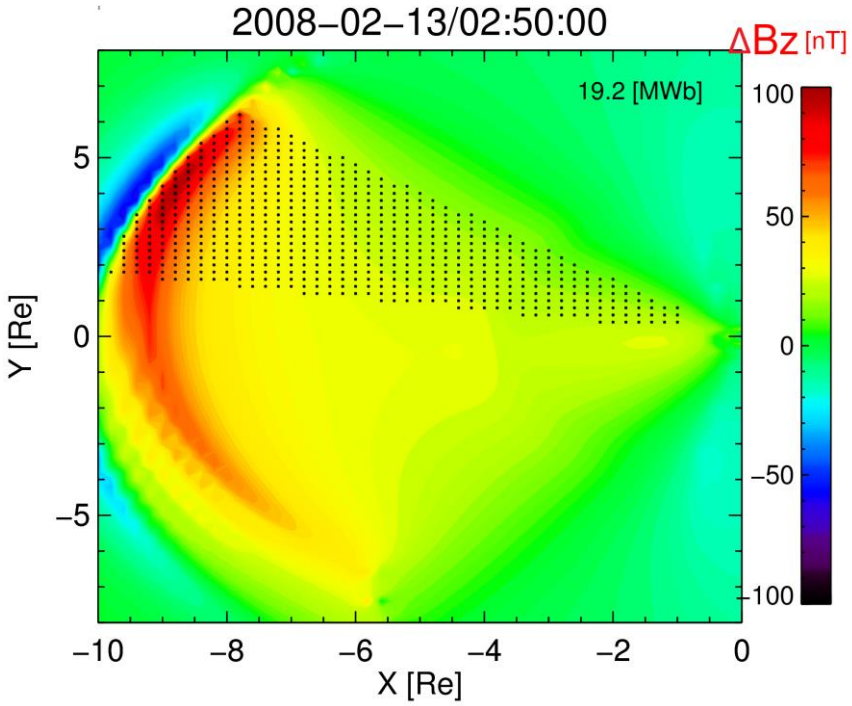

Figure 6.4 Colored contour of magnetic perturbation ΔBz by the SCW on the equatorial plane at 02:50 UT. The area corresponding to the auroral brightening regions are marked as shaded area. The magnetic flux by the SCW in the shaded area is labeled.

6.3.4 Magnetic flux accumulation

In our previous work auroral poleward expansion was found to be mostly caused by the mapping effect of substorm currents that project the satellite footprint to higher latitude as the magnetic field becomes more dipolar [*Chu et al.*, 2015c]. Both auroral poleward expansion and magnetic dipolarization were closely related to flux accumulation in the near-Earth region. In this section, the temporal variation of the magnetic flux is compared using three different methods: magnetic flux transported by earthward flows; flux accumulated inside the SCW causing dipolarization; and flux

enclosed in the auroral bulge. The temporal variations of these magnetic flux calculated by each method between 0235 and 0250 UT are shown in Figure 6.5. Note that the flux transport rate (per R_E) carried by the flows (figure 6.2h and 6.2i) was calculated. And the width of the flows was estimated to be ~4±0.5 R_E based on auroral brightening as mapped to the equatorial plane (the shaded area in Figure 6.4). The blue and red lines show the earthward magnetic flux carried by P3 (blue) and P4 (red). Magnetic flux increased continuously during the substorm expansion phase. During the first three minutes after onset, the earthward flux at P3 was larger than at P4 because P3 was located nearer to the center of the first flow, as P3 observed strong earthward flow while P4 observed a flow vortex (figure 6.2d and 6.2f). At the same time, brightening of the aurora and its poleward expansion were also near the footprint of P3 (Figure 6.3b). Later during the substorm, the flux transport at P4 became comparable and exceeded that at P3 as successive flows arrived. In the meantime, the auroral brightening and poleward expansion were close to the footprint of P4 instead. These observations suggested that transportation of magnetic flux by flows at different local times caused the auroral brightening and poleward expansion at corresponding local times.

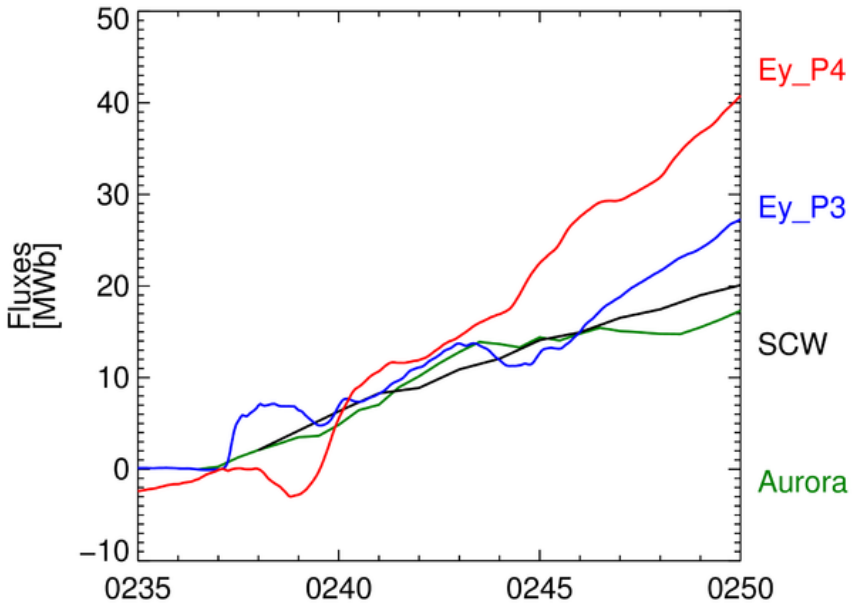

Figure 6.5 Comparison among the temporal variations of the magnetic flux Φ_{SCW} (black), Φ_{aurora} (green) and Φ_{flows} at THEMIS P3 (blue) and P4 (red).

In Figure 6.5, the temporal variation of Φ_{aurora} is shown in green. Before 02:43 UT, Φ_{aurora} was comparable to Φ_{flows}. Later, it became smaller than Φ_{flows}. Auroral intensification was the signature of flows in the magnetotail. The auroral poleward boundary, which mapped more tailward than the flows, indicated the tailward boundary of the flows. The poleward boundary also represented the tailward boundary of intense flux transport. Therefore, Φ_{aurora} represented the accumulated magnetic flux transported by the flows toward the Earth. The fact that Φ_{aurora} was initially comparable to Φ_{flows} and became smaller later suggests that Φ_{flows} accumulated during the early expansion phase, and then part of the flux was transported away by magnetospheric convection. In Figure 6.5, the temporal variation of Φ_{SCW} is shown in black. It represents the magnetic flux responsible for the magnetic dipolarization and the corresponding SCW in the inner

magnetosphere.

During the expansion phase, the magnetic flux accumulated and created the dipolarization in this region. In this process, the plasma pressure and magnetic pressure bent the magnetic field lines and balanced the curvature force of the field lines. The rotation of the field lines was consistent with polarity of field-aligned currents, which fed the SCW. The degree to which the magnetic field lines were distorted also depended on the amount of magnetic flux accumulated. Therefore, the strength of the SCW was relevant to the accumulated magnetic flux. Not all the earthward flux was accumulated in the near-Earth region, however. The magnetospheric convection was initially balanced before the substorm and was enhanced during substorm expansion and recovery phase. The enhanced convection transported the magnetic flux away from the near-Earth region. This was why Φ_{SCW} and Φ_{aurora} were close to Φ_{flows} at first and became smaller later.

6.3.5 Magnetic reconnection

Figure 6.6 is an overview of observations at P1 ([-27.4, 10.0,-5.2] R_E), which was well positioned in the magnetotail to observe magnetic reconnection. THEMIS P1 was located below the magnetic equator (Figure 6.1b), and B_x was negative (Figure 6.5a). Around the onset (02:37 UT), a traveling compression region (TCR) was observed travelling tailward by P1. The strength of B_x suddenly decreased (became less negative) from 02:38:00 UT, reached a minimum at 02:39:18 UT, and then recovered around 02:44 UT. Initially close to zero, B_z became negative at 02:37:51 UT. It reached its most negative value at 02:39:21 UT and then returned to almost zero at around 02:44 UT.

Before the TCR, B_y had a positive background. During the TCR, B_y became more positive (duskward). All these observations of the TCR suggested that a plasmoid passed P1 on its dawn side. The relatively slow change in $|B_x|$ between 02:35 UT and 02:38 UT (before the TCR) was not likely caused by the TCR because B_y and B_z did not change. The thermal (red), magnetic (blue) and total (black) pressures at P1 are shown in Figure 6.6b. The decrease in the magnetic pressure and the increase in the thermal pressure were also evidences of a TCR. The total pressure continued to increase during the growth phase before onset and dropped sharply near onset. After that, the total pressure continued to decrease at a lower rate. After 03:10 UT (not shown), the thermal pressure is almost zero, suggesting that either the plasma sheet was totally depleted or P1 had entered the lobe.

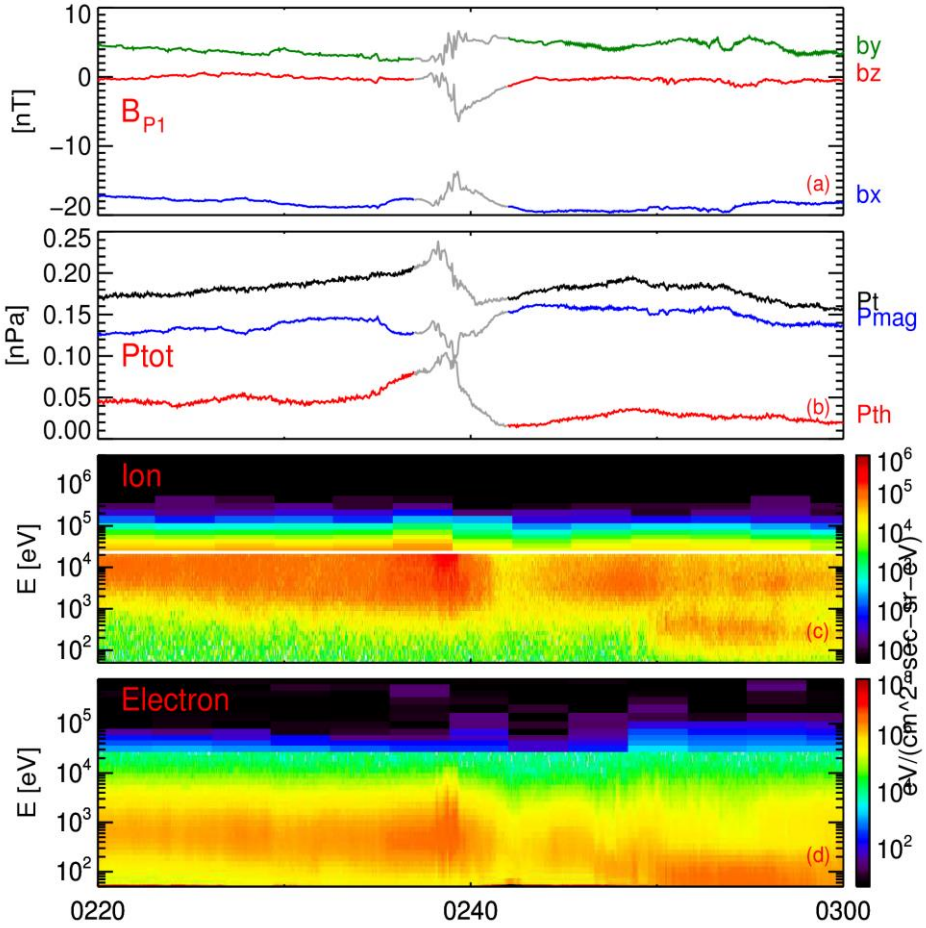

Figure 6.6 Observations from THEMIS P1 ([-27.4, 10.0,-5.2] R_E) in the tail: (a) the magnetic field (b) thermal (red), magnetic (blue) and total (black) pressures. The time interval of the TCR is plotted in grey. Panels (c) and (d) are ion and electron energy spectrum combined from both the SST and ESA instruments.

Decrease in the total pressure indicates conversion of lobe flux to closed field line by magnetic reconnection. To estimate the change in the lobe flux, the magnetic field strength and the radius of the lobe are needed. The lobe field strength B_{lobe} was calculated based on the assumption of pressure balance $P_{lobe} = \frac{B_{lobe}^2}{2\mu_0} = P_{total} = P_{thermal} + P_{mag}$.

This assumption might not hold during plasmoid passage, however, because of the curvature force. Hence the interval of the plasmoid has been plotted in grey from 02:37:00 UT to 02:42:00 UT in Figure 6.6. The lobe field B_{lobe} in the same interval in Figure 6.7e is plotted in grey.

The lobe radius was obtained using two different magnetopause models: the Shue98 model [*Shue et al.*, 1998] and the Shukhtina09 model [*Shukhtina et al.*, 2009]. The Shue98 model is a statistical model; its input parameters are solar wind dynamic pressure and IMF B_z. The Shukhtina09 model is a dynamic model that determines the lobe radius by calculating the flaring angle α assuming pressure balance at the magnetopause between solar wind dynamic, thermal, and magnetic pressures and total pressure inside the magnetosphere.

$$0.88P_d sin^2\alpha + B_{SW}^2 + P_{thSW} = \frac{B_{lobe}^2}{2\mu_0}$$

On the left side, its input parameters include the solar wind dynamic, magnetic and thermal pressures. They are balanced by the total pressure in the lobe on the right side. Figure 6.7 shows the solar wind dynamic pressure and the IMF B_z at the bow shock (solid) and propagated to P1's location at X =-27.4 R_E (dotted line), the lobe radius, the lobe magnetic field strength, the lobe open flux Φ_{lobe} and its first derivative $d\Phi_{lobe}/dt$. Solar wind dynamic pressure and IMF B_z were obtained from Geotail upstream of the Earth and propagated to the nominal bow shock (about 17 R_E) [*Weimer et al.*, 2003; *Weimer*, 2004]. During this event, the dynamic pressure increased from 2.0 nPa to 3.0 nPa. The IMF B_z was southward for about half an hour and turned northward before onset. To

calculate the lobe radius, the solar wind dynamic pressure and IMF B_z were further propagated to P1's location X=-27.4 R_E (dotted line). Because the thermal and magnetic pressures in the solar wind were much smaller than the dynamic pressure they were not shown in the figure (considered in the calculation). The lobe radius from both models (Figure 6.7c) had similar trends. Figure 6.7 shows that the lobe radius from two models increased slowly during the growth phase before onset, then dropped during the expansion and recovery phase after onset. The lobe radius calculated using Shue98 model was generally larger than the lobe radius from Shukhtina09 model. This was most likely because Shue98 is a statistical model while Shukhtina09 model required in-situ measurements from the tail. The lobe field strength increased during the growth phase, and dropped sharply after TCR passage. The lobe open flux from two models (Figure 6.7e) showed similar trends and decreased by about ~0.10 MWb after plasmoid passage. Note that the interval of the plasmoid has been plotted in grey as well because the total pressure might be local due to the curvature and not mapping to the magnetopause. The open flux continued to decrease after 02:50 UT, and dropped to a minimum around 03:10 UT (not shown here). The changes of the open fluxes every 3 minutes (Figure 6.7f) are shown for comparison between two models. Although the absolute values of lobe flux given by two models were different, their changes were very close. About 0.10-0.15 GWb (100-150 MWb) of magnetic flux was released by magnetic reconnection in the first five minutes after substorm onset. Two more flux drops were observed at 02:49 UT and 02:55 UT (red arrows), which were close to when two other flows observed by P3 and P4 as indicated by red arrows.

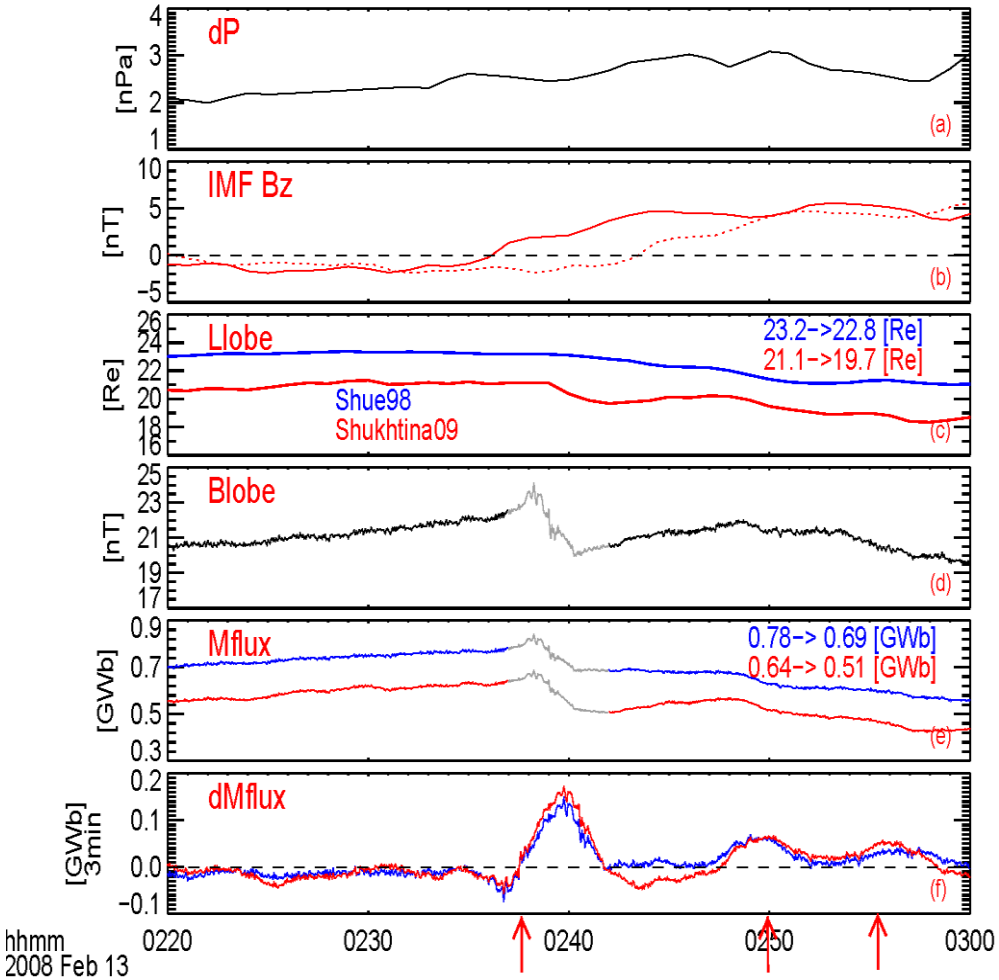

Figure 6.7. Observations used to calculate the lobe open flux: (a) and (b) the dynamic pressure and IMF Bz propagated to the nominal bow shock; the dashed line in panel (b) is the IMF Bz propagated to P1's location; (c) the lobe radius obtained using Shue 98 model (blue) and Shukhtina 09 model (red); (d) the lobe magnetic field strength obtained from P1; (e) the lobe open flux from Shue 98 (blue) and Shukhtina 09 (red) models; the time interval of the TCR is plotted in grey; (f) 3-min time derivative of the lobe open flux. The red arrows showed the flows observed by P3 and P4.

6.4 Discussion

6.4.1 Magnetic flux and SCW

In this study, magnetic flux accumulation and its relationship to substorm phenomena were analyzed during an isolated substorm on 13 February 2008. Various methods were used to calculate the amount of magnetic flux transported by earthward flows (Φ_{flows}), accumulated inside the SCW causing dipolarization (Φ_{SCW}), and enclosed in the auroral bulge (Φ_{aurora}). Φ_{flow} is magnetic flux transported by earthward flows into the inner magnetosphere from the reconnection site in the tail. Φ_{SCW} is the amount of magnetic flux that causes longer-lasting dipolarization (tens of minutes) and the magnetic flux needed to generate the SCW. Additional magnetic flux below the auroral poleward boundary in the auroral oval (the flux needed to map auroral source region to higher latitude) is represented by Φ_{aurora}. Note that later flows were observed at the same tail location. Figure 6.5 shows good agreement for magnetic flux calculated for three different types of observations using different methods. The good agreement between Φ_{SCW} and Φ_{aurora} suggests that the amount of magnetic flux responsible for magnetic dipolarization in SCW determines the amplitude of auroral poleward expansion. Consequently, auroral poleward expansion can be calculated by considering the dipolarization effect of the SCW. The good correlations between Φ_{flows} and other two fluxes suggests that the amplitudes of the SCW and auroral poleward expansion were determined by the magnetic flux transported and accumulated by earthward flows. Flux accumulation resulted in magnetic dipolarization, which in turn caused auroral poleward expansion. These three

good agreements demonstrate that magnetic flux accumulation generated the SCW and magnetic dipolarization, causing auroral poleward expansion. The amplitude of these processes was determined by the amount of accumulated magnetic flux from earthward flows.

Magnetic flux can be accumulated by a single flow or by successive flows. As magnetic flux accumulates, the resulting high-pressure region behaves like a barrier, slowing down and diverting later flows. Flux accumulated by successive flows contributes to SCW buildup; additional flux further dipolarizes magnetic field lines and generates stronger FACs. As more flux is added, the flux accumulation region sometimes retreats tailward [*Ohtani et al.*, 1992a; *Angelopoulos et al.*, 1996; *Baumjohann et al.*, 1999; *Pu et al.*, 2001; *Zhang et al.*, 2007; *Cao et al.*, 2012; *Angelopoulos et al.*, 2013]. In this event, however, all successive flows were observed by P3 and P4, suggesting that the accumulation region did not retreat tailward significantly. It has also been proposed that multiple simultaneous flows at different local times can generate many narrow current wedgelets, which might have magnetic effects similar to those of a global SCW [*Birn and Hesse*, 2013; *Liu et al.*, 2015]. However, simultaneous flows at different local times are rare because the occurrence of flows and pi2 pulsations peaks at ~15 minutes [*Kepko et al.*, 2001; *Hsu and McPherron*, 2007; *Keiling and Takahashi*, 2011; *McPherron et al.*, 2011; *Hsu et al.*, 2012]. In addition, the timescale of these current wedgelet was ~ 2 min, significantly shorter than that of substorms (~ 1 hour). Furthermore, only localized magnetic perturbations were observed before flow arrival [*Zhang et al.*, 2011]. These facts suggest that the currents surrounding the flows were not

or only partially connected to the ionosphere and did not lead to notable FACs to the ionosphere before the flows were slowed down [*Birn and Hesse*, 2014].

An outstanding question is how flows that last minutes sustain a substorm that lasts tens of minutes. This study suggests a scenario of global SCW generation by magnetic flux accumulation that is different from the wedgelet scenario. In this event, the magnetic flux from the flows accumulated and created a high-pressure region with highly dipolarized magnetic field lines, the rotation of which generated FACs. This high-pressure region persisted for tens of minutes even in the absence of flow. Substorm-related phenomena (flux accumulation, dipolarization in the near-Earth region, auroral poleward expansion, the SCW, and the westward electrojet) also lasted for tens of minutes. Furthermore, the amounts of magnetic flux responsible for these phenomena lasted for tens of minutes. In addition, it was found that one flow could carry enough magnetic flux to create a global SCW. Successive flows could further contribute to a global SCW by accumulating more magnetic flux, which further bent and dipolarized the magnetic field lines and generated stronger FACs. All the evidences above support generation of a global SCW by magnetic flux accumulation by flows.

It should be pointed out that there is growing evidence that there is a second weaker current wedge underneath the main current wedge at the same local time with current flowing in opposite direction [*Raeder and McPherron* 1998; *Sergeev et al.*, 2011; *Yang et al.*, 2011; *Birn et al.*, 2013]. Thus the classic current wedge seen at midlatitudes is the net current of two-loop SCW. However, the global magnetic perturbations can be represented by classic SCW very well [*Chu et al.*, 2015c]. In addition, according to

Faraday's law, the accumulation of the magnetic flux enclosed between two-loop SCW equals to that of the net current, which is contributed from earthward flows. Therefore, our conclusion that magnetic flux accumulation generated a global SCW is consistent with both classic SCW and two-loop SCW.

The magnetic flux accumulation is the result of imbalance between dayside and nightside magnetic reconnections. During quiet times or steady magnetospheric convection, dayside and nightside reconnection are balanced and magnetic flux is not accumulated in the near-Earth region. During the substorm expansion phase, however, magnetic reconnection in the mid-tail released more magnetic flux in a short time than could be balanced by magnetospheric convection. Note that not only lobe reconnection, but also plasma sheet reconnection could create earthward flows and trigger small substorms [*Chu et al.*, 2010b; *Pu et al.*, 2010b] and generate plasmoids [*Li et al.*, 2013]. The flux carried by earthward flows is accumulated in the near-Earth region that bends the magnetic field lines and generates the FACs of the SCW [*Kepko et al.*, 2014]. The magnetospheric convection is enhanced during such a process. Later the accumulated flux slowly decays (in tens of minutes), and the strength of the SCW decays as well. This is why Φ_{SCW} and Φ_{aurora} were close to Φ_{flows} at first, and became smaller later.

6.4.2 Modeling magnetic field rotation

The accumulated magnetic flux not only dipolarized the magnetic field lines vertically, but also bent them azimuthally. The magnetic dipolarization was mainly caused by the reduction of the cross-tail current (tail part of the SCW); the azimuthal

distortion of the magnetic field was related to the FACs of the SCW. The quiet-time (green) and the substorm-time (black) magnetic field lines in the meridian and equatorial planes are compared in Figure 6.8. The quiet time magnetic field lines were calculated using Tsyganenko model; the substorm-time magnetic field lines were calculated using the dynamic magnetospheric model, which took the SCW at 02:50 UT into account. In the meridian plane (Figure 6.8a), the magnetic field lines are traced from the same equatorial footprint. The projections of the downward (blue) and upward (red) FACs were shown as lines with arrows. The substorm-time magnetic field line (black) from the dynamic magnetospheric model was dipolarized. As predicted by the dynamic magnetospheric model [*Chu et al.*, 2015c], geosynchronous dipolarization at GOES 10 lasted for more than 40 minutes. Its effect on mapping and auroral poleward expansion was discussed in our previous paper [*Chu et al.*, 2015c]. Here this study focuses on projection of field lines on the equatorial plane. The colored contour in Figure 6.8b shows the magnetic perturbation ΔBz induced by the SCW on the equatorial plane. The sheet-like upward FAC (from the ionosphere) is represented by the area between two dashed red lines with outward arrows; the downward FAC (into the ionosphere) is located between two dashed blue lines. The downward FAC is wider than the upward FAC in an asymmetric SCW; thus, ΔBz is stronger near the upward FAC. The magnetic field lines were traced from the same ionospheric footprints using the Tsyganenko model (green) and dynamic magnetospheric model (black). Near the central meridian of the SCW, the substorm-time magnetic field line (#4, green) was not as azimuthally bent as the quiet-

time field line (#4, black). In addition, the equatorial footprint of the substorm-time field line (#4, green) was closer to the Earth because it was highly dipolarized. Near the upward FAC (inside the SCW at earlier local time), the substorm-time magnetic field line (#3, black) was bent more significantly toward dusk than the quiet time field line (#3, green). In addition, its equatorial footprint (#3, black) was closer to the Earth than the quiet-time magnetic field line (#3, green) because of the dipolarization. On the other hand, the magnetic field lines (#1 and #2) were barely bent azimuthally because they were outside the SCW. And their equatorial footprints (#1 and #2) were farther from the Earth, suggesting that the magnetic field lines outside the SCW were stretched rather than dipolarized. Near the downward FAC, the substorm-time field line (#5, black) was similarly dipolarized but bent dawnward. On the dawnside of the SCW, the magnetic field lines (#6) was stretched but not bent significantly. It should be emphasized that the field line bending shown is calculated using the modeled field and not distorted for purposes of illustration. The modeled vertical dipolarization and azimuthal bending of the magnetic field lines inside the SCW are consistent with previous suggestions that flow braking and diversion can bend magnetic field lines and generate FACs [*Birn and Hesse*, 2014; *Kepko et al.*, 2014].

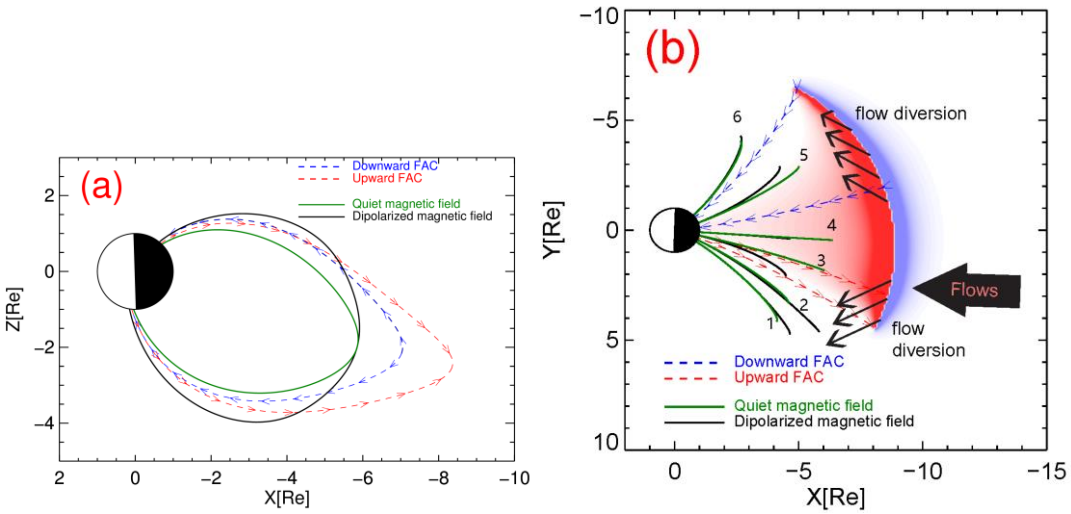

Figure 6.8. Comparison between the magnetic field lines during quiet time (green, before the substorm onset) and during substorm (black, at 02:50 UT) in the meridian (a) and equatorial (b) plane. The downward (blue) and upward (red) FACs of the SCW are illustrated by arrow lines. The colored contour (Figure 6.8b) illustrates the magnetic perturbation ΔBz by the SCW at 02:50 UT.

6.5 Conclusions

THEMIS observations of an isolated substorm on 13 February 2008 reveal a magnetic flux transport and accumulation process that is closely related to SCW generation. A tailward plasmoid was observed by P1 at X=27 R_E in the form of travelling compression region, which was the evidence of mid-tail reconnection. Successive earthward flows from the reconnection were observed at P3 and P4 at X=~10 R_E; the first flow was associated with auroral onset. Magnetic flux released by magnetic reconnection partly transported by earthward flows and accumulated in the near-Earth region, and partly

diverted by azimuthal flow. The amount of magnetic flux during transport and accumulation was carefully examined in the local time corresponding to the auroral brightening region. The amount of flux transported by the flows (Φ_{flows}) was consistent with the amount of magnetic flux accumulated in the SCW-induced dipolarization (Φ_{SCW}). This agreement suggests that accumulated flux from the flows was responsible for generation of the SCW. The first flow carried enough magnetic flux for a global SCW, and successive flows further contributed to the global SCW by accumulating more magnetic flux. The accumulated flux dipolarized the modeled magnetic field lines vertically and bent them azimuthally in the region of the SCW. This is consistent with previous suggestions that flow braking and diversion can bend magnetic field lines and generate FACs. The accumulated flux was also consistent with the amount of magnetic flux responsible for auroral poleward expansion (Φ_{aurora}), suggesting that the accumulated flux caused the auroral poleward expansion by mapping the flows toward higher latitude in the ionosphere via dipolarized magnetic field lines. The tens-of-minutes timescale of the substorm-related phenomena (SCW, magnetic dipolarization, auroral expansion and westward electrojet) is consistent with the flux accumulation process. The quantity of accumulated flux appears to be positively correlated with the amplitudes of these substorm phenomena.

CHAPTER 7

Conclusions and future work

7.1 Conclusions

Substorm current wedge, a core element of substorm dynamics coupling global phenomena in the magnetotail and the ionosphere, is crucial in understanding of substorms. The generation mechanisms of FACs in a SCW have been suggested in theoretical studies: pressure gradient, flow vortex and inertial current. In previous studies, our understanding of the generation mechanisms were based predominately on numerical simulations. The inertial current has been investigated using observations from single satellite. However, there are few observational studies on pressure gradient and flow vortices because multiple suitably-separated satellites are required to obtain them. Moreover, to explain the observed pressure gradient and flow vortices, the central meridian of the SCW is crucial but unknown. In this thesis, an inversion technique for SCW has been developed to obtain the location information, which facilitates to obtain the patterns of the generation mechanisms in the SCW frame. This thesis suggests that the high pressure region generated by flow braking is likely sustaining the FACs in a SCW. The non-alignment between pressure gradient and flux tube volume is consistent with a quadrupole SCW, whose net current is positively correlated with the amount of magnetic flux brought by the flow.

7.1.1 Solar cycle dependence of substorm occurrence and duration

In Chapter 2, an MPB index has been developed to measure the SCW strength based on the MPB signature at midlatitudes at one minute resolution from 1982 to 2012 (31 years). A database of substorm onset was then identified using the MPB index and refined by original magnetic field data. In total, 40,562 substorm onsets are found between 1982 and 2012. The MPB substorm onset list exhibits very good correlations with auroral onsets (0.4 ± 1.9 min) from IMAGE spacecraft and AL onsets (-0.8 ± 5.0 min).

Using the substorm list, I have examined the seasonal and diurnal variations of the substorms. By fitting the seasonal-diurnal occurrence of substorm onsets with Svalgaard function, I found that the substorm occurrence could partially be explained by the equinoctial effect (62%); the residual shows excess signal in the European sector and no clear pattern characteristic of the Russell-McPherron effect.

The solar cycle dependence of substorm occurrence and duration are also investigated. I found that both the substorm occurrence and substorm waiting time showed strong dependence on solar wind speed rather than the sun spot number. Therefore, the geomagnetic activity is controlled by solar wind driving rather than dayside ionospheric conductance. On the other hand, I found that the durations of substorm expansion and recovery phases show rather stochastic stable distribution versus solar wind condition, solar cycle and substorm size. Therefore, it suggests that the generation and decay of the SCW, which is related to the pileup and decay of magnetic flux at the inner edge of the plasma sheet, has an intrinsic pattern independent of external driving. This result has not

been resolved from the AL index because it responses to both the SCW and two-cell convection, and the latter is directly driven by the solar wind.

7.1.2 Inversion technique for substorm current wedge

In Chapter 3, I have developed an inversion technique to determine the parameters of the SCW, such as the strengths and locations of the downward and upward FACs in the SCW, the partial ring current and the ring current. The inversion technique uses magnetic field data from magnetometers at midlatitudes. I have applied the inversion technique for an isolated substorm on January 11th 2002. To validate the inversion results, I have compared the locations of the FACs with auroral observations from IMAGE satellite. I found that the FAC locations given by the inversion technique are consistent with auroral observations in different spectral bands measuring aurora excited by different precipitations. The upward FACs was co-located with the brightest spot of the westward travelling surge measured by wide-band aurora or electron aurora throughout the substorm. The proton aurora near the upward FAC was weak because the proton precipitation related to upward FAC was weak. I also found that the downward FAC was found in good agreement with eastward expansion of the aurora during substorm expansion phase. The agreement is especially good between the proton aurora and downward FAC, because the precipitating protons carries the downward FAC.

The strengths of these currents are validated using various measurements. The SCW strength from the inversion technique was compared with the strength of the westward electrojet obtained from 1-D equivalent ionospheric current. The correlation

coefficient was as high as 95.4%, which suggests that the inversion technique gave reliable SCW intensity. The intensity of the ring current was compared with the SMR index from SuperMAG. The correlation coefficient was 95.2%, suggesting the inversion technique gave reliable ring current strength. In conclusion, the inversion technique for SCW provides a valuable tool for the study of substorm development and its relation to phenomena in space.

7.1.3 Improving mapping earthward flows to auroral poleward expansion

In Chapter 4, I have studied the connections between the earthward flows and the auroral poleward expansion. In an isolated substorm on 13 February 2008, a good correlation was found between four auroral brightenings and four flow breakings and diversions observed by THEMIS P3 and P4, suggesting that the onset location was near the probes' location at |X| = ~ 9 Re. In other words, successive flow breakings and diversions in this location contributed to the generation of auroral brightenings, slight auroral poleward expansions, and the global SCW. The flows and the aurora are connected via FACs flowing along magnetic field lines. The magnetic field lines are usually calculated using standard Tsyganenko model, in which the magnetic dipolarization induced by the SCW is missing.

A dynamic magnetospheric model was developed to provide improved mapping during substorms by superimposing the currents in the inversion model on the Tsyganenko model. The parameters of these currents are provided by the inversion technique for SCW every minute and validated by comparing the model and observed

geosynchronous dipolarization at GOES 10. It was found that the geosynchronous prolonged dipolarization was well predicted by the inversion technique, suggesting that the overall longitudinal structure of the net FACs averaged over latitude resembles the classic SCW. The footprints of the flows from the dynamic magnetospheric model were colocated with auroral brightenings. The footprints followed the auroral poleward expansion during the expansion phase and equatorward retreat during the recovery phase. These evidences above suggests that the auroral poleward expansion and equatorward retreat were mainly caused by the magnetic dipolarization of the global SCW. Although minimal in this event, the effect of the tailward expanding flux pileup region could not be excluded.

7.1.4 Generation mechanisms of substorm current wedge

In chapter 5, the generation mechanisms of the SCW have been investigated in the SCW frame using a statistical analysis of earthward flows and substorm onsets. A total of 3370 earthward flows were observed by THEMIS P3, P4 and P5 during five tail seasons within 12 R_E, where the flow speed significantly dropped and considered to be the flow braking region. Good temporal and spatial correlations between these flows and the substorm onsets. In the time delay analysis, it is found that the flow occurrence peaked at substorm. This good temporal correlation suggests that the SCW formation is highly correlated to the flow braking process. Furthermore, the flow occurrence in the SCW frame relative to the central meridian of the SCW was investigated. It is found that majority (85%) of the flows associated with substorm onsets were located inside the

SCW between two FACs. The good spatial correlation suggests that the FACs are generated on each side of the flows. Then, I plotted the SPEA of the thermal pressure and the flow vortices relative to the flow onsets. In the SPEA, the equatorial thermal pressure lasted for about an hour, which is comparable to the durations of the SCW and has a similar trend to the SCW. On the other hand, the flows associated with flow vortices lasted for less than 3 minutes, which was significantly shorter than the SCW. Therefore, the SCW is likely sustained by the high pressure generated in the flow braking process rather than the transient flow vortices.

The pressure gradient is then studied in the SCW frame. I selected substorm events when three THEMIS probes were located in a triangular configuration on the equatorial plane and located close enough. The pressure gradient was calculated under the assumption that the pressure gradient is linear. I plotted the pressure gradient relative to the central meridian of the SCW. It was found that the ∇P_x increased for almost all substorms; the ∇P_y increased on the dawnside of the central meridian and decreased on the duskside. This result suggests that the center of the high pressure region caused by flow braking was co-located with the central meridian of the SCW, which was consistent with the result that the FACs were generated on each side of the flows. Although the gradient of the flux tube volume cannot be obtained from in situ observations, it can be inferred from the magnetic dipolarization of B_Z. In the SPEA of B_Z, it was found that the center of the magnetic dipolarization B_Z was more tailward than the center of the increased pressure, which was consistent with previous simulation results. Thus, the nonalignment between the gradient of the flux tube volume and pressure could generate

an SCW with quadrupole FACs. Their combined magnetic effects on the ground and at geosynchronous orbit are similar to their net current, which is a classic one-loop SCW.

7.1.5 Magnetic flux accumulation leading to substorm current wedge

In Chapter 5, it is found that the pressure gradient is likely the major contributor to the SCW formation. However, what determines the strength of the SCW is still unknown. In Chapter 6, we analyzed magnetic flux transport and accumulation by earthward flows, which is closely related to SCW formation. We calculated the temporal variation of magnetic flux released by reconnection and transported by earthward flows during the isolated substorm on 13 February 2008 studied in Chapter 4.

At substorm onset, a tailward plasmoid was observed by THEMIS P1 at X=27 R_E in the form of travelling compression region, which was the evidence of mid-tail reconnection. The lobe magnetic flux released by the reconnection was calculated. In the near-Earth region, successive earthward flows from the reconnection were observed at substorm onset by THEMIS P3 and P4 at X=~10 R_E. The first flow was associated with auroral onset. I have carefully examined the amount of magnetic flux during transport and accumulation in the local time corresponding to the auroral brightening region. I found that the amount of flux transported by the flows (Φ_{flows}) was consistent with the amount of magnetic flux accumulated in the SCW-induced dipolarization (Φ_{SCW}). This agreement suggests that accumulated flux from the flows was responsible for generation of the SCW. In addition, I found that the first flow carried enough magnetic flux for a global SCW for early expansion phase, and successive flows further contributed to the

global SCW by accumulating more magnetic flux. I also found that the accumulated flux was consistent with the amount of magnetic flux responsible for auroral poleward expansion (Φ_{aurora}), suggesting that the accumulated flux caused the auroral poleward expansion by mapping the flows toward higher latitude in the ionosphere via dipolarized magnetic field lines. I have modeled how the magnetic field lines were re-configured by the existence of an SCW. It was found that the SCW or the accumulated flux dipolarized the modeled magnetic field lines vertically and bent them azimuthally inside the SCW. This is consistent with previous suggestions that flow braking and diversion can bend magnetic field lines and generate FACs. The quantity of accumulated flux appears to be positively correlated with the amplitudes of these substorm phenomena.

7.2 Future Work

This thesis set stages for many future studies. As demonstrated in this thesis and previous studies, substorm current wedge formation is associated with the flow braking and diversion process. However, flows occur at any level of geomagnetic activity and only a small fraction of flows can trigger a substorm. Some flows only trigger a pseudo breakup instead of a major substorm. Although the penetration depth of an earthward flow is generally thought to depend on its entropy, what controls whether an earthward flow can trigger a substorm is still unknown. Our expected parameter is the magnetic flux transport by an earthward flow and accumulated at the inner edge of the plasma sheet. Based on the database of earthward flows and substorms in this thesis, we propose to study the amount of magnetic flux carried by flows associated and not associated with

substorm onsets. It is expected that the amount of magnetic flux carried by two types of flows differs significantly, no matter what radial distance they are observed.

The newly developed MPB index, designed to measure the SCW strength, has raise a lot of interests in our society. It is unique because it is supposed to measure the amplitude of the unloading process in the nightside, while the AL index measures both processes of directly-driven and unloading. Linear prediction filter technique, canonical correlation analysis, and nonlinear autoregressive network with exogenous inputs are proposed to apply to both indices to 1) separate two processes and 2) predict geomagnetic activity using solar wind parameters.

The transport and acceleration of low energy electrons from the plasma sheet to inner magnetosphere with energy from approximately 10 to 250 keV, which is the seed population, is critically important for the radiation belt dynamics. These electrons are generally associated with substorm injections. Satellite measurements cannot provide continuous spatial or temporal measurements of these electrons at all magnetic local time and L-shells. The local time and amplitude of the injections can be obtained from the inversion technique for SCW developed in this thesis. Therefore, the inversion technique can provide useful information of the seed populations in study of the radiation belt dynamics.

APPENDEX 1

JOHN WILEY AND SONS LICENSE TERMS AND CONDITIONS

Nov 24, 2015

This Agreement between Xiangning Chu ("You") and John Wiley and Sons ("John Wiley and Sons") consists of your license details and the terms and conditions provided by John Wiley and Sons and Copyright Clearance Center.

License Number	3755570850951
License date	Nov 24, 2015
Licensed Content Publisher	John Wiley and Sons
Licensed Content Publication	Journal of Geophysical Research: Space Physics
Licensed Content Title	Solar cycle dependence of substorm occurrence and duration: Implications for onset
Licensed Content Author	Xiangning Chu, Robert L. McPherron, Tung-Shin Hsu, Vassilis Angelopoulos
Licensed Content Date	Apr 22, 2015
Pages	11
Type of use	Dissertation/Thesis
Requestor type	Author of this Wiley article
Format	Print and electronic
Portion	Full article
Will you be translating?	No
Title of your thesis /	Configuration and Generation of Substorm Current

dissertation	Wedge
Expected completion date	Dec 2015
Expected size (number of pages)	180
Total	0.00 USD

Terms and Conditions

TERMS AND CONDITIONS

This copyrighted material is owned by or exclusively licensed to John Wiley & Sons, Inc. or one of its group companies (each a"Wiley Company") or handled on behalf of a society with which a Wiley Company has exclusive publishing rights in relation to a particular work (collectively "WILEY"). By clicking "accept" in connection with completing this licensing transaction, you agree that the following terms and conditions apply to this transaction (along with the billing and payment terms and conditions established by the Copyright Clearance Center Inc., ("CCC's Billing and Payment terms and conditions"), at the time that you opened your RightsLink account (these are available at any time at http://myaccount.copyright.com).

Terms and Conditions

- The materials you have requested permission to reproduce or reuse (the "Wiley Materials") are protected by copyright.
- You are hereby granted a personal, non-exclusive, non-sub licensable (on a stand-alone basis), non-transferable, worldwide, limited license to reproduce the Wiley Materials for the purpose specified in the licensing process. This license, **and any CONTENT (PDF or image file) purchased as part of your order,** is for a one-time use only and limited to any maximum distribution number specified in the license. The first instance of republication or reuse granted by this license must be completed within two years of the date of the grant of this license (although copies prepared before the end date may be distributed thereafter). The Wiley Materials shall not be used in any other manner or for any other purpose, beyond what is granted in the license. Permission is granted subject to an appropriate acknowledgement given to the author, title of the material/book/journal and the publisher. You shall also duplicate the copyright notice that appears in the Wiley publication

in your use of the Wiley Material. Permission is also granted on the understanding that nowhere in the text is a previously published source acknowledged for all or part of this Wiley Material. Any third party content is expressly excluded from this permission.

- With respect to the Wiley Materials, all rights are reserved. Except as expressly granted by the terms of the license, no part of the Wiley Materials may be copied, modified, adapted (except for minor reformatting required by the new Publication), translated, reproduced, transferred or distributed, in any form or by any means, and no derivative works may be made based on the Wiley Materials without the prior permission of the respective copyright owner.**For STM Signatory Publishers clearing permission under the terms of the STM Permissions Guidelines only, the terms of the license are extended to include subsequent editions and for editions in other languages, provided such editions are for the work as a whole in situ and does not involve the separate exploitation of the permitted figures or extracts,** You may not alter, remove or suppress in any manner any copyright, trademark or other notices displayed by the Wiley Materials. You may not license, rent, sell, loan, lease, pledge, offer as security, transfer or assign the Wiley Materials on a stand-alone basis, or any of the rights granted to you hereunder to any other person.
- The Wiley Materials and all of the intellectual property rights therein shall at all times remain the exclusive property of John Wiley & Sons Inc, the Wiley Companies, or their respective licensors, and your interest therein is only that of having possession of and the right to reproduce the Wiley Materials pursuant to Section 2 herein during the continuance of this Agreement. You agree that you own no right, title or interest in or to the Wiley Materials or any of the intellectual property rights therein. You shall have no rights hereunder other than the license as provided for above in Section 2. No right, license or interest to any trademark, trade name, service mark or other branding ("Marks") of WILEY or its licensors is granted hereunder, and you agree that you shall not assert any such right, license or interest with respect thereto
- NEITHER WILEY NOR ITS LICENSORS MAKES ANY WARRANTY OR REPRESENTATION OF ANY KIND TO YOU OR ANY THIRD PARTY, EXPRESS, IMPLIED OR STATUTORY, WITH RESPECT TO THE MATERIALS OR THE ACCURACY OF ANY INFORMATION CONTAINED IN THE MATERIALS, INCLUDING, WITHOUT LIMITATION, ANY IMPLIED WARRANTY OF MERCHANTABILITY,

ACCURACY, SATISFACTORY QUALITY, FITNESS FOR A PARTICULAR PURPOSE, USABILITY, INTEGRATION OR NON-INFRINGEMENT AND ALL SUCH WARRANTIES ARE HEREBY EXCLUDED BY WILEY AND ITS LICENSORS AND WAIVED BY YOU.

- WILEY shall have the right to terminate this Agreement immediately upon breach of this Agreement by you.
- You shall indemnify, defend and hold harmless WILEY, its Licensors and their respective directors, officers, agents and employees, from and against any actual or threatened claims, demands, causes of action or proceedings arising from any breach of this Agreement by you.
- IN NO EVENT SHALL WILEY OR ITS LICENSORS BE LIABLE TO YOU OR ANY OTHER PARTY OR ANY OTHER PERSON OR ENTITY FOR ANY SPECIAL, CONSEQUENTIAL, INCIDENTAL, INDIRECT, EXEMPLARY OR PUNITIVE DAMAGES, HOWEVER CAUSED, ARISING OUT OF OR IN CONNECTION WITH THE DOWNLOADING, PROVISIONING, VIEWING OR USE OF THE MATERIALS REGARDLESS OF THE FORM OF ACTION, WHETHER FOR BREACH OF CONTRACT, BREACH OF WARRANTY, TORT, NEGLIGENCE, INFRINGEMENT OR OTHERWISE (INCLUDING, WITHOUT LIMITATION, DAMAGES BASED ON LOSS OF PROFITS, DATA, FILES, USE, BUSINESS OPPORTUNITY OR CLAIMS OF THIRD PARTIES), AND WHETHER OR NOT THE PARTY HAS BEEN ADVISED OF THE POSSIBILITY OF SUCH DAMAGES. THIS LIMITATION SHALL APPLY NOTWITHSTANDING ANY FAILURE OF ESSENTIAL PURPOSE OF ANY LIMITED REMEDY PROVIDED HEREIN.
- Should any provision of this Agreement be held by a court of competent jurisdiction to be illegal, invalid, or unenforceable, that provision shall be deemed amended to achieve as nearly as possible the same economic effect as the original provision, and the legality, validity and enforceability of the remaining provisions of this Agreement shall not be affected or impaired thereby.
- The failure of either party to enforce any term or condition of this Agreement shall not constitute a waiver of either party's right to enforce each and every term and condition of this Agreement. No breach under this agreement shall be deemed waived or excused by either party unless such waiver or consent

is in writing signed by the party granting such waiver or consent. The waiver by or consent of a party to a breach of any provision of this Agreement shall not operate or be construed as a waiver of or consent to any other or subsequent breach by such other party.

- This Agreement may not be assigned (including by operation of law or otherwise) by you without WILEY's prior written consent.
- Any fee required for this permission shall be non-refundable after thirty (30) days from receipt by the CCC.
- These terms and conditions together with CCC's Billing and Payment terms and conditions (which are incorporated herein) form the entire agreement between you and WILEY concerning this licensing transaction and (in the absence of fraud) supersedes all prior agreements and representations of the parties, oral or written. This Agreement may not be amended except in writing signed by both parties. This Agreement shall be binding upon and inure to the benefit of the parties' successors, legal representatives, and authorized assigns.
- In the event of any conflict between your obligations established by these terms and conditions and those established by CCC's Billing and Payment terms and conditions, these terms and conditions shall prevail.
- WILEY expressly reserves all rights not specifically granted in the combination of (i) the license details provided by you and accepted in the course of this licensing transaction, (ii) these terms and conditions and (iii) CCC's Billing and Payment terms and conditions.
- This Agreement will be void if the Type of Use, Format, Circulation, or Requestor Type was misrepresented during the licensing process.
- This Agreement shall be governed by and construed in accordance with the laws of the State of New York, USA, without regards to such state's conflict of law rules. Any legal action, suit or proceeding arising out of or relating to these Terms and Conditions or the breach thereof shall be instituted in a court of competent jurisdiction in New York County in the State of New York in the United States of America and each party hereby consents and submits to the personal jurisdiction of such court, waives any objection to venue in such court and consents to service of process by registered or certified mail, return receipt requested, at the last known address of such party.

WILEY OPEN ACCESS TERMS AND CONDITIONS

Wiley Publishes Open Access Articles in fully Open Access Journals and in Subscription journals offering Online Open. Although most of the fully Open Access journals publish open access articles under the terms of the Creative Commons Attribution (CC BY) License only, the subscription journals and a few of the Open Access Journals offer a choice of Creative Commons Licenses. The license type is clearly identified on the article.

The Creative Commons Attribution License

The Creative Commons Attribution License (CC-BY) allows users to copy, distribute and transmit an article, adapt the article and make commercial use of the article. The CC-BY license permits commercial and non-

Creative Commons Attribution Non-Commercial License

The Creative Commons Attribution Non-Commercial (CC-BY-NC)License permits use, distribution and reproduction in any medium, provided the original work is properly cited and is not used for commercial purposes.(see below)

Creative Commons Attribution-Non-Commercial-NoDerivs License

The Creative Commons Attribution Non-Commercial-NoDerivs License (CC-BY-NC-ND) permits use, distribution and reproduction in any medium, provided the original work is properly cited, is not used for commercial purposes and no modifications or adaptations are made. (see below)

Use by commercial "for-profit" organizations

Use of Wiley Open Access articles for commercial, promotional, or marketing purposes requires further explicit permission from Wiley and will be subject to a fee.

Further details can be found on Wiley Online Library
http://olabout.wiley.com/WileyCDA/Section/id-410895.html

Other Terms and Conditions:

v1.10 Last updated September 2015

Questions? customercare@copyright.com or +1-855-239-3415 (toll free in the US) or +1-978-646-2777.

APPENDEX 2

JOHN WILEY AND SONS LICENSE TERMS AND CONDITIONS

Nov 24, 2015

This Agreement between Xiangning Chu ("You") and John Wiley and Sons ("John Wiley and Sons") consists of your license details and the terms and conditions provided by John Wiley and Sons and Copyright Clearance Center.

License Number	3755580569084
License date	Nov 24, 2015
Licensed Content Publisher	John Wiley and Sons
Licensed Content Publication	Journal of Geophysical Research: Space Physics
Licensed Content Title	Development and validation of inversion technique for substorm current wedge using ground magnetic field data
Licensed Content Author	Xiangning Chu,Tung-Shin Hsu,Robert L. McPherron,Vassilis Angelopoulos,Zuyin Pu,James J. Weygand,Krishan Khurana,Martin Connors,Jennifer Kissinger,Hui Zhang,Olaf Amm
Licensed Content Date	Mar 26, 2014
Pages	16
Type of use	Dissertation/Thesis
Requestor type	Author of this Wiley article
Format	Print and electronic
Portion	Full article
Will you be translating?	No
Title of your thesis / dissertation	Configuration and Generation of Substorm Current Wedge
Expected completion date	Dec 2015
Expected size (number of pages)	180
Total	0.00 USD
Terms and Conditions	

TERMS AND CONDITIONS

This copyrighted material is owned by or exclusively licensed to John Wiley & Sons, Inc. or one of its group companies (each a"Wiley Company") or handled on behalf of a

society with which a Wiley Company has exclusive publishing rights in relation to a particular work (collectively "WILEY"). By clicking "accept" in connection with completing this licensing transaction, you agree that the following terms and conditions apply to this transaction (along with the billing and payment terms and conditions established by the Copyright Clearance Center Inc., ("CCC's Billing and Payment terms and conditions"), at the time that you opened your RightsLink account (these are available at any time at http://myaccount.copyright.com).

Terms and Conditions

- The materials you have requested permission to reproduce or reuse (the "Wiley Materials") are protected by copyright.

- You are hereby granted a personal, non-exclusive, non-sub licensable (on a stand-alone basis), non-transferable, worldwide, limited license to reproduce the Wiley Materials for the purpose specified in the licensing process. This license, **and any CONTENT (PDF or image file) purchased as part of your order,** is for a one-time use only and limited to any maximum distribution number specified in the license. The first instance of republication or reuse granted by this license must be completed within two years of the date of the grant of this license (although copies prepared before the end date may be distributed thereafter). The Wiley Materials shall not be used in any other manner or for any other purpose, beyond what is granted in the license. Permission is granted subject to an appropriate acknowledgement given to the author, title of the material/book/journal and the publisher. You shall also duplicate the copyright notice that appears in the Wiley publication in your use of the Wiley Material. Permission is also granted on the understanding that nowhere in the text is a previously published source acknowledged for all or part of this Wiley Material. Any third party content is expressly excluded from this permission.

- With respect to the Wiley Materials, all rights are reserved. Except as expressly granted by the terms of the license, no part of the Wiley Materials may be copied, modified, adapted (except for minor reformatting required by the new Publication), translated, reproduced, transferred or distributed, in any form or by any means, and no derivative works may be made based on the Wiley Materials without the prior permission of the respective copyright owner.**For STM Signatory Publishers clearing permission under the terms of the STM Permissions Guidelines only, the terms of the license are extended to include subsequent editions and for editions in other languages, provided such editions are for the work as a whole in situ and does not involve the separate exploitation of the permitted figures or extracts,** You may not alter, remove or suppress in any manner any copyright, trademark or other notices displayed by

the Wiley Materials. You may not license, rent, sell, loan, lease, pledge, offer as security, transfer or assign the Wiley Materials on a stand-alone basis, or any of the rights granted to you hereunder to any other person.

- The Wiley Materials and all of the intellectual property rights therein shall at all times remain the exclusive property of John Wiley & Sons Inc, the Wiley Companies, or their respective licensors, and your interest therein is only that of having possession of and the right to reproduce the Wiley Materials pursuant to Section 2 herein during the continuance of this Agreement. You agree that you own no right, title or interest in or to the Wiley Materials or any of the intellectual property rights therein. You shall have no rights hereunder other than the license as provided for above in Section 2. No right, license or interest to any trademark, trade name, service mark or other branding ("Marks") of WILEY or its licensors is granted hereunder, and you agree that you shall not assert any such right, license or interest with respect thereto

- NEITHER WILEY NOR ITS LICENSORS MAKES ANY WARRANTY OR REPRESENTATION OF ANY KIND TO YOU OR ANY THIRD PARTY, EXPRESS, IMPLIED OR STATUTORY, WITH RESPECT TO THE MATERIALS OR THE ACCURACY OF ANY INFORMATION CONTAINED IN THE MATERIALS, INCLUDING, WITHOUT LIMITATION, ANY IMPLIED WARRANTY OF MERCHANTABILITY, ACCURACY, SATISFACTORY QUALITY, FITNESS FOR A PARTICULAR PURPOSE, USABILITY, INTEGRATION OR NON-INFRINGEMENT AND ALL SUCH WARRANTIES ARE HEREBY EXCLUDED BY WILEY AND ITS LICENSORS AND WAIVED BY YOU.

- WILEY shall have the right to terminate this Agreement immediately upon breach of this Agreement by you.

- You shall indemnify, defend and hold harmless WILEY, its Licensors and their respective directors, officers, agents and employees, from and against any actual or threatened claims, demands, causes of action or proceedings arising from any breach of this Agreement by you.

- IN NO EVENT SHALL WILEY OR ITS LICENSORS BE LIABLE TO YOU OR ANY OTHER PARTY OR ANY OTHER PERSON OR ENTITY FOR ANY SPECIAL, CONSEQUENTIAL, INCIDENTAL, INDIRECT, EXEMPLARY OR PUNITIVE DAMAGES, HOWEVER CAUSED, ARISING OUT OF OR IN CONNECTION WITH THE DOWNLOADING, PROVISIONING, VIEWING OR USE OF THE MATERIALS REGARDLESS OF THE FORM OF ACTION, WHETHER FOR BREACH OF CONTRACT, BREACH OF WARRANTY, TORT, NEGLIGENCE, INFRINGEMENT OR OTHERWISE (INCLUDING, WITHOUT LIMITATION, DAMAGES BASED ON LOSS OF PROFITS,

DATA, FILES, USE, BUSINESS OPPORTUNITY OR CLAIMS OF THIRD PARTIES), AND WHETHER OR NOT THE PARTY HAS BEEN ADVISED OF THE POSSIBILITY OF SUCH DAMAGES. THIS LIMITATION SHALL APPLY NOTWITHSTANDING ANY FAILURE OF ESSENTIAL PURPOSE OF ANY LIMITED REMEDY PROVIDED HEREIN.

- Should any provision of this Agreement be held by a court of competent jurisdiction to be illegal, invalid, or unenforceable, that provision shall be deemed amended to achieve as nearly as possible the same economic effect as the original provision, and the legality, validity and enforceability of the remaining provisions of this Agreement shall not be affected or impaired thereby.

- The failure of either party to enforce any term or condition of this Agreement shall not constitute a waiver of either party's right to enforce each and every term and condition of this Agreement. No breach under this agreement shall be deemed waived or excused by either party unless such waiver or consent is in writing signed by the party granting such waiver or consent. The waiver by or consent of a party to a breach of any provision of this Agreement shall not operate or be construed as a waiver of or consent to any other or subsequent breach by such other party.

- This Agreement may not be assigned (including by operation of law or otherwise) by you without WILEY's prior written consent.

- Any fee required for this permission shall be non-refundable after thirty (30) days from receipt by the CCC.

- These terms and conditions together with CCC's Billing and Payment terms and conditions (which are incorporated herein) form the entire agreement between you and WILEY concerning this licensing transaction and (in the absence of fraud) supersedes all prior agreements and representations of the parties, oral or written. This Agreement may not be amended except in writing signed by both parties. This Agreement shall be binding upon and inure to the benefit of the parties' successors, legal representatives, and authorized assigns.

- In the event of any conflict between your obligations established by these terms and conditions and those established by CCC's Billing and Payment terms and conditions, these terms and conditions shall prevail.

- WILEY expressly reserves all rights not specifically granted in the combination of (i) the license details provided by you and accepted in the course of this licensing transaction, (ii) these terms and conditions and (iii) CCC's Billing and Payment terms and conditions.

- This Agreement will be void if the Type of Use, Format, Circulation, or Requestor Type was misrepresented during the licensing process.

- This Agreement shall be governed by and construed in accordance with the laws of the State of New York, USA, without regards to such state's conflict of law rules. Any legal action, suit or proceeding arising out of or relating to these Terms and Conditions or the breach thereof shall be instituted in a court of competent jurisdiction in New York County in the State of New York in the United States of America and each party hereby consents and submits to the personal jurisdiction of such court, waives any objection to venue in such court and consents to service of process by registered or certified mail, return receipt requested, at the last known address of such party.

WILEY OPEN ACCESS TERMS AND CONDITIONS

Wiley Publishes Open Access Articles in fully Open Access Journals and in Subscription journals offering Online Open. Although most of the fully Open Access journals publish open access articles under the terms of the Creative Commons Attribution (CC BY) License only, the subscription journals and a few of the Open Access Journals offer a choice of Creative Commons Licenses. The license type is clearly identified on the article.

The Creative Commons Attribution License

The Creative Commons Attribution License (CC-BY) allows users to copy, distribute and transmit an article, adapt the article and make commercial use of the article. The CC-BY license permits commercial and non-

Creative Commons Attribution Non-Commercial License

The Creative Commons Attribution Non-Commercial (CC-BY-NC)License permits use, distribution and reproduction in any medium, provided the original work is properly cited and is not used for commercial purposes.(see below)

Creative Commons Attribution-Non-Commercial-NoDerivs License

The Creative Commons Attribution Non-Commercial-NoDerivs License (CC-BY-NC-ND) permits use, distribution and reproduction in any medium, provided the original work is properly cited, is not used for commercial purposes and no modifications or adaptations are made. (see below)

Use by commercial "for-profit" organizations

Use of Wiley Open Access articles for commercial, promotional, or marketing purposes requires further explicit permission from Wiley and will be subject to a fee.

Further details can be found on Wiley Online Library
http://olabout.wiley.com/WileyCDA/Section/id-410895.html

Other Terms and Conditions:

v1.10 Last updated September 2015

Questions? customercare@copyright.com or +1-855-239-3415 (toll free in the US) or +1-978-646-2777.

APPENDEX 3

JOHN WILEY AND SONS LICENSE
TERMS AND CONDITIONS

Nov 24, 2015

This Agreement between Xiangning Chu ("You") and John Wiley and Sons ("John Wiley and Sons") consists of your license details and the terms and conditions provided by John Wiley and Sons and Copyright Clearance Center.

License Number	3755580353588
License date	Nov 24, 2015
Licensed Content Publisher	John Wiley and Sons
Licensed Content Publication	Journal of Geophysical Research: Space Physics
Licensed Content Title	Magnetic mapping effects of substorm currents leading to auroral poleward expansion and equatorward retreat
Licensed Content Author	Xiangning Chu,Robert L. McPherron,Tung-Shin Hsu,Vassilis Angelopoulos,Zuyin Pu,Zhonghua Yao,Hui Zhang,Martin Connors
Licensed Content Date	Jan 19, 2015
Pages	13
Type of use	Dissertation/Thesis
Requestor type	Author of this Wiley article
Format	Print and electronic
Portion	Full article
Will you be translating?	No
Title of your thesis / dissertation	Configuration and Generation of Substorm Current Wedge
Expected completion date	Dec 2015
Expected size (number of pages)	180
Total	0.00 USD
Terms and Conditions	

TERMS AND CONDITIONS

This copyrighted material is owned by or exclusively licensed to John Wiley & Sons, Inc. or one of its group companies (each a"Wiley Company") or handled on behalf of a society with which a Wiley Company has exclusive publishing rights in relation to a

particular work (collectively "WILEY"). By clicking "accept" in connection with completing this licensing transaction, you agree that the following terms and conditions apply to this transaction (along with the billing and payment terms and conditions established by the Copyright Clearance Center Inc., ("CCC's Billing and Payment terms and conditions"), at the time that you opened your RightsLink account (these are available at any time at http://myaccount.copyright.com).

Terms and Conditions

- The materials you have requested permission to reproduce or reuse (the "Wiley Materials") are protected by copyright.

- You are hereby granted a personal, non-exclusive, non-sub licensable (on a stand-alone basis), non-transferable, worldwide, limited license to reproduce the Wiley Materials for the purpose specified in the licensing process. This license, **and any CONTENT (PDF or image file) purchased as part of your order,** is for a one-time use only and limited to any maximum distribution number specified in the license. The first instance of republication or reuse granted by this license must be completed within two years of the date of the grant of this license (although copies prepared before the end date may be distributed thereafter). The Wiley Materials shall not be used in any other manner or for any other purpose, beyond what is granted in the license. Permission is granted subject to an appropriate acknowledgement given to the author, title of the material/book/journal and the publisher. You shall also duplicate the copyright notice that appears in the Wiley publication in your use of the Wiley Material. Permission is also granted on the understanding that nowhere in the text is a previously published source acknowledged for all or part of this Wiley Material. Any third party content is expressly excluded from this permission.

- With respect to the Wiley Materials, all rights are reserved. Except as expressly granted by the terms of the license, no part of the Wiley Materials may be copied, modified, adapted (except for minor reformatting required by the new Publication), translated, reproduced, transferred or distributed, in any form or by any means, and no derivative works may be made based on the Wiley Materials without the prior permission of the respective copyright owner.**For STM Signatory Publishers clearing permission under the terms of the STM Permissions Guidelines only, the terms of the license are extended to include subsequent editions and for editions in other languages, provided such editions are for the work as a whole in situ and does not involve the separate exploitation of the permitted figures or extracts,** You may not alter, remove or suppress in any manner any copyright, trademark or other notices displayed by the Wiley Materials. You may not license, rent, sell, loan, lease, pledge, offer as

security, transfer or assign the Wiley Materials on a stand-alone basis, or any of the rights granted to you hereunder to any other person.

- The Wiley Materials and all of the intellectual property rights therein shall at all times remain the exclusive property of John Wiley & Sons Inc, the Wiley Companies, or their respective licensors, and your interest therein is only that of having possession of and the right to reproduce the Wiley Materials pursuant to Section 2 herein during the continuance of this Agreement. You agree that you own no right, title or interest in or to the Wiley Materials or any of the intellectual property rights therein. You shall have no rights hereunder other than the license as provided for above in Section 2. No right, license or interest to any trademark, trade name, service mark or other branding ("Marks") of WILEY or its licensors is granted hereunder, and you agree that you shall not assert any such right, license or interest with respect thereto

- NEITHER WILEY NOR ITS LICENSORS MAKES ANY WARRANTY OR REPRESENTATION OF ANY KIND TO YOU OR ANY THIRD PARTY, EXPRESS, IMPLIED OR STATUTORY, WITH RESPECT TO THE MATERIALS OR THE ACCURACY OF ANY INFORMATION CONTAINED IN THE MATERIALS, INCLUDING, WITHOUT LIMITATION, ANY IMPLIED WARRANTY OF MERCHANTABILITY, ACCURACY, SATISFACTORY QUALITY, FITNESS FOR A PARTICULAR PURPOSE, USABILITY, INTEGRATION OR NON-INFRINGEMENT AND ALL SUCH WARRANTIES ARE HEREBY EXCLUDED BY WILEY AND ITS LICENSORS AND WAIVED BY YOU.

- WILEY shall have the right to terminate this Agreement immediately upon breach of this Agreement by you.

- You shall indemnify, defend and hold harmless WILEY, its Licensors and their respective directors, officers, agents and employees, from and against any actual or threatened claims, demands, causes of action or proceedings arising from any breach of this Agreement by you.

- IN NO EVENT SHALL WILEY OR ITS LICENSORS BE LIABLE TO YOU OR ANY OTHER PARTY OR ANY OTHER PERSON OR ENTITY FOR ANY SPECIAL, CONSEQUENTIAL, INCIDENTAL, INDIRECT, EXEMPLARY OR PUNITIVE DAMAGES, HOWEVER CAUSED, ARISING OUT OF OR IN CONNECTION WITH THE DOWNLOADING, PROVISIONING, VIEWING OR USE OF THE MATERIALS REGARDLESS OF THE FORM OF ACTION, WHETHER FOR BREACH OF CONTRACT, BREACH OF WARRANTY, TORT, NEGLIGENCE, INFRINGEMENT OR OTHERWISE (INCLUDING, WITHOUT LIMITATION, DAMAGES BASED ON LOSS OF PROFITS, DATA, FILES, USE, BUSINESS OPPORTUNITY OR CLAIMS OF THIRD

PARTIES), AND WHETHER OR NOT THE PARTY HAS BEEN ADVISED OF THE POSSIBILITY OF SUCH DAMAGES. THIS LIMITATION SHALL APPLY NOTWITHSTANDING ANY FAILURE OF ESSENTIAL PURPOSE OF ANY LIMITED REMEDY PROVIDED HEREIN.

- Should any provision of this Agreement be held by a court of competent jurisdiction to be illegal, invalid, or unenforceable, that provision shall be deemed amended to achieve as nearly as possible the same economic effect as the original provision, and the legality, validity and enforceability of the remaining provisions of this Agreement shall not be affected or impaired thereby.

- The failure of either party to enforce any term or condition of this Agreement shall not constitute a waiver of either party's right to enforce each and every term and condition of this Agreement. No breach under this agreement shall be deemed waived or excused by either party unless such waiver or consent is in writing signed by the party granting such waiver or consent. The waiver by or consent of a party to a breach of any provision of this Agreement shall not operate or be construed as a waiver of or consent to any other or subsequent breach by such other party.

- This Agreement may not be assigned (including by operation of law or otherwise) by you without WILEY's prior written consent.

- Any fee required for this permission shall be non-refundable after thirty (30) days from receipt by the CCC.

- These terms and conditions together with CCC's Billing and Payment terms and conditions (which are incorporated herein) form the entire agreement between you and WILEY concerning this licensing transaction and (in the absence of fraud) supersedes all prior agreements and representations of the parties, oral or written. This Agreement may not be amended except in writing signed by both parties. This Agreement shall be binding upon and inure to the benefit of the parties' successors, legal representatives, and authorized assigns.

- In the event of any conflict between your obligations established by these terms and conditions and those established by CCC's Billing and Payment terms and conditions, these terms and conditions shall prevail.

- WILEY expressly reserves all rights not specifically granted in the combination of (i) the license details provided by you and accepted in the course of this licensing transaction, (ii) these terms and conditions and (iii) CCC's Billing and Payment terms and conditions.

- This Agreement will be void if the Type of Use, Format, Circulation, or

Requestor Type was misrepresented during the licensing process.

- This Agreement shall be governed by and construed in accordance with the laws of the State of New York, USA, without regards to such state's conflict of law rules. Any legal action, suit or proceeding arising out of or relating to these Terms and Conditions or the breach thereof shall be instituted in a court of competent jurisdiction in New York County in the State of New York in the United States of America and each party hereby consents and submits to the personal jurisdiction of such court, waives any objection to venue in such court and consents to service of process by registered or certified mail, return receipt requested, at the last known address of such party.

WILEY OPEN ACCESS TERMS AND CONDITIONS

Wiley Publishes Open Access Articles in fully Open Access Journals and in Subscription journals offering Online Open. Although most of the fully Open Access journals publish open access articles under the terms of the Creative Commons Attribution (CC BY) License only, the subscription journals and a few of the Open Access Journals offer a choice of Creative Commons Licenses. The license type is clearly identified on the article.

The Creative Commons Attribution License

The Creative Commons Attribution License (CC-BY) allows users to copy, distribute and transmit an article, adapt the article and make commercial use of the article. The CC-BY license permits commercial and non-

Creative Commons Attribution Non-Commercial License

The Creative Commons Attribution Non-Commercial (CC-BY-NC)License permits use, distribution and reproduction in any medium, provided the original work is properly cited and is not used for commercial purposes.(see below)

Creative Commons Attribution-Non-Commercial-NoDerivs License

The Creative Commons Attribution Non-Commercial-NoDerivs License (CC-BY-NC-ND) permits use, distribution and reproduction in any medium, provided the original work is properly cited, is not used for commercial purposes and no modifications or adaptations are made. (see below)

Use by commercial "for-profit" organizations

Use of Wiley Open Access articles for commercial, promotional, or marketing purposes

requires further explicit permission from Wiley and will be subject to a fee.

Further details can be found on Wiley Online Library
http://olabout.wiley.com/WileyCDA/Section/id-410895.html

Other Terms and Conditions:

v1.10 Last updated September 2015
Questions? customercare@copyright.com or +1-855-239-3415 (toll free in the US) or +1-978-646-2777.

BIBLIOGRAPHY

1. Akasofu, S. I. (1964), The Development of the Auroral Substorm, *Planetary and Space Science*, *12*(4), 273-282, doi:10.1016/0032-0633(64)90151-5.

2. Akasofu, S. I. (1968), Polar and magnetosphere substorms.

3. Akasofu, S. I. (1996), Search for the "unknown" quantity in the solar wind: A personal account, *J. Geophys. Res.*, *101*(A5), 10531-10540, doi:10.1029/96ja00182.

4. Akasofu, S. I., and S. Chapman (1961), Ring Current, Geomagnetic Disturbance, and Van Allen Radiation Belts, *J. Geophys. Res.*, *66*(5), 1321-&, doi:10.1029/Jz066i005p01321.

5. Akasofu, S. I., S. Chapman, and C. I. Meng (1965), Polar Electrojet, *Journal of Atmospheric and Terrestrial Physics*, *27*(11-1), 1275-&, doi:10.1016/0021-9169(65)90087-5.

6. Amm, O. (1997), Ionospheric elementary current systems in spherical coordinates and their application, *Journal of Geomagnetism and Geoelectricity*, *49*(7), 947-955.

7. Amm, O., and A. Viljanen (1999), Ionospheric disturbance magnetic field continuation from the ground to the ionosphere using spherical elementary current systems, *Earth Planets Space*, *51*(6), 431-440.

8. Angelopoulos, V. (2008), The THEMIS Mission, *Space Sci. Rev.*, *141*(1), 5-34, doi:10.1007/s11214-008-9336-1.

9. Angelopoulos, V., W. Baumjohann, C. F. Kennel, F. V. Coroniti, M. G. Kivelson, R. Pellat, R. J. Walker, H. Luhr, and G. Paschmann (1992), Bursty Bulk Flows in the Inner Central Plasma Sheet, *J. Geophys. Res.*, *97*(A4), 4027-4039, doi:10.1029/91ja02701.

10. Angelopoulos, V., C. F. Kennel, F. V. Coroniti, R. Pellat, M. G. Kivelson, R. J. Walker, C. T. Russell, W. Baumjohann, W. C. Feldman, and J. T. Gosling (1994), Statistical Characteristics of Bursty Bulk Flow Events, *J. Geophys. Res.*, *99*(A11), 21257-21280, doi:10.1029/94ja01263.

11. Angelopoulos, V., et al. (2008a), Tail reconnection triggering substorm onset, *Science*, *321*(5891), 931.

12. Angelopoulos, V., et al. (1996), Tailward progression of magnetotail acceleration centers: Relationship to substorm current wedge, *J. Geophys. Res.*, *101*(A11), 24599-24619, doi:10.1029/96ja01665.

13. Angelopoulos, V., A. Runov, X. Z. Zhou, D. L. Turner, S. A. Kiehas, S. S. Li, and I. Shinohara (2013), Electromagnetic Energy Conversion at Reconnection Fronts, *Science*, *341*(6153), 1478-1482, doi:10.1126/science.1236992.

14. Angelopoulos, V., et al. (2008b), First Results from the THEMIS Mission, *Space Sci. Rev.*, *141*(1-4), 453-476, doi:10.1007/s11214-008-9378-4.

15. Auster, H. U., et al. (2008), The THEMIS Fluxgate Magnetometer, *Space Sci. Rev.*, *141*(1-4), 235-264, doi:10.1007/s11214-008-9365-9.

16. Axford, W. I., and C. O. Hines (1961), A Unifying Theory of High-Latitude Geophysical Phenomena and Geomagnetic Storms, *Canadian Journal of Physics*, *39*(10), 1433-&.

17. Baker, D. N., T. I. Pulkkinen, V. Angelopoulos, W. Baumjohann, and R. L. McPherron (1996), Neutral line model of substorms: Past results and present view, *J. Geophys. Res.*, *101*(A6), 12975-13010, doi:10.1029/95ja03753.

18. Bartels, J. (1932), Terrestrial-magnetic activity and its relations to solar phenomena, *Terrestrial Magnetism and Atmospheric Electricity*, *37*(1), 1-52, doi:10.1029/TE037i001p00001.

19. Baumjohann, W. (1982), Ionospheric and field-aligned current systems in the auroral zone: a concise review, *Adv. Space Res.*, *2*(10), 55-62, doi:10.1016/0273-1177(82)90363-5.

20. Baumjohann, W. (2002), Modes of convection in the magnetotail, *Phys. Plasmas*, *9*(9), 3665-3667, doi:10.1063/1.1499116.

21. Baumjohann, W., M. Hesse, S. Kokubun, T. Mukai, T. Nagai, and A. A. Petrukovich (1999), Substorm dipolarization and recovery, *J. Geophys. Res.*, *104*(A11), 24995-25000, doi:10.1029/1999ja900282.

22. Baumjohann, W., and R. Nakamura (2001), Updating the Near-Earth Neutral Line Model, *ArXiv Physics e-prints*, 11145.

23. Baumjohann, W., R. J. Pellinen, H. J. Opgenoorth, and E. Nielsen (1981), Joint Two-Dimensional Observations of Ground Magnetic and Ionospheric Electric-Fields Associated with Auroral-Zone Currents - Current Systems Associated with Local Auroral Break-Ups, *Planetary and Space Science*, *29*(4), 431-&, doi:10.1016/0032-0633(81)90087-8.

24. Birkeland, K. (1908), *The Norwegian aurora polaris expedition 1902-1903*, H. Aschelhoug & Co.

25. Birn, J., and M. Hesse (1991), The Substorm Current Wedge and Field-Aligned Currents in MHD Simulations of Magnetotail Reconnection, *J. Geophys. Res.*, *96*(A2), 1611-1618, doi:10.1029/90JA01762.

26. Birn, J., and M. Hesse (1996), Details of current disruption and diversion in simulations of magnetotail dynamics, *J. Geophys. Res.*, *101*(A7), 15345-15358, doi:10.1029/96ja00887.

27. Birn, J., and M. Hesse (2000), The current disruption myth, *Magnetospheric Current Systems*, *118*, 285-294.

28. Birn, J., and M. Hesse (2013), The substorm current wedge in MHD simulations, *J. Geophys. Res.*, *118*(6), 3364-3376, doi:10.1002/jgra.50187.

29. Birn, J., and M. Hesse (2014), The Substorm Current Wedge: Further Insights from MHD Simulations, *J. Geophys. Res.*, 2014JA019863, doi:10.1002/2014JA019863.

30. Birn, J., M. Hesse, G. Haerendel, W. Baumjohann, and K. Shiokawa (1999), Flow braking and the substorm current wedge, *J. Geophys. Res.*, *104*(A9), 19895-19903, doi:10.1029/1999ja900173.

31. Birn, J., R. Nakamura, and M. Hesse (2013), On the propagation of blobs in the magnetotail: MHD simulations, *J. Geophys. Res.*, *118*(9), 5497-5505, doi:10.1002/jgra.50521.

32. Birn, J., R. Nakamura, E. V. Panov, and M. Hesse (2011), Bursty bulk flows and dipolarization in MHD simulations of magnetotail reconnection, *J. Geophys. Res.*, *116*(A1), A01210, doi:10.1029/2010ja016083.

33. Bonnevier, B., R. Boström, and G. Rostoker (1970), A Three-Dimensional Model Current System for Polar Magnetic Substorms, *J. Geophys. Res.*, *75*(1), 107-122, doi:10.1029/JA075i001p00107.

34. Caan, M. N., R. L. McPherron, and C. T. Russell (1978), The statistical magnetic signature of magnetospheric substorms, *Planetary and Space Science*, *26*(3), 269-279.

35. Cao, X., Z. Y. Pu, A. M. Du, V. M. Mishin, X. G. Wang, C. J. Xiao, T. L. Zhang, V. Angelopoulos, J. P. McFadden, and K. H. Glassmeier (2012), On the retreat of

near-Earth neutral line during substorm expansion phase: a THEMIS case study during the 9 January 2008 substorm, *Ann. Geophys*, *30*(1), 143-151, doi:10.5194/angeo-30-143-2012.

36. Carbary, J. F., K. Liou, A. T. Y. Lui, P. T. Newell, and C. I. Meng (2000), "Blob" analysis of auroral substorm dynamics, *Journal of Geophysical Research: Space Physics*, *105*(A7), 16083-16091, doi:10.1029/1999JA000210.

37. Chapman, S. (1918), On the times of sudden commencement of magnetic storms., *P Phys Soc Lond*, *30*, 205-214.

38. Chapman, S. (1927), The sun, the earths atmosphere, and radio transmission, *Nature*, *119*, 428-429, doi:10.1038/119428a0.

39. Chu, X., et al. (2014a), Development and Validation of Inversion Technique for Substorm Current Wedge Using Ground Magnetic Field Data, *J. Geophys. Res.*, 2013JA019185, doi:10.1002/2013JA019185.

40. Chu, X., R. L. McPherron, T.-S. Hsu, and V. Angelopoulos (2015a), Solar cycle dependence of substorm occurrence and duration: implications for onset, *J. Geophys. Res.*, 2015JA021104R

41. Chu, X., R. L. McPherron, T.-S. Hsu, and V. Angelopoulos (2015b), Solar cycle dependence of substorm occurrence and duration: implications for onset, *Journal of Geophysical Research: Space Physics*, 2015JA021104, doi:10.1002/2015JA021104.

42. Chu, X., R. L. McPherron, T.-S. Hsu, V. Angelopoulos, Z. Pu, Z. Yao, H. Zhang, and M. Connors (2015c), Magnetic mapping effects of substorm currents leading to auroral poleward expansion and equatorward retreat, *Journal of Geophysical Research: Space Physics*, 2014JA020596, doi:10.1002/2014JA020596.

43. Chu, X., et al. (2010a), THEMIS observations of two substorms on February 26, 2008, *Sci China Technol Sc*, *53*(5), 1328-1337, doi:10.1007/s11431-009-0399-3.

44. Chu, X. N., et al. (2014b), Development and validation of inversion technique for substorm current wedge using ground magnetic field data, *J. Geophys. Res.*, *119*(3), 1909-1924, doi:10.1002/2013ja019185.

45. Chu, X. N., Z. Y. Pu, X. Cao, J. Wang, V. Mishin, V. Angelopoulos, J. Liu, Y. Wei, K. H. Glassmeier, and J. Mcfadden (2010b), THEMIS observations of two substorms on February 26, 2008, *SCIENCE CHINA Technological Sciences*, *53*(5), 1328-1337 %\ 2010-1308-1318 1315:1303:1300.

46. Clauer, C. R., and Y. Kamide (1985), Dp-1 and Dp-2 Current Systems for the March 22, 1979 Substorms, *J. Geophys. Res.*, *90*(Na2), 1343-1354, doi:10.1029/Ja090ia02p01343.

47. Clauer, C. R., and R. L. McPherron (1974a), Mapping the Local Time-Universal Time Development of Magnetospheric Substorms Using Mid-Latitude Magnetic Observations, *J. Geophys. Res.*, *79*(19), 2811-2820, doi:10.1029/JA079i019p02811.

48. Clauer, C. R., and R. L. McPherron (1974b), Variability of Mid-Latitude Magnetic Parameters Used to Characterize Magnetospheric Substorms, *J. Geophys. Res.*, *79*(19), 2898-2900, doi:10.1029/JA079i019p02898.

49. Clauer, C. R., R. L. McPherron, and C. Searls (1983), Solar wind control of the low-latitude asymmetric magnetic disturbance field, *Journal of Geophysical Research, vol. 88, Mar. 1, 1983, p. 2123 2130.*, doi:10.1029/JA088iA03p02123.

50. Cliver, E. W., Y. Kamide, and A. G. Ling (2000), Mountains versus valleys: Semiannual variation of geomagnetic activity, *J. Geophys. Res.*, *105*(A2), 2413-2424, doi:10.1029/1999ja900439.

51. Connors, M., R. L. McPherron, B. J. Anderson, H. Korth, C. T. Russell, and X. Chu (2014), Electric currents of a substorm current wedge on 24 February 2010, *Geophys. Res. Lett.*, 2014GL060604, doi:10.1002/2014GL060604.

52. Connors, M. G. (1998), Auroral current systems studied using automated forward modelling, Ph.D. thesis, 427-427 p. pp, University of Alberta (Canada), Canada.

53. Coroniti, F. V., R. L. McPherron, and G. K. Parks (1968), Studies of the Magnetospheric Substorm, 3, Concept of the Magnetospheric Substorm and its Relation to Electron Precipitation and Micropulsations, *J. Geophys. Res.*, *73*(5), 1715-1722, doi:10.1029/JA073i005p01715.

54. Cortie, A. L. (1912), Sun-spots and terrestrial magnetic phenomena, 1898-1911: The cause of the annual variation in magnetic disturbances., *Monthly Notices of the Royal Astronomical Society*, *73*(1), 0052-0060.

55. Crooker, N. U., J. Feynman, and J. T. Gosling (1977), High Correlation between Long-Term Averages of Solar-Wind Speed and Geomagnetic Activity, *J. Geophys. Res.*, *82*(13), 1933-1937, doi:10.1029/Ja082i013p01933.

56. Crooker, N. U., and R. L. McPherron (1972), On the distinction between the auroral electrojet and partial ring current systems, *J. Geophys. Res., Vol. 77, p. 6886 6889*, doi:10.1029/JA077i034p06886.

57. Donovan, E., S. Mende, B. Jackel, H. Frey, M. Syrjäsuo, I. Voronkov, T. Trondsen, L. Peticolas, V. Angelopoulos, and S. Harris (2006), The THEMIS all-sky imaging array--system design and initial results from the prototype imager, *Journal of Atmospheric and Solar-Terrestrial Physics*, *68*(13), 1472-1487.

58. Dubyagin, S., V. Sergeev, S. Apatenkov, V. Angelopoulos, A. Runov, R. Nakamura, W. Baumjohann, J. McFadden, and D. Larson (2011), Can flow bursts penetrate into the inner magnetosphere?, *Geophys. Res. Lett.*, *38*(8), L08102, doi:10.1029/2011gl047016.

59. Dungey, J. W. (1961), Interplanetary Magnetic Field and Auroral Zones, *Physical Review Letters*, *6*(2), 47-&, doi:10.1103/PhysRevLett.6.47.

60. Frey, H. U., S. B. Mende, V. Angelopoulos, and E. F. Donovan (2004), Substorm onset observations by IMAGE-FUV, *J. Geophys. Res.*, *109*(A10), A10304, doi:10.1029/2004ja010607.

61. Frey, H. U., S. B. Mende, C. W. Carlson, J. C. Gérard, B. Hubert, J. Spann, R. Gladstone, and T. J. Immel (2001), The electron and proton aurora as seen by IMAGE-FUV and FAST, *Geophys. Res. Lett.*, *28*(6), 1135-1138, doi:10.1029/2000gl012352.

62. Gabrielse, C., V. Angelopoulos, A. Runov, and D. L. Turner (2014), Statistical characteristics of particle injections throughout the equatorial magnetotail, *J. Geophys. Res.*, 2013JA019638, doi:10.1002/2013JA019638.

63. Gjerloev, J. W. (2009), A Global Ground-Based Magnetometer Initiative, *Eos, Transactions American Geophysical Union*, *90*(27), 230-231, doi:10.1029/2009EO270002.

64. Gjerloev, J. W. (2012), The SuperMAG data processing technique, *J. Geophys. Res.*, *117*, doi:10.1029/2012ja017683.

65. Guo, J. P., H. X. Liu, X. S. Feng, T. I. Pulkkinen, E. I. Tanskanen, C. X. Liu, D. K. Zhong, and Y. Wang (2014a), MLT and seasonal dependence of auroral electrojets: IMAGE magnetometer network observations, *J. Geophys. Res.*, *119*(4), 3179-3188, doi:10.1002/2014ja019843.

66. Guo, J. P., T. I. Pulkkinen, E. I. Tanskanen, X. S. Feng, B. A. Emery, H. X. Liu, C. X. Liu, and D. K. Zhong (2014b), Annual variations in westward auroral electrojet and substorm occurrence rate during solar cycle 23, *J. Geophys. Res.*, *119*(3), 2061-2068, doi:10.1002/2013ja019742.

67. Haerendel, G. (1992a), Disruption, ballooning or auroral avalanche—On the cause of substorms, paper presented at Proceedings of the First International Conference on Substorms (ICS-1).

68. Haerendel, G. (1992b), Disruption, ballooning or auroral avalanche—On the cause of substorms, paper presented at Proceedings of the International Conference on Substorms (ICS-1), Kiruna, Sweden, 23–27 March 1992, Eur. Space Agency Spec. Publ., ESA SP.

69. Hasegawa, A., and T. Sato (1980), *Generation of field aligned current during substorm*, 529-542 pp., Springer Netherlands, doi:10.1007/978-94-009-9519-2_28.

70. Hashimoto, K. K., T. Kikuchi, S. Watari, and M. A. Abdu (2011), Polar-equatorial ionospheric currents driven by the region 2 field-aligned currents at the onset of substorms, *J. Geophys. Res.*, *116*(A9), A09217, doi:10.1029/2011ja016442.

71. Holzworth, R. H., and C. I. Meng (1975), Mathematical Representation of Auroral Oval, *Geophys. Res. Lett.*, *2*(9), 377-380, doi:10.1029/Gl002i009p00377.

72. Hones, E. W. (1977), Substorm Processes in Magnetotail - Comments on on Hot Tenuous Plasmas, Fireballs, and Boundary-Layers in Earths Magnetotail, *J. Geophys. Res.*, *82*(35), 5633-5640, doi:10.1029/Ja082i035p05633.

73. Hones, E. W., S. I. Akasofu, P. Perreault, S. J. Bame, and S. Singer (1970), Poleward expansion of the auroral oval and associated phenomena in the magnetotail during auroral substorms: 1, *J. Geophys. Res.*, *75*(34), 7060-7074, doi:10.1029/JA075i034p07060.

74. Hones, E. W., J. R. Asbridge, S. J. Bame, and S. Singer (1973), Substorm Variations of Magnetotail Plasma Sheet from Xsm =-6 Re to Xsm =-60 Re, *Eos T Am Geophys Un*, *54*(1), 58-&.

75. Horning, B. L., Mcpherro.Rl, and D. D. Jackson (1974a), Application of Linear Inverse Theory to a Line Current Model of Substorm Current Systems, *Journal of Geophysical Research*, *79*(34), 5202-5210, doi:Doi 10.1029/Ja079i034p05202.

76. Horning, B. L., R. L. McPherron, D. D. Jackson, Mcpherro.Rl, and D. D. Jackson (1974b), Application of Linear Inverse Theory to a Line Current Model of Substorm Current Systems, *J. Geophys. Res.*, *79*, 5202-5210, doi:10.1029/Ja079i034p05202.

77. Hsu, T. S., and R. L. McPherron (2007), A statistical study of the relation of Pi 2 and plasma flows in the tail, *J. Geophys. Res.*, *112*(A5), doi:10.1029/2006ja011782.

78. Hsu, T. S., and R. L. McPherron (2012), A statistical analysis of substorm associated tail activity, *Adv. Space Res.*, *50*(10), 1317-1343, doi:10.1016/j.asr.2012.06.034.

79. Hsu, T. S., R. L. McPherron, V. Angelopoulos, Y. S. Ge, H. Zhang, C. Russell, X. N. Chu, and J. Kissinger (2012), A statistical analysis of the association between fast plasma flows and Pi2 pulsations, *J. Geophys. Res.*, *117*, doi:10.1029/2012ja018173.

80. Hsu, T. S., R. L. Mcpherron, J. Kissinger, X. Chu, and H. Zhang (2015), An Investigation of the Solar Cycle Effect on Substorms, *To be Submitted to Journal of Geophysical Research*.

81. Hubert, B., J. C. Gerard, D. S. Evans, M. Meurant, S. B. Mende, H. U. Frey, and T. J. Immel (2002), Total electron and proton energy input during auroral substorms:

Remote sensing with IMAGE-FUV, *Journal of Geophysical Research: Space Physics*, *107*(A8), doi:10.1029/2001JA009229.

82. Iijima, T., and T. Nagata (1972), Signatures for Substorm Development of Growth Phase and Expansion Phase, *Planetary and Space Science*, *20*(7), 1095-&, doi:10.1016/0032-0633(72)90219-X.

83. Jacquey, C., J. A. Sauvaud, and J. Dandouras (1991), Location and propagation of the magnetotail current disruption during substorm expansion: Analysis and simulation of an ISEE multi-onset event, *Geophys. Res. Lett.*, *18*(3), 389-392, doi:10.1029/90GL02789.

84. Jelly, D., and N. Brice (1967), Changes in Van Allen Radiation Associated with Polar Substorms, *J. Geophys. Res.*, *72*(23), 5919-&, doi:10.1029/JZ072i023p05919.

85. Kamide, Y., S. I. Akasofu, and A. Brekke (1976), Ionospheric currents obtained from the Chatanika radar and ground magnetic perturbations at the Auroral latitude, *Planetary and Space Science*, *24*(3), 193-201, doi:10.1016/0032-0633(76)90016-7.

86. Keiling, A., et al. (2009), Substorm current wedge driven by plasma flow vortices: THEMIS observations, *J. Geophys. Res.*, *114*(A1), A00C22, doi:10.1029/2009ja014114.

87. Keiling, A., and K. Takahashi (2011), Review of Pi2 Models, *Space Sci. Rev.*, *161*(1-4), 63-148, doi:10.1007/s11214-011-9818-4.

88. Kepko, L., M. G. Kivelson, and K. Yumoto (2001), Flow bursts, braking, and Pi 2 pulsations, *J. Geophys. Res.*, *106*, 1903-1915.

89. Kepko, L., R. L. McPherron, O. Amm, S. Apatenkov, W. Baumjohann, J. Birn, M. Lester, R. Nakamura, T. I. Pulkkinen, and V. Sergeev (2014), Substorm Current Wedge Revisited, *Space Sci. Rev.*, 1-46, doi:10.1007/s11214-014-0124-9.

90. Kisabeth, J. L., and G. Rostoker (1970), Dynamic Development of Polar Electrojets, *Eos T Am Geophys Un*, *51*(11), 808-&.

91. Kisabeth, J. L., and G. Rostoker (1971), Development of the Polar Electrojet during Polar Magnetic Substorms, *J. Geophys. Res.*, *76*(28), 6815-6828, doi:10.1029/JA076i028p06815.

92. Kisabeth, J. L., and G. Rostoker (1977), Modelling of three-dimensional current systems associated with magnetospheric substorms, *Geophys. J. Roy. Astron. Soc.*, *49*(3), 655-683, doi:10.1111/j.1365-246X.1977.tb01310.x.

93. Kissinger, J., R. L. McPherron, T. S. Hsu, and V. Angelopoulos (2012), Diversion of plasma due to high pressure in the inner magnetosphere during steady magnetospheric convection, *J. Geophys. Res.*, *117*, doi:10.1029/2012ja017579.

94. Kokubun, S. (1972), Relationship of Interplanetary Magnetic-Field Structure with Development of Substorm and Storm Main Phase, *Planetary and Space Science*, *20*(7), 1033-&, doi:10.1016/0032-0633(72)90214-0.

95. Kotikov, A., Y. A. Latov, and O. Troshichev (1987), Structure of auroral electrojets by the data from a meridional chain of magnetic stations, *Geophysica*, *23*(2), 143-154.

96. Kubyshkina, M., V. Sergeev, N. Tsyganenko, V. Angelopoulos, A. Runov, E. Donovan, H. Singer, U. Auster, and W. Baumjohann (2011), Time-dependent magnetospheric configuration and breakup mapping during a substorm, *J. Geophys. Res.*, *116*, A00I27, doi:10.1029/2010ja015882.

97. Kubyshkina, M. V., V. K. Sergeev, and T. I. Pulkkinen (1999), Hybrid input algorithm: An event-oriented magnetospheric model, *J. Geophys. Res.*, *104*(A11), 24977-24993, doi:10.1029/1999ja900222.

98. Li, S. S., V. Angelopoulos, A. Runov, S. A. Kiehas, and X. Z. Zhou (2013), Plasmoid growth and expulsion revealed by two-point ARTEMIS observations, *J. Geophys. Res.*, *118*(5), 2133-2144, doi:10.1002/Jgra.50105.

99. Li, S. S., J. Liu, V. Angelopoulos, A. Runov, X. Z. Zhou, and S. A. Kiehas (2014), Antidipolarization fronts observed by ARTEMIS, *J. Geophys. Res.*, *119*(9), doi:10.1002/2014ja020062.

100. Liou, K., C. I. Meng, A. T. Y. Lui, P. T. Newell, and S. Wing (2002), Magnetic dipolarization with substorm expansion onset, *J. Geophys. Res.*, *107*(A7), 1131, doi:10.1029/2001ja000179.

101. Liou, K., P. T. Newell, D. G. Sibeck, C. I. Meng, M. Brittnacher, and G. Parks (2001), Observation of IMF and seasonal effects in the location of auroral substorm onset, *Journal of Geophysical Research: Space Physics*, *106*(A4), 5799-5810, doi:10.1029/2000JA003001.

102. Liu, J., V. Angelopoulos, X. Chu, X.-Z. Zhou, and C. Yue (2015), Substorm Current Wedge Composition by Wedgelets, *Geophys. Res. Lett.*, 2015GL063289, doi:10.1002/2015GL063289.

103. Liu, J., V. Angelopoulos, A. Runov, and X. Z. Zhou (2013a), On the current sheets surrounding dipolarizing flux bundles in the magnetotail: The case for wedgelets, *Journal of Geophysical Research: Space Physics*, *118*(5), 2000-2020, doi:10.1002/jgra.50092.

104. Liu, J., V. Angelopoulos, A. Runov, and X. Z. Zhou (2013b), On the current sheets surrounding dipolarizing flux bundles in the magnetotail: The case for wedgelets, *J. Geophys. Res.*, *118*(5), 2000-2020, doi:10.1002/jgra.50092.

105. Liu, J., V. Angelopoulos, X. Z. Zhou, and A. Runov (2014), Magnetic flux transport by dipolarizing flux bundles, *J. Geophys. Res.*, *119*(2), 909-926, doi:10.1002/2013ja019395.

106. Liu, J., V. Angelopoulos, X. Z. Zhou, A. Runov, and Z. H. Yao (2013c), On the role of pressure and flow perturbations around dipolarizing flux bundles, *J. Geophys. Res.*, *118*(11), 7104-7118, doi:10.1002/2013ja019256.

107. Lui, A. T. Y. (1978), Estimates of Current Changes in Geomagnetotail Associated with a Substorm, *Geophys. Res. Lett.*, *5*(10), 853-856, doi:10.1029/Gl005i010p00853.

108. Lui, A. T. Y. (1996), Current disruption in the Earth's magnetosphere: Observations and models, *J. Geophys. Res.*, *101*(A6), 13067-13088, doi:10.1029/96ja00079.

109. Lui, A. T. Y. (2009), Comment on "Tail Reconnection Triggering Substorm Onset", *Science*, *324*(5933), doi:10.1126/science.1167726.

110. Lui, A. T. Y., A. Mankofsky, C. L. Chang, K. Papadopoulos, and C. S. Wu (1990), A Current Disruption Mechanism in the Neutral Sheet - a Possible Trigger for Substorm Expansions, *Geophys. Res. Lett.*, *17*(6), 745-748, doi:10.1029/Gl017i006p00745.

111. Lui, A. T. Y., and J. S. Murphree (1998), A substorm model with onset location tied to an auroral arc, *Geophys. Res. Lett.*, *25*(8), 1269-1272, doi:10.1029/98gl00758.

112. Lui, A. T. Y., E. Spanswick, E. F. Donovan, J. Liang, W. W. Liu, O. LeContel, and Q. G. Zong (2010), A transient narrow poleward extrusion from the diffuse aurora and the concurrent magnetotail activity, *J. Geophys. Res.*, *115*, doi:10.1029/2010ja015449.

113. Mareschal, M. (1976), On the problem of simulating the Earth's induction effects in modeling polar magnetic substorms, *Rev. Geophys.*, *14*(3), 403-409, doi:10.1029/RG014i003p00403.

114. Mareschal, M., and J. L. Kisabeth (1977), Simulating the earth's induction effects on substorm data recorded at mid-latitude stations-The three-dimensional problem, *Journal of Geomagnetism and Geoelectricity*, *29*, 81-104.

115. Markwardt, C. B., D. Durand, and P. Dowler (2009), Non-linear Least-squares Fitting in IDL with MPFIT, in *Astr Soc P*, edited by D. A. Bohlender, p. 251.

116. McFadden, J. P., C. W. Carlson, D. Larson, M. Ludlam, R. Abiad, B. Elliott, P. Turin, M. Marckwordt, and V. Angelopoulos (2008), The THEMIS ESA Plasma Instrument and In-flight Calibration, *Space Sci. Rev.*, *141*(1-4), 277-302, doi:10.1007/s11214-008-9440-2.

117. McPherron, R. (1991), Physical processes producing magnetospheric substorms and magnetic storms, paper presented at Geomagnetism.

118. McPherron, R., L. Kepko, T. Pulkkinen, T. Hsu, J. Weygand, and L. Bargatze (2009), Changes in the response of the AL Index with solar cycle and epoch within a corotating interaction region, *Ann. Geophys*, *27*, 3165–3178.

119. McPherron, R. L. (1970), Growth phase of magnetospheric substorms, *J. Geophys. Res.*, *75*(28), 5592-5599, doi:10.1029/JA075i028p05592.

120. McPherron, R. L. (1972), Substorm related changes in the geomagnetic tail: the growth phase, *Planetary and Space Science*, *20*(9), 1521-1539.

121. McPherron, R. L. (1994), The substorm growth phase, *Substorm 2, edited by J.R. Kan, J.D. Craven, and S.-I. Akasofu, Geophysical Institute, University of Alaska, University of Alaska, Fairbanks, AK 99775-0800.*

122. McPherron, R. L., D. N. Baker, T. I. Pulkkinen, T. S. Hsu, J. Kissinger, and X. Chu (2013), Changes in solar wind–magnetosphere coupling with solar cycle, season, and time relative to stream interfaces, *Journal of Atmospheric and Solar-Terrestrial Physics*, *99*(0), 1-13, doi:10.1016/j.jastp.2012.09.003.

123. McPherron, R. L., and J. N. Barfield (1980), A Seasonal Change in the Effect of Field-Aligned Currents at Synchronous Orbit, *J. Geophys. Res.*, *85*(A12), 6743-6746, doi:10.1029/JA085iA12p06743.

124. McPherron, R. L., T. S. Hsu, and X. Chu (2014), An Optimum Solar Wind Coupling Function for the AL Index, *J. Geophys. Res.*, doi:2014JA020619.

125. McPherron, R. L., T. S. Hsu, J. Kissinger, X. Chu, and V. Angelopoulos (2011), Characteristics of plasma flows at the inner edge of the plasma sheet, *J. Geophys. Res.*, *116*, doi:10.1029/2010ja015923.

126. McPherron, R. L., G. K. Parks, and F. V. Coroniti (1967), Relation of correlated magnetic micropulsations and electron precipitation to the auroral substorm, *Proceedings of the Conjugate Point Symposium, Boulder, CO ITSA Mem*, *72*.

127. McPherron, R. L., C. T. Russell, and M. P. Aubry (1973), Satellite studies of magnetospheric substorms on August 15, 1968: 9. Phenomenological model for substorms, *J. Geophys. Res.*, *78*(16), 3131-3149, doi:10.1029/JA078i016p03131.

128. Mende, S. B., S. E. Harris, H. U. Frey, V. Angelopoulos, C. T. Russell, E. Donovan, B. Jackel, M. Greffen, and L. M. Peticolas (2008), The THEMIS Array of Ground-based Observatories for the Study of Auroral Substorms, *Space Sci. Rev.*, *141*(1-4), 357-387, doi:10.1007/s11214-008-9380-x.

129. Mende, S. B., et al. (2000), Far ultraviolet imaging from the IMAGE spacecraft. 1. System design, *Space Sci. Rev.*, *91*(1-2), 243-270, doi:10.1023/A:1005271728567.

130. Murphy, K. R., I. R. Mann, I. J. Rae, C. L. Waters, B. J. Anderson, D. K. Milling, H. J. Singer, and H. Korth (2012), Reduction in field-aligned currents preceding and local to auroral substorm onset, *Geophys. Res. Lett.*, *39*, doi:10.1029/2012gl052798.

131. Murphy, K. R., I. R. Mann, I. J. Rae, C. L. Waters, H. U. Frey, A. Kale, H. J. Singer, B. J. Anderson, and H. Korth (2013), The detailed spatial structure of field-aligned currents comprising the substorm current wedge, *J. Geophys. Res.*, *118*(12), 7714-7727, doi:10.1002/2013JA018979.

132. Nagai, T. (1982a), Local time dependence of electron flux changes during substorms derived from multi-satellite observation at synchronous orbit, *J. Geophys. Res.*, *87*, 3456-3468, doi:10.1029/Ja087ia05p03456.

133. Nagai, T. (1982b), Observed Magnetic Substorm Signatures at Synchronous Altitude, *J. Geophys. Res.*, *87*(A6), 4405-4417, doi:10.1029/JA087iA06p04405.

134. Nakamura, R., W. Baumjohann, R. Schodel, M. Brittnacher, V. A. Sergeev, M. Kubyshkina, T. Mukai, and K. Liou (2001), Earthward flow bursts, auroral streamers, and small expansions, *J. Geophys. Res.*, *106*(A6), 10791-10802, doi:10.1029/2000ja000306.

135. Nakamura, R., T. Oguti, T. Yamamoto, and S. Kokubun (1993), Equatorward and poleward expansion of the auroras during auroral substorms, *J. Geophys. Res.*, *98*(A4), 5743-5759, doi:10.1029/92JA02230.

136. Newell, P. T., and J. W. Gjerloev (2011a), Evaluation of SuperMAG auroral electrojet indices as indicators of substorms and auroral power, *J. Geophys. Res.*, *116*, doi:10.1029/2011ja016779.

137. Newell, P. T., and J. W. Gjerloev (2011b), Substorm and magnetosphere characteristic scales inferred from the SuperMAG auroral electrojet indices, *J. Geophys. Res.*, *116*, doi:10.1029/2011ja016936.

138. Newell, P. T., J. W. Gjerloev, and E. J. Mitchell (2013), Space climate implications from substorm frequency, *Journal of Geophysical Research: Space Physics*, *118*(10), 2013JA019081, doi:10.1002/jgra.50597.

139. Newell, P. T., T. Sotirelis, K. Liou, C. I. Meng, and F. J. Rich (2007), A nearly universal solar wind-magnetosphere coupling function inferred from 10 magnetospheric state variables, *J. Geophys. Res.*, *112*(A1), doi:10.1029/2006ja012015.

140. Nishida, A. (1968a), Coherence of Geomagnetic Dp 2 Fluctuations with Interplanetary Magnetic Variations, *J. Geophys. Res.*, *73*(17), 5549-&, doi:10.1029/JA073i017p05549.

141. Nishida, A. (1968b), Geomagnetic Dp 2 Fluctuations and Associated Magnetospheric Phenomena, *J. Geophys. Res.*, *73*(5), 1795-&, doi:10.1029/JA073i005p01795.

142. O'Brien, T. P., and R. L. McPherron (2002), Seasonal and diurnal variation of Dst dynamics, *J. Geophys. Res.*, *107*(A11), doi:10.1029/2002ja009435.

143. Obayashi, T., and A. Nishida (1968), Large-scale electric field in the magnetosphere, *Space Sci. Rev.*, *8*(1), 3-31, doi:10.1007/BF00362569.

144. Ohtani, S., S. Kokubun, R. Nakamura, R. C. Elphic, C. T. Russell, and D. N. Baker (1990), Field-Aligned Current Signatures in the near-Tail Region .2. Coupling between the Region-1 and the Region-2 Systems, *J. Geophys. Res.*, *95*(A11), 18913-18927, doi:10.1029/Ja095ia11p18913.

145. Ohtani, S., S. Kokubun, and C. T. Russell (1992a), Radial Expansion of the Tail Current Disruption during Substorms - a New Approach to the Substorm Onset Region, *J. Geophys. Res.*, *97*(A3), 3129-3136, doi:10.1029/91ja02470.

146. Ohtani, S., H. J. Singer, and T. Mukai (2006), Effects of the fast plasma sheet flow on the geosynchronous magnetic configuration: Geotail and GOES coordinated study, *J. Geophys. Res.*, *111*(A1), A01204, doi:10.1029/2005ja011383.

147. Ohtani, S., K. Takahashi, L. J. Zanetti, T. A. Potemra, R. W. Mcentire, and T. Iijima (1992b), Initial Signatures of Magnetic-Field and Energetic Particle Fluxes at Tail Reconfiguration - Explosive Growth-Phase, *J. Geophys. Res.*, *97*(A12), 19311-19324, doi:10.1029/92ja01832.

148. Oldenburg, D. W. (1976), Ionospheric current structure as determined from ground-based magnetometer data, *Geophys. J. Roy. Astron. Soc.*, *46*(1), 41-66, doi:10.1111/j.1365-246X.1976.tb01631.x.

149. Pellinen, R. J., T. I. Pulkkinen, A. Huuskonen, and K. H. Glassmeier (1995), On the Dynamical Development of the Downward Field-Aligned Current in the Substorm Current Wedge, *J. Geophys. Res.*, *100*(A8), 14863-14873, doi:10.1029/95ja00227-B.

150. Petrukovich, A. A., and A. G. Yahnin (2006), The substorm onset location controversy, *Space Sci. Rev.*, *122*(1-4), 81-87, doi:10.1007/s11214-006-7022-8.

151. Pontius, D. H., and R. A. Wolf (1990), Transient Flux Tubes in the Terrestrial Magnetosphere, *Geophys. Res. Lett.*, *17*(1), 49-52, doi:10.1029/GL017i001p00049.

152. Pu, Z. Y., et al. (2010a), THEMIS observations of substorms on 26 February 2008 initiated by magnetotail reconnection, *J. Geophys. Res.*, *115*, doi:10.1029/2009ja014217.

153. Pu, Z. Y., et al. (2010b), THEMIS observations of substorms on 26 February 2008 initiated by magnetotail reconnection, *J. Geophys. Res.*, *115*(A2), A02212.

154. Pu, Z. Y., et al. (1999), Ballooning instability in the presence of a plasma flow: A synthesis of tail reconnection and current disruption models for the initiation of substorms, *J. Geophys. Res.*, *104*(A5), 10235-10248, doi:10.1029/1998ja900104.

155. Pu, Z. Y., A. Korth, Z. X. Chen, Z. X. Liu, S. Y. Fu, G. Zong, M. H. Hong, and X. M. Wang (2001), A global synthesis model of dipolarization at substorm expansion onset, *Journal of Atmospheric and Solar-Terrestrial Physics*, *63*(7), 671-681, doi:10.1016/s1364-6826(00)00183-8.

156. Pulkkinen, A., et al. (2003), Ionospheric equivalent current distributions determined with the method of spherical elementary current systems, *J. Geophys. Res.*, *108*(A2), doi:10.1029/2001ja005085.

157. Pulkkinen, T. I., D. N. Baker, D. H. Fairfield, R. J. Pellinen, J. S. Murphree, R. D. Elphinstone, R. L. Mcpherron, J. F. Fennell, R. E. Lopez, and T. Nagai (1991), Modeling the Growth-Phase of a Substorm Using the Tsyganenko Model and Multi-Spacecraft Observations - Cdaw-9, *Geophys. Res. Lett.*, *18*(11), 1963-1966, doi:10.1029/91gl02002.

158. Pytte, T., R. L. Mcpherron, and S. Kokubun (1976), Ground Signatures of Expansion Phase during Multiple Onset Substorms, *Planetary and Space Science*, *24*(12), 1115-1132, doi:10.1016/0032-0633(76)90149-5.

159. Raeder, J., and R. L. McPherron (1998), Global MHD simulations of the substorm current wedge and dipolarization, paper presented at Substorms-4: International Conference on Substorms-4, Lake Hamana, Japan, March 9-13, 1998, Springer.

160. Ritter, P., and H. Lühr (2008), Near-Earth magnetic signature of magnetospheric substorms and an improved substorm current model, *Ann. Geophys*, *26*(9), 2781-2793.

161. Rostoker, G., C. W. Anderson, Oldenbur.Dw, P. A. Camfield, D. I. Gough, and H. Porath (1970), Development of a polar magnetic substorm current system, *J. Geophys. Res.*, *75*(31), 6318-&, doi:10.1029/JA075i031p06318.

162. Rostoker, G., and J. L. Kisabeth (1973), Response of the Polar Electrojets in the Evening Sector to Polar Magnetic Substorms, *J. Geophys. Res.*, *78*(25), 5559-5571, doi:10.1029/JA078i025p05559.

163. Runov, A., et al. (2011), Dipolarization fronts in the magnetotail plasma sheet, *Planetary and Space Science*, *59*(7), 517-525, doi:10.1016/j.pss.2010.06.006.

164. Runov, A., V. Angelopoulos, M. I. Sitnov, V. A. Sergeev, J. Bonnell, J. P. McFadden, D. Larson, K. H. Glassmeier, and U. Auster (2009), THEMIS observations of an earthward-propagating dipolarization front, *Geophys. Res. Lett.*, *36*, doi:10.1029/2009gl038980.

165. Runov, A., V. A. Sergeev, V. Angelopoulos, K. H. Glassmeier, and H. J. Singer (2014), Diamagnetic oscillations ahead of stopped dipolarization fronts, *Journal of Geophysical Research: Space Physics*, n/a-n/a, doi:10.1002/2013JA019384.

166. Russell, C. T., P. J. Chi, D. J. Dearborn, Y. S. Ge, B. Kuo-Tiong, J. D. Means, D. R. Pierce, K. M. Rowe, and R. C. Snare (2008), THEMIS Ground-Based Magnetometers, *Space Sci. Rev.*, *141*(1-4), 389-412, doi:10.1007/s11214-008-9337-0.

167. Russell, C. T., and Mcpherro.Rl (1973), Semiannual Variation of Geomagnetic Activity, *J. Geophys. Res.*, *78*(1), 92-108, doi:10.1029/Ja078i001p00092.

168. Sato, T., and T. Iijima (1979), Primary Sources of Large-Scale Birkeland Currents, *Space Sci. Rev.*, *24*(3), 347-366.

169. Sergeev, V., Y. Nishimura, M. Kubyshkina, V. Angelopoulos, R. Nakamura, and H. Singer (2012), Magnetospheric location of the equatorward prebreakup arc, *J. Geophys. Res.*, *117*, doi:10.1029/2011ja017154.

170. Sergeev, V. A., I. A. Chernyaev, V. Angelopoulos, A. V. Runov, and R. Nakamura (2014a), Stopping flow bursts and their role in the generation of the substorm current wedge, *Geophys. Res. Lett.*, *41*(4), 1106-1112, doi:10.1002/2014GL059309.

171. Sergeev, V. A., T. A. Kornilova, I. A. Kornilov, V. Angelopoulos, M. V. Kubyshkina, M. Fillingim, R. Nakamura, J. P. McFadden, and D. Larson (2010), Auroral signatures of the plasma injection and dipolarization in the inner magnetosphere, *J. Geophys. Res.*, *115*(A2), A02202, doi:10.1029/2009ja014522.

172. Sergeev, V. A., A. V. Nikolaev, N. A. Tsyganenko, V. Angelopoulos, A. V. Runov, H. J. Singer, and J. Yang (2014b), Testing a two-loop pattern of the substorm

current wedge (SCW2L), *Journal of Geophysical Research: Space Physics*, n/a-n/a, doi:10.1002/2013JA019629.

173. Sergeev, V. A., N. A. Tsyganenko, M. V. Smirnov, A. V. Nikolaev, H. J. Singer, and W. Baumjohann (2011), Magnetic effects of the substorm current wedge in a "spread-out wire" model and their comparison with ground, geosynchronous, and tail lobe data, *J. Geophys. Res.*, *116*(A7), A07218, doi:10.1029/2011ja016471.

174. Sergeev, V. A., L. I. Vagina, R. D. Elphinstone, J. S. Murphree, D. J. Hearn, L. L. Cogger, and M. L. Johnson (1996), Comparison of UV optical signatures with the substorm current wedge as predicted by an inversion algorithm, *J. Geophys. Res.*, *101*(A2), 2615-2627, doi:10.1029/95ja00537.

175. Shiokawa, K., W. Baumjohann, and G. Haerendel (1997), Braking of high speed flows in the near Earth tail, *Geophys. Res. Lett.*, *24*(10), 1179-1182, doi:10.1029/97gl01062.

176. Shiokawa, K., et al. (1998a), High-speed ion flow, substorm current wedge, and multiple Pi 2 pulsations, *J. Geophys. Res.*, *103*(A3), 4491-4507, doi:10.1029/97ja01680.

177. Shiokawa, K., G. Haerendel, and W. Baumjohann (1998b), Azimuthal pressure gradient as driving force of substorm currents, *Geophys. Res. Lett.*, *25*(7), 959-962, doi:10.1029/98gl00540.

178. Shue, J. H., et al. (1998), Magnetopause location under extreme solar wind conditions, *J. Geophys. Res.*, *103*(A8), 17691-17700, doi:10.1029/98ja01103.

179. Shukhtina, M. A., E. I. Gordeev, and V. A. Sergeev (2009), Time-varying magnetotail magnetic flux calculation: a test of the method, *Ann. Geophys.*, *27*(4), 1583-1591, doi:10.5194/angeo-27-1583-2009.

180. Siscoe, G. L., and T. S. Huang (1985), Polar-Cap Inflation and Deflation, *J. Geophys. Res.*, *90*(Na1), 543-547, doi:10.1029/Ja090ia01p00543.

181. Sun, W. J., S. Y. Fu, G. K. Parks, J. Liu, Z. H. Yao, Q. Q. Shi, Q. G. Zong, S. Y. Huang, Z. Y. Pu, and T. Xiao (2013), Field-aligned currents associated with dipolarization fronts, *Geophys. Res. Lett.*, *40*(17), 4503-4508, doi:10.1002/grl.50902.

182. Svalgaard, L. (2011), Geomagnetic semiannual variation is not overestimated and is not an artifact of systematic solar hemispheric asymmetry, *Geophys. Res. Lett.*, *38*, doi:10.1029/2011gl048616.

183. Svalgaard, L., and E. W. Cliver (2007), Long-term geomagnetic indices and their use in inferring solar wind parameters in the past, *Adv. Space Res.*, *40*(7), 1112-1120, doi:10.1016/j.asr.2007.06.066.

184. Svalgaard, L., E. W. Cliver, and A. G. Ling (2002), The semiannual variation of great geomagnetic storms, *Geophys. Res. Lett.*, *29*(16), doi:10.1029/2001gl014145.

185. Takada, T., R. Nakamura, W. Baumjohann, Y. Asano, M. Volwerk, T. L. Zhang, B. Klecker, H. Rème, E. A. Lucek, and C. Carr (2006), Do BBFs contribute to inner magnetosphere dipolarizations: Concurrent Cluster and Double Star observations, *Geophys. Res. Lett.*, *33*(21), L21109, doi:10.1029/2006gl027440.

186. Tanaka, T., A. Nakamizo, A. Yoshikawa, S. Fujita, H. Shinagawa, H. Shimazu, T. Kikuchi, and K. K. Hashimoto (2010), Substorm convection and current system deduced from the global simulation, *Journal of Geophysical Research: Space Physics*, *115*(A5), A05220, doi:10.1029/2009JA014676.

187. Tang, C. L., L. Lu, M. Zhou, and Z. H. Yao (2013), THEMIS observations of electron acceleration associated with the evolution of substorm dipolarization in the near-Earth tail, *J. Geophys. Res.*, *118*(7), 4237-4247, doi:10.1002/Jgra.50418.

188. Tanskanen, E. I. (2009), A comprehensive high-throughput analysis of substorms observed by IMAGE magnetometer network: Years 1993–2003 examined, *Journal of Geophysical Research: Space Physics*, *114*(A5), A05204, doi:10.1029/2008JA013682.

189. Tsyganenko, N. A. (1989), A magnetospheric magnetic field model with a warped tail current sheet, *Planet. Space Sci.*, *37*(1), 5-20, doi:10.1016/0032-0633(89)90066-4.

190. Tsyganenko, N. A. (1997), An empirical model of the substorm current wedge, *J. Geophys. Res.*, *102*(A9), 19935-19941, doi:10.1029/97ja01904.

191. Tsyganenko, N. A., and D. P. Stern (1996), Modeling the global magnetic field of the large-scale Birkeland current systems, *J. Geophys. Res.*, *101*(A12), 27187-27198, doi:10.1029/96ja02735.

192. Vagina, L. I., V. A. Sergeev, D. N. Baker, and H. J. Singer (1996), Use of mid-latitude magnetic data for modelling and diagnostics of magnetospheric substorms, *Adv. Space Res.*, *18*(8), 229-232, doi:10.1016/0273-1177(95)00987-6.

193. Vagina, L. I., V. A. Sergeev, A. L. Kotikov, and E. M. Shishkina (1997), On the relationship between parameters of substorm current wedge and westward electrojet, *Adv. Space Res.*, *20*(3), 477-480, doi:10.1016/s0273-1177(97)00714-x.

194. Vanhamaki, H., O. Amm, and A. Viljanen (2003), One-dimensional upward continuation of the ground magnetic field disturbance using spherical elementary current systems, *Earth Planets Space*, *55*(10), 613-625.

195. Vasyliunas, V. (1970), Mathematical Models of Magnetospheric Convection and its Coupling to the Ionosphere, in *Particles and Fields in the Magnetosphere*, edited by B. M. McCormac, pp. 60-71, Springer Netherlands, doi:10.1007/978-94-010-3284-1_6.

196. Weimer, D. R. (2004), Correction to Predicting interplanetary magnetic field (IMF) propagation delay times using the minimum variance technique&#8221, *J. Geophys. Res.*, *109*(A12), A12104, doi:10.1029/2004ja010691.

197. Weimer, D. R., D. M. Ober, N. C. Maynard, M. R. Collier, D. J. McComas, N. F. Ness, C. W. Smith, and J. Watermann (2003), Predicting interplanetary magnetic field (IMF) propagation delay times using the minimum variance technique, *J. Geophys. Res.*, *108*(A1), 1026, doi:10.1029/2002ja009405.

198. Weygand, J. M., O. Amm, A. Viljanen, V. Angelopoulos, D. Murr, M. J. Engebretson, H. Gleisner, and I. Mann (2011), Application and validation of the spherical elementary currents systems technique for deriving ionospheric equivalent currents with the North American and Greenland ground magnetometer arrays, *J. Geophys. Res.*, *116*(A3), A03305, doi:10.1029/2010ja016177.

199. Weygand, J. M., R. L. Mcpherron, K. Kauristie, H. U. Frey, and T. S. Hsu (2008), Relation of auroral substorm onset to local AL index and dispersionless particle injections, *Journal of Atmospheric and Solar-Terrestrial Physics*, *70*(18), 2336-2345, doi:10.1016/j.jastp.2008.09.030.

200. Xing, X., L. R. Lyons, V. Angelopoulos, D. Larson, C. Carlson, A. Runov, and U. Auster (2010), Plasma sheet pressure evolution related to substorms, *J. Geophys. Res.*, *115*(A1), A01212, doi:10.1029/2009ja014315.

201. Xing, X., L. R. Lyons, V. Angelopoulos, D. Larson, J. McFadden, C. Carlson, A. Runov, and U. Auster (2009), Azimuthal plasma pressure gradient in quiet time plasma sheet, *Geophys. Res. Lett.*, *36*(14), L14105, doi:10.1029/2009gl038881.

202. Xing, X., L. R. Lyons, Y. Nishimura, V. Angelopoulos, E. Donovan, E. Spanswick, J. Liang, D. Larson, C. Carlson, and U. Auster (2011), Near-Earth

plasma sheet azimuthal pressure gradient and associated auroral development soon before substorm onset, *J. Geophys. Res.*, *116*, doi:10.1029/2011ja016539.

203. Xing, X., L. R. Lyons, X. Z. Zhou, V. Angelopoulos, E. Donovan, D. Larson, C. Carlson, and U. Auster (2012), On the formation of pre-onset azimuthal pressure gradient in the near-Earth plasma sheet, *J. Geophys. Res.*, *117*, doi:10.1029/2012ja017840.

204. Yang, J., F. R. Toffoletto, and Y. Song (2010), Role of depleted flux tubes in steady magnetospheric convection: Results of RCM-E simulations, *J. Geophys. Res.*, *115*, A00I11, doi:10.1029/2010ja015731.

205. Yang, J., F. R. Toffoletto, R. A. Wolf, and S. Sazykin (2011), RCM-E simulation of ion acceleration during an idealized plasma sheet bubble injection, *J. Geophys. Res.*, *116*(A5), A05207, doi:10.1029/2010ja016346.

206. Yao, Z. H., et al. (2012), Mechanism of substorm current wedge formation: THEMIS observations, *Geophys. Res. Lett.*, *39*(13), L13102, doi:10.1029/2012gl052055.

207. Yao, Z. H., et al. (2014), Current reduction in a pseudo-breakup event: THEMIS observations, *Journal of Geophysical Research: Space Physics*, 2014JA020186, doi:10.1002/2014JA020186.

208. Yao, Z. H., et al. (2013), Current structures associated with dipolarization fronts, *J. Geophys. Res.*, *118*(11), 6980-6985, doi:10.1002/2013ja019290.

209. Zhang, H., et al. (2007), TC-1 observations of flux pileup and dipolarization-associated expansion in the near-Earth magnetotail during substorms, *Geophys. Res. Lett.*, *34*(3), doi:10.1029/2006gl028326.

210. Zhang, X. J., V. Angelopoulos, A. Runov, X. Z. Zhou, J. Bonnell, J. P. McFadden, D. Larson, and U. Auster (2011), Current carriers near dipolarization fronts in the magnetotail: A THEMIS event study, *J. Geophys. Res.*, *116*, doi:10.1029/2010ja015885.

211. Zhou, X.-Z., V. Angelopoulos, J. Liu, A. Runov, and D.-X. Pan (2014a), Asymmetric braking and dawnward deflection of dipolarization fronts: Effects of ion reflection, *Geophys. Res. Lett.*, n/a-n/a, doi:10.1002/2014GL061794.

212. Zhou, X. Z., V. Angelopoulos, J. Liu, A. Runov, and S. S. Li (2014b), On the origin of pressure and magnetic perturbations ahead of dipolarization fronts, *J. Geophys. Res.*, *119*(1), 211-220, doi:10.1002/2013ja019394.

213. Zhou, X. Z., V. Angelopoulos, J. Liu, A. Runov, and S. S. Li (2014c), On the origin of pressure andmagnetic perturbations ahead of dipolarization fronts, *J. Geophys. Res.*, *119*(1), 211-220, doi:Doi 10.1002/2013ja019394.